Three-Dimensional Finite Element Modelling of Corroded Corrugated Metal Pipe Culverts

by
Alex R. Campbell

Submitted in partial fulfilment of the requirements
for the degree of Master of Applied Science

at

Dalhousie University
Halifax, Nova Scotia
April 2018

DEDICATION PAGE

To my parents, Ross and Elaine, for all their love and support.

TABLE OF CONTENTS

LIST OF TABLES

LIST OF FIGURES

ABSTRACT

The effects of corrosion on the structural response of round CMP culverts is investigated using three-dimensional (3D) finite element models. The validity of the model was assessed by comparing model output with results from full-scale laboratory tests conducted by Mai et al. (2014a). The 3D FE models were then used to carry out parametric studies for intact and corroded culverts. Input parameters for the study of intact culverts were pipe diameter, height of soil cover, soil stiffness, soil strength, and the strength/stiffness of the soil-CMP interface. Total forces in the pipe were found to be most sensitive to pipe diameter and height of soil cover. Input parameters for the study of corroded culverts included corrosion geometry and remaining plate thickness. The largest effects on factor of safety against yielding and buckling occurred when corrosion covered the location of maximum normal stress located at the haunches.

Keywords: culvert, corrosion, infrastructure, corrugated metal pipe, rehabilitation, soil-structure interaction

LIST OF ABBREVIATIONS AND SYMBOLS USED

2D	Two-dimensional
3D	Three-dimensional
A	Pipe wall cross-sectional area per unit length (m^2/m)
a_i	Adhesion intercept of the soil-pipe interface
B	Half of the width of the yielding strip
c'	Cohesion intercept of soil
c'_{ref}	Reference cohesion intercept of soil
CANDE	Culvert ANalysis and DEsign
CHBDC	Canadian Highway Bridge Design Code
CMP	Corrugated metal pipe
CSP	Corrugated steel pipe
D	Pipe centroidal diameter
D	Depth of dry sand stratum above yielding strip
D_i	Inside pipe diameter
D_l	Deflection lag factor
E	Pipe material modulus of elasticity
E_m	Modified modulus of soil stiffness
E_s	Young's modulus of soil; Secant modulus of soil
E_{50}	Secant modulus of soil (triaxial loading)
E_{50}^{ref}	Reference secant modulus of soil
E_{ur}	Unloading-reloading modulus of soil (triaxial loading)
E_{ur}^{ref}	Reference unloading-reloading modulus of soil

E_{oed}	Oedometer loading modulus of soil
E_{oed}^{ref}	Reference oedometer loading modulus of soil
E'	Horizontal modulus of soil reaction
$\bar{E}_{\theta}$	Effective modulus of elasticity in the circumferential direction
$\bar{E}_{L}$	Effective modulus of elasticity in the longitudinal direction
$(EA)_{\theta}$	Pipe wall circumferential normal stiffness
$(EI)_{\theta}$	Pipe wall circumferential flexural rigidity
F	Applied load per unit length
F_m	Reduction factor for modifying buckling stress
F_y	Yield strength of pipe material
f_b	Buckling strength of the pipe wall
FE	Finite Element
FS_y	Factor of safety against yielding
$FS_{y(min)}$	Minimum factor of safety against yielding
FS_b	Factor of safety against buckling
$\bar{G}_{\theta R}$	Circumferential out-of-plane shear modulus of the orthotropic pipe plate
$\bar{G}_{LR}$	Longitudinal out-of-plane shear modulus of the orthotropic pipe plate
$\bar{G}_{\theta L}$	In-plane shear modulus of the orthotropic pipe plate
H	Height of soil cover
H'	Half the vertical distance between the crown and springline
HS	Hardening Soil (soil model in Plaxis 3D)
h_c	Critical height of backfill for compaction effects
I	Pipe wall moment of inertia per unit length

K	The coefficient of lateral earth pressure; Factor representing the relative stiffness of pipe wall with respect to the adjacent soil
K_a	The active coefficient of lateral earth pressure
K_n	Empirical kneading coefficient
K_p	The passive coefficient of lateral earth pressure
K_0	At-rest coefficient of lateral earth pressure
$K_{0(NC)}$	At-rest coefficient of lateral earth pressure (normally consolidated)
$K_{0(OC)}$	At-rest coefficient of lateral earth pressure (overconsolidated)
K_s	Bedding constant
k_n	Normal stiffness of soil-pipe interface
k_s	Shear stiffness of soil-pipe interface
L	Pipe length
L_c	Longitudinal extent of corrosion
LE	Linear-Elastic (soil model in Plaxis 3D)
MC	Mohr-Coulomb (soil model in Plaxis 3D)
OCR	Overconsolidation ratio
PS_H	Pipe hoop stiffness
PS_B	Pipe bending stiffness
P_t	Percentage of intact plate thickness remaining
p	Radial pressure on the pipe
p_{ref}	Reference pressure
R	Centroidal radius of the pipe
R_c	Radius of the pipe at the crown (=R for round pipes)
R_{inter}	Strength reduction factor of soil-pipe interface

r	Radius of gyration of the corrugated pipe plate
r_e	Relative element size factor
SA	Single axle
SW	Single wheel pair
t	Pipe plate thickness
t_i	Interface element thickness
t_0	Intact plate thickness
$\bar{t}$	Effective (orthotropic) pipe plate thickness
W_c	Marston load per unit length of pipe
W_p	Weight of pipe per unit length
z_c	Critical depth for compaction effects
α	Inclination of the wall from vertical
β	Inclination of the ground surface form horizontal
γ	Unit weight of pipe material
γ_s	Total unit weight of soil
γ'_s	Effective unit weight of soil
$\bar{\gamma}$	Unit weight of orthotropic pipe plate
ΔD	Change of the inside diameter
Δx	Horizontal deflection or change in diameter
Δy	Change of inside diameter measured in the direction of the applied load
$\Delta \sigma'_h$	Change in horizontal effective stress
$\Delta \sigma'_v$	Change in vertical effective stress
δ	Wall-soil interface friction angle

ε	Total soil strain
ε^e	Elastic component of soil strain
ε^p	Plastic component of soil strain
θ_c	Circumferential extent of corrosion
θ_0	Angle of radial line from vertical demarking the upper and lower portions of the pipe for evaluation of buckling strength.
λ	Factor used in calculating K
ν	Poisson's ratio of pipe material
ν_s	Poisson's ratio of soil
$\bar{\nu}$	Poisson's ratio of the orthotropic pipe plate
ρ	Reduction factor for buckling strength
σ'	Effective normal stress
σ'_d	Deviator effective stress
σ'_h	Horizontal effective stress
$\sigma'_{h(max)}$	Maximum horizontal effective stress
$\sigma'_{h(0)}$	Horizontal effective stress prior to application of compaction load
$\sigma'_{h(1)}$	Horizontal effective stress during application of compaction load
$\sigma'_{h(2)}$	Horizontal effective stress after removal of compaction load
σ'_v	Vertical effective stress
$\sigma'_{v(1)}$	Vertical effective stress during application of compaction load
$\sigma'_{v(2)}$	Vertical effective stress after removal of compaction load
σ'_1	Major principal stress
σ'_3	Minor principal stress
τ_s	Shear strength of soil

τ_θ	Shear stress in any planar orientation
φ'	Effective friction angle of the soil
φ_i	Friction angle of the soil-pipe interface
ϕ_t	Resistance factor for buckling strength
ψ'	Effective dilation angle of the soil

ACKNOWLEDGEMENTS

I would like to express my sincere gratitude to my supervisor, Dr. Hany El Naggar, for his continuous support, patience, and willingness to have extended discussions around any issues I encountered during my work.

I am also indebted to Dr. Craig Lake and Dr. Andrew Corkum, each of whom made significant contributions to my education and development in the field of geotechnical engineering.

Finally, huge amounts of support and encouragement were provided by my family (especially my wife, Brigitte), friends, and colleagues. I could not have done this without you!

CHAPTER 1:
INTRODUCTION

Many culverts are currently in service all over the world. Their abundance is a direct result of their considerable utility; most notably, culverts enable roads to be constructed across watercourses without blocking the flow of water. Examples of typical highway and railroad embankment culverts are shown in Figure 1.1.

(a) (b)

Figure 1.1 Typical culvert applications: a) highway culvert for stream crossing (Contech, 2017); and b) railroad culvert for small vehicle access (Armtec, 2015)

Unfortunately, many existing culverts have reached or are nearing the end of their serviceable lifespans. Many corrugated metal pipe (CMP) culverts suffer from accelerated rates of deterioration, primarily due to abrasion and corrosion of the metal. It is currently not a straightforward task to determine how the overall stability of a culvert structure is influenced by pipe degradation of this sort. The main difficulty arises from the fact that the structural response of a CMP culvert relies on a complex interaction between the pipe and its surrounding soil. This problem is of practical interest to culvert owners, especially as funding for infrastructure renewal continues to be scarce in many parts of the world. A better understanding of the effects of deterioration on CMP culverts would allow owners to more effectively prioritize—and engineers to more efficiently design—their repairs, rehabilitations, and/or

replacements. The problem of deteriorated CMP culverts is further described in the next section and forms the basis for the research that follows.

1.1 Historical Background

Although culverts have been constructed using a variety of cross-sectional shapes, one of the simplest and most common shapes is the round (i.e. circular) pipe. In this case, the culvert is constructed by first placing the round pipe on a layer of prepared bedding. Next, the pipe is enveloped by an engineered backfill soil, which is placed and compacted in successive layers (typically 150 to 300 mm thick) up to some height above the crown (top) of the pipe.

A major part of the design process for culvert structures is the selection of the pipe material. Corrugated steel pipes (CSP) were developed at the end of the 19th century and were used as culverts as early as 1896 (Corrugated Steel Pipe Institute, 2009). The corrugated geometry provided the pipe with additional stiffness and strength without increasing the thickness of the pipe wall, as would be necessary if using a plain pipe of the same diameter. Due to its lower initial cost and relative ease of installation, corrugated metal soon surpassed concrete as the preferred material for culvert construction. However, the design implications of using this new, relatively flexible pipe remained poorly understood. In 1941, Merlin Spangler developed the famous Iowa formula (Spangler, 1941), which provided a theoretical basis for the design of buried flexible conduits. Spangler's work, in combination with the post-World War II infrastructure boom of the 1950's and 1960's, led to the proliferation of corrugated metal culverts around the world. Although CMP culverts provided many advantages during this time, their legacy now presents a widespread problem due degradation of the pipe metal.

1.2 Problem Description

All structures are susceptible to degradation over time. The main problem associated with CMP culverts is one of durability. The metal pipe plate—typically made of galvanized steel (aluminum is also used)—tends to wear away over time, primarily

caused by two destructive mechanisms: abrasion and corrosion. The effects of deterioration can develop anywhere on the surface of the CMP, but they are most frequently concentrated on the inside (water side) of the pipe, between the invert and the maximum water level. Bed load abrasion acts to remove the protective coating (if present), exposing the underlying metal and making it susceptible to corrosion.

A typical corrosion pattern along the invert of a CMP culvert is shown in Figure 1.2. In this case, the degree of corrosion is so severe that much of the metal has been fully perforated, and significant erosion of the surrounding soil is evident. Erosion of the backfill soil surrounding the CMP is highly undesirable since the soil plays a critical role in the overall stability of the soil-metal structure (further explanation is provided in section 2.2). Once this level of degradation has been reached, repair or rehabilitation of the culvert is usually not feasible, and a full replacement may be necessary. Therefore, it is prudent to address deteriorating CMP culverts well before full perforation of the metal occurs anywhere on the pipe.

Figure 1.2 CMP culvert in Halifax, Nova Scotia exhibiting severe corrosion along the invert (Campbell, 2015)

Deterioration of the metal in CMP culverts is not always confined to the invert of the pipe. For example, accelerated rates of corrosion may occur along plate seams and connections, where stress concentrations and leakage are prone to exist. Sanitary

sewer culverts often suffer from corrosion on the inside and unsubmerged portions of the pipe (i.e. at the crown and shoulders) due to direct attack by corrosive gases, such as hydrogen sulphide (H_2S) and sulphur dioxide (SO_2). Deterioration of the metal can also occur anywhere on the outside (soil side) of the pipe, especially where the surrounding soil or groundwater conditions are particularly aggressive. Figure 1.3 shows a CMP culvert in Dartmouth, NS, Canada with inner (water-side) corrosion along the invert and lower haunches, and outer (soil-side) corrosion at the crown, shoulders, and springlines.

Figure 1.3 CMP culvert in Dartmouth, Nova Scotia exhibiting corrosion at the crown and haunches. (Campbell, 2017)

Figure 1.4 shows the results of a condition survey carried out in 2007 inclusive of 1,931 CSP culverts in Sweden (Mattsson & Sundquist, 2007) plotted by age of the culvert. Nearly half of all existing (and recently demolished) CSP culverts (925/1,931 = 48%) were between 33 to 47 years old, and about half of those (445/925 = 48%) needed replacement or repair. A significant portion of culverts between 18 to 32 years old (180/481 = 37%) were also in need of repair or replacement. Design

lifespans for major highway culverts reportedly range from 30 to 75 years (Tenbusch et al., 2009; United States Army Corps of Engineers, 1998). However, the lifespan of a galvanized corrugated metal pipe can be less than 20 years because of invert corrosion damage (Tenbusch et al., 2009).

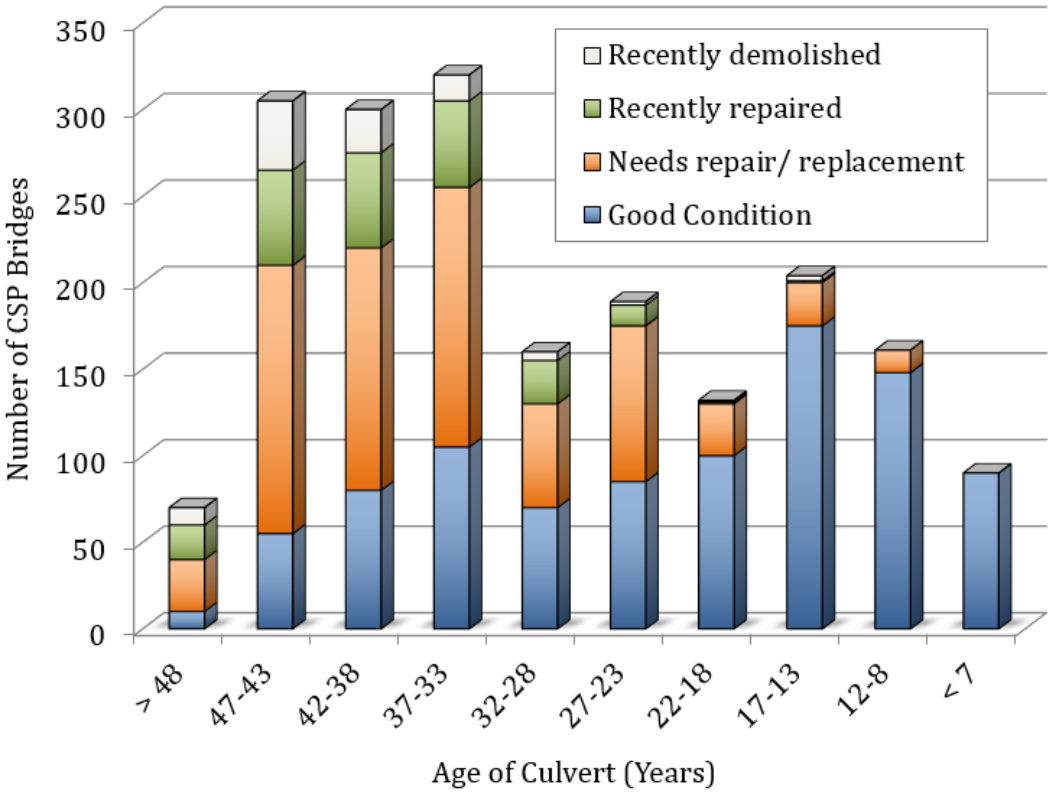

Figure 1.4 Condition of 1,936 CSP culverts in Sweden (Mattsson & Sundquist, 2007).

The economic cost of culvert failures far exceeds that of replacement alone, as detailed by Perrin and Chintan (2004). Furthermore, failing culverts represent a serious risk to public safety. Increasing focus over the past couple of decades has thus been shifted towards the maintenance of existing systems and away from new construction projects. Many methods of repairing and rehabilitating deteriorated CMP culverts exist, from the conventional installation of a cast-in-place reinforced concrete invert (shown in Figure 1.5) to various contemporary methods of relining the existing structure.

At this point, most government agencies have realized the importance of good asset management; inspection programs are generally well established, and culvert

conditions are often assessed in qualitative terms. Reliable techniques to quantitatively evaluate the stability of deteriorated CMP culverts, however, are still evolving. In the absence of unlimited fiscal resources, such evaluations are necessary to efficiently prioritize and design the restoration of these culvert structures.

Figure 1.5 CMP culvert rehabilitated by the in-place installation of a concrete invert.

The overall mechanical behaviour of a buried flexible pipe is dependent on a complex interaction between the structure (pipe) and the surrounding soil, making it difficult to predict using analytical methods. However, numerical techniques such as the finite element method—in which a large system is analyzed by discretizing the overall geometry into a (finite) number of smaller, simpler components (elements)—has proved very useful in this regard. Two-dimensional, elastic finite element analyses have recently been performed (El-Taher & Moore, 2008; Mai, 2013) to evaluate the stability of corroded corrugated metal culverts. Two-dimensional models, however, rely on simplifying assumptions to approximate certain three-dimensional (3D) aspects of the real problem, such as live load spreading through the cover soil and 3D corrosion geometries. Moreover, the use of linear elastic constitutive soil models may be insufficient for modelling the observed non-linear force-displacement response of real flexible culverts subjected to incremental earth and live loading. Linear elastic

soil models neglect the shear strength and stress-dependent stiffness of real soils. The purpose of this thesis is to investigate the effects of corrosion on the stability of CMP culverts, through the development and application of a 3D, non-linear finite element model.

1.3 Research Objectives

The specific objectives of this research are as follows:

- Develop a 3D finite element (FE) model capable of predicting: a) the structural forces that develop in intact, round CMP culverts during backfilling and live loading; and b) the incremental structural forces that develop in a CMP culvert that has subsequently corroded and is subjected to live loading. The 3D FE model should account for the construction sequencing, compaction effects, behaviour of the soil-pipe interface, and the non-linear behaviour of the surrounding soil.
- Compare the results from the 3D FE model to published results from full-scale laboratory testing.
- Compare the results from the 3D FE model to previously published results from a 2D linear elastic model.
- Compare the results from the 3D FE model using three (3) different constitutive soil models (Linear Elastic (LE), Mohr-Coulomb (MC), and Hardening Soil(HS));
- Use the 3D FE Model to investigate the effects of various input parameters on the structural response of intact CMP culverts; and
- Use the 3D FE Model to investigate the effects of various corrosion parameters on the stability of corroded CMP culverts.

1.4 Contents

Chapter 2 is a review of some of the pertinent research conducted over the last 70 years with respect to the behaviour and analysis of round CMP culverts subjected to

earth and live loading. The literature review is divided into two main sub-sections: experimental studies and numerical studies. Chapter 3 describes the development of a comprehensive, 3D non-linear finite element model that can simulate the structural response of both intact and deteriorated round CMP culverts. The model is calibrated by comparing its output to experimental results on a relatively small culvert from Chapter 2. In Chapter 4, the same methodology described in Chapter 3 is applied to carry out a parametric study for intact CMP culverts. A parametric study for corroded CMP culverts is then carried out in Chapter 5. Findings from the research are summarized in Chapter 6, along with a discussion of limitations and suggestions for future work.

CHAPTER 2:
LITERATURE REVIEW

2.1 Introduction

This chapter consists of a brief review of the most pertinent insights that have been gained to date on the topic of performance and analysis of buried CMP culverts.

2.2 Soil-Structure Interaction

Strictly speaking, any physical system in which a structure is in direct contact with the ground involves some degree of soil-structure interaction. In certain situations, however, the relationship between the response of the soil and the motion of the structure—and vice versa—is more integrated than in others. Buried flexible CMPs subjected to earth and live loading, for example, interact with the surrounding soil to such a degree that they behave as composite (soil-metal) structures.

2.2.1 Buried Flexible Pipe Behaviour

The "flexibility" of a pipe generally refers to its circumferential (ring) bending stiffness. A pipe with a low circumferential bending stiffness is described as "flexible", while a "rigid" pipe has a high circumferential bending stiffness. The response of unburied flexible pipe subjected to diametrically-opposed vertical loads differs significantly from that of rigid pipe, as illustrated in Figure 2.1. Rigid pipe experiences negligible deflections, carrying the load through internal bending moments. Flexible pipe contracts vertically and expands in the horizontal direction, forming a horizontal ellipse (a response described as "ovaling"). When flexible pipes are buried, the side-fill (soil placed beside the pipe between the invert and crown) provides lateral restraint, allowing the pipe to maintain its shape without the development of bending moments. Vertical loads are converted to circumferential axial force in the pipe (a.k.a. hoop thrust). Since CMPs typically have high hoop stiffness, the presence of sidefill significantly increases their load-carrying capacity. Denser (stiffer) sidefills provide more support than loose sidefills. Local bending will still occur at the pipe crown,

where downward deflection of the pipe is unrestrained. Although the bending stiffness of pipe should be sufficient to prevent excessive deflection, a small amount of downward movement is desirable, as it induces a phenomenon known as soil arching, which significantly reduces the load on the pipe (this will be discussed further in section 2.2.2).

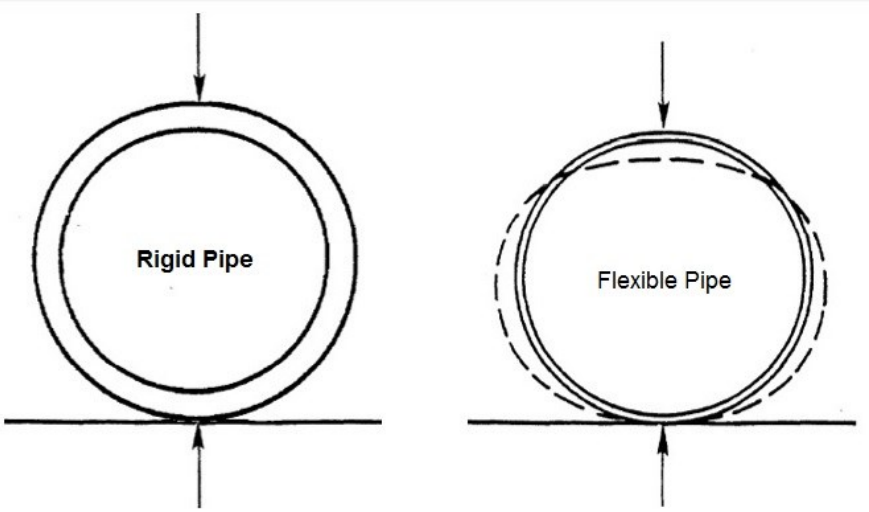

Figure 2.1 Deflection of rigid versus flexible pipe under vertical load (from FHA (1995)).

The early history of buried flexible pipe analysis is described by Watkins and Anderson (1999). In the early 20th century, Iowa State College Dean of Engineering Anston Marston was conducting research on buried rigid pipes with the goal of developing design procedures for highway pipes and culverts. He assigned his student, M.G. Spangler, the task of burying samples of rigid pipe and measuring the soil loads on them so that they could be related to the failure loads obtained from parallel-plate load tests. During this time, the prevalence of corrugated steel pipes (CSPs) was on the rise. Spangler realized that for these flexible pipes, the parallel plate load tests were not representative of buried conditions. This led to his development of the Iowa formula (Spangler, 1941) for predicting the increase in horizontal diameter produced by earth load placed above the crown of the pipe. Decades later, with the help of his student R.K. Watkins, he published a refined version of the equation which became known as the modified Iowa formula (Watkins & Spangler, 1958):

$$\Delta x = \frac{D_l K_s W_c r^3}{(EI + 0.061 E' r^3)} \qquad 2.1$$

Spangler assumed that the value of *E'*, defined as the "horizontal modulus of soil reaction", was constant for a given soil type and density. Experimental tests later confirmed suspicions, however, that *E'* is a function of soil depth (confinement) and ring stiffness, in addition to soil type and density. Obtaining a reliable estimate of this soil-structure interaction parameter was very difficult, and the formula was gradually abandoned in favour of methods based on ring compression theory. Closed form elastic solutions for buried flexible pipe, such as the one developed by Burns & Richard (1964), provided a theoretical basis for standard design procedures. The Burns & Richard solution uses the conventional soil properties E_s and ν_s, and provides not only horizontal pipe deflection, but also vertical pipe deflection, wall thrust, bending moment, and radial pressure at any point along the pipe circumference.

The advancement of numerical methods—particularly the finite element (FE) method—over the last several decades has allowed greater customization of the problem geometry and material properties. In 1976, an open source, two-dimensional finite element computer program, CANDE (Katona, 1976), was developed specifically for the design and analysis of all types of culverts. The Soil-Culvert Interaction (SCI) method (Duncan, 1978) uses formulas and design graphs based on results from numerous two-dimensional finite element analyses. Modern computing power has greatly enhanced the use of FE models in research and in practice. Currently, many sophisticated 3D FE software packages are commercially available. Contemporary design codes in North America ((CSA, 2014); (AASHTO, 2014)) are based on Limit States design philosophies.

2.2.2 Soil Arching

Some of the earliest insights with respect to the mechanism of arching in granular soils were provided by Karl Terzaghi (1883-1963), through his experimental investigation (Terzaghi, 1936) and subsequent theoretical work (Terzaghi, 1943). He considered a stratum of dry sand of depth D and unit weight γ supported by a rigid

base containing a yielding strip, or "trap-door" (line *ab* in Figure 2.2a) of width equal to *2B*. The initial vertical stress along the entire base is equal to *γD*. It had been known for over a century that the slightest downward movement of a trap-door in this scenario reduces the vertical stress on the trap-door to a fraction of its initial value. However, Terzaghi provided one of the first explanations of the mechanism behind this phenomenon.

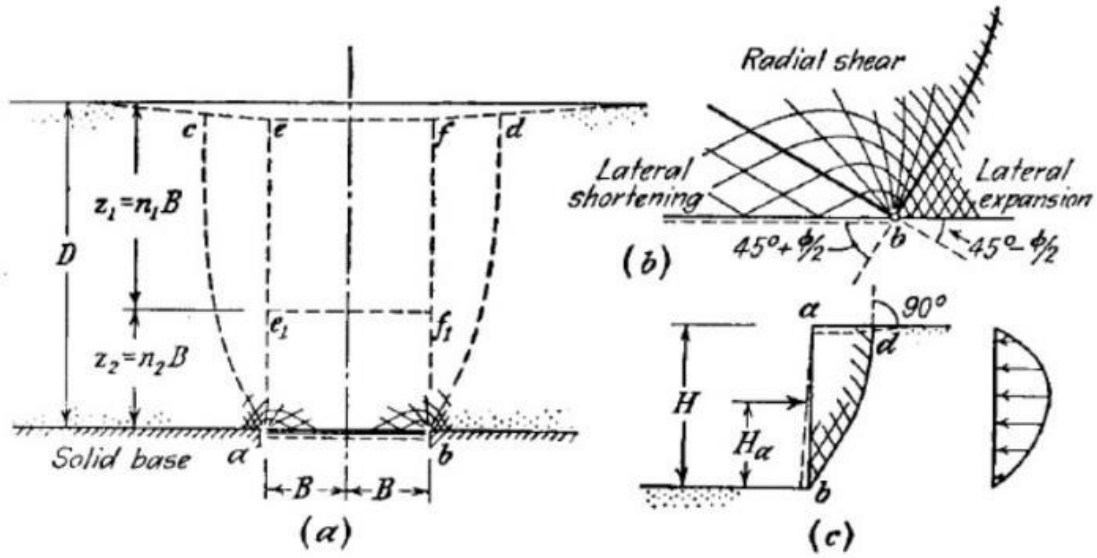

Figure 2.2 Development of arching in sand above a yielding trap-door (Terzaghi, 1943).

In response to a small downward movement of the trap-door, the sand immediately above the trap-door (volume abe_1f_1) expands vertically and contracts horizontally, inducing the sand adjacent to this volume to extend laterally and contract vertically. This generates radial shear zones as the inner soil seeks to move past the outer soil towards the trap-door. A portion of the weight of the sand between these shear zones (equal to the sum of the vertical components of the frictional forces generated) is transferred to the outer, stationary soil. As the trap-door continues to yield, the inclination of shear zones shifts from 45 + (φ'/2) to 90° (vertical) due to the progressive disintegration of the soil structure above the trap-door, and the vertical pressure on the trap-door increases slightly until it reaches an ultimate value.

Terzaghi's experimental tests (1936) comprised a 7.3 cm-wide by 46.3 cm-long trapdoor in the base of a bin containing approximately 31 cm of sand. The tests were

conducted using loose (φ' was not provided) and dense (φ' = 44°) sand. As the trapdoor deflected downward, the deflection and total load upon the trapdoor were measured. Horizontal and vertical stresses were determined at various heights above the trapdoor based on the friction resistance of tapes placed in the soil (i.e. the "friction tape method"). Results of the tests revealed the following:

- The reduction in vertical pressure due to a slight downward movement of the trap-door is greater for dense sand than for loose sand.
- As yielding of the trapdoor continues, the vertical stress on the trapdoor increases until an ultimate (maximum) value is reached, which is equal in the case of dense and loose sand.
- For both dense and loose sand, the coefficient of lateral earth pressure *K* above the yielding strip increases from about unity immediately above the centreline of the strip to a maximum of about 1.5 at approximately *2B* above the centreline. At greater heights than about *5B* (2.5 times the width of the trap-door) above the centreline, the yielding strip seems to have no effect on the state of stress in the sand.

Results from full-scale experimental tests have shown that the crown of a flexible buried pipe is analogous to a yielding trap-door. A soil arch forms as the load is applied and the crown of the pipe deflects downward (Figure 2.3).

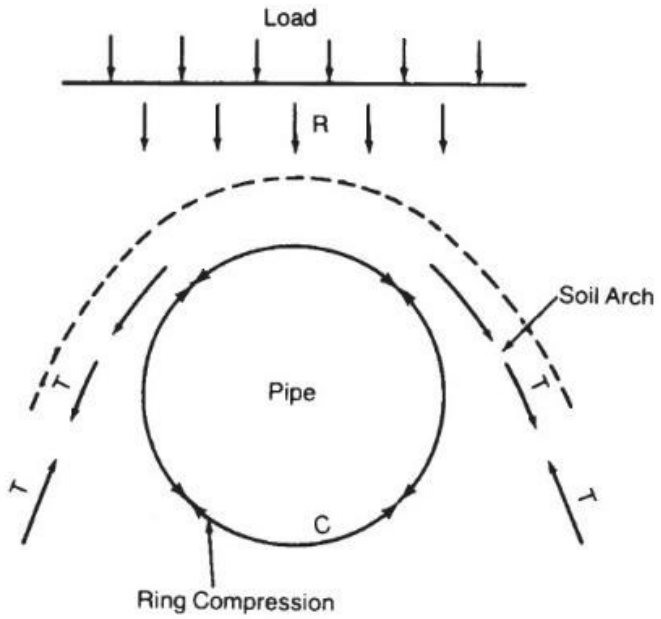

Figure 2.3 Soil arching over flexible pipe (Corrugated Steel Pipe Institute, 2009).

2.2.3 Soil-CMP Interface

Another aspect of soil-structure interaction that impacts the overall behaviour of CMP culverts is the relative displacement between the soil and the CMP at their contact surface (the soil-CMP interface). The behaviour of a soil-structure interface is anisotropic; the responses to changes in stress are very different in the normal (perpendicular to the contact surface) and shear (parallel to the contact surface) directions. Typical results obtained from direct shear tests are shown in Figure 2.4. The normal behaviour is often modelled as linear elastic with a normal stiffness k_n, and the shear behaviour as elastic-perfectly plastic with a shear stiffness k_s. The stiffness parameters k_n and k_s do not represent real physical soil properties; they are used to describe the rate of change of stress with displacement ($kN/m^2/m$).

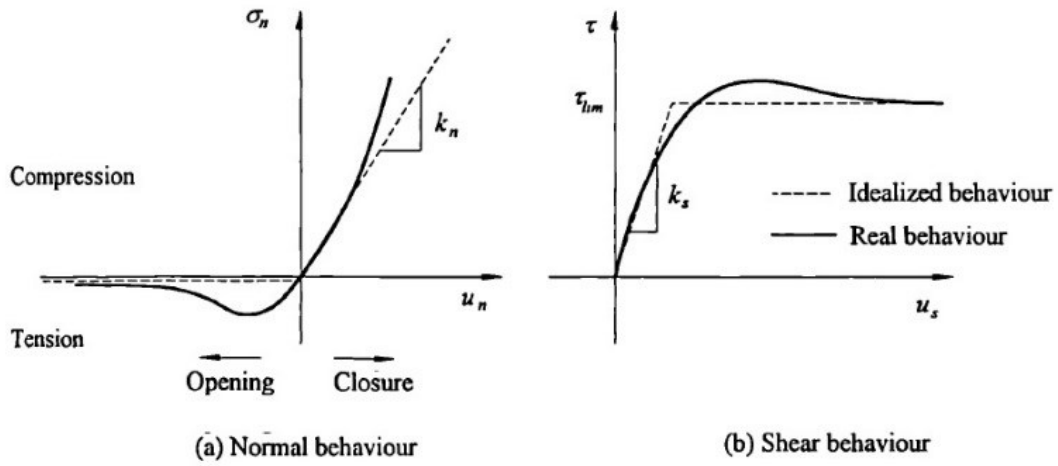

Figure 2.4 Typical stress-displacement relationships at the soil-structure interface measured from direct shear tests (Desai & Nagaraj, 1988).

Closed-form solutions for buried pipes based on the theory of elasticity ((Burns & Richard, 1964) allow two different slippage conditions at the interface to be considered: perfectly rough (i.e. rigid, fully bonded, or no slip), or perfectly smooth (i.e. un-bonded, or full slip). Actual slippage conditions, however, lie somewhere in between these two idealizations. Also, tensile normal stresses could lead to separation between the soil and the structure (gapping). Finite element methods can account for these behaviours using special interface elements, to which unique material models can be assigned. If the friction angle, adhesion, and normal stress at the soil-pipe interface are denoted as φ_{ii}, and a_i, respectively, and σ_i is the normal stress at the interface, the Mohr-Coulomb failure criterion can be used to establish the limiting shear strength of the interface, τ_i:

$$\tau_i = a_i + \sigma_i \tan \delta_i \qquad 2.2$$

The material parameters typically required as input by commercial finite element programs are the Young's Modulus E_i and Poisson's ratio ν_i. For a given interface element thickness t_i, the values of E_i and ν_i can be computed from the normal modulus $K_n = k_n t_i$ and shear modulus $K_s = k_s t_i$, using Equations 2.3 and 2.4 (Ng, 1994):

$$E = \frac{(3K_n - 4K_s)K_s}{K_n - K_s} \quad 2.3$$

$$\nu = \frac{K_n - 2K_s}{2(K_n - K_s)} \quad 2.4$$

Alternatively, many FE programs allow the shear strength and elastic modulus of the interface elements to be specified as a percentage of the material properties of the adjacent soil. This is typically accomplished by assigning a reduction factor ranging from 1 (in which the interface properties assume 100% of the adjacent soil properties) to 0.001 (0.1% of the adjacent soil properties). Due to the difficulty of selecting an accurate value for the analysis of CMP culverts, the interface is often modelled as fully bonded (i.e. infinite strength) or assigned a strength reduction value in the range of about 0.5-0.6 (Allen, Duncan & Snacio, 1988).

2.3 Compaction Effects

2.3.1 Classical Earth Pressure Theories

The ratio of the horizontal to vertical effective stress at a position within a soil mass is defined as the coefficient of lateral earth pressure, *K*, and is given in Equation 2.5. If no lateral strains exist in the ground (i.e. lateral earth stresses are the same as they were in the undisturbed state), this coefficient is called the coefficient of lateral earth pressure at rest, K_0. At-rest conditions may exist, for example, in naturally deposited, undisturbed soils, or in uncompacted backfill soils adjacent to a rigid, unyielding structure. Jaky (1948) developed an empirical relationship for determining K_0 for normally consolidated, cohesionless soils (Equation 2.6) in terms of the effective internal friction angle of the soil, φ'. This relationship was later modified by Mayne and Kulhawy (1982) to accommodate overconsolidated soils (Equation 2.7).

The changes in the stress conditions in a soil as it transitions between the at-rest, active and passive conditions are perhaps best illustrated using Mohr's circles, as shown in Figure 2.5. For a soil element below a horizontal ground surface, the horizontal effective stress σ'_h under at-rest conditions is the confining stress (i.e.

minor principal stress) σ'_3, and the vertical effective stress σ'_v is the major principal stress σ'_1. If the confining stress, $\sigma'_3 = \sigma'_h$, is decreased (e.g. when a structure deflects away from the adjacent soil), the shear strength of the soil, τ_s will be reduced. The vertical stress $\sigma'_1 = \sigma'_v$ will remain unchanged. Consequently, the deviator stress, $\sigma'_d = \sigma'_1 - \sigma'_3$, will increase along with the shear stress in any planar orientation, τ_θ, manifesting in an expanding Mohr's circle. Therefore, a minimum value of σ'_h (and thus, K) is quickly reached as shear failure of the soil is initiated. This is known as the active condition, and the associated value of K is the active coefficient of lateral earth pressure, K_a. The magnitude of K_a is typically in the range of 0.2 to 0.5. Conversely, if (starting from the at-rest condition) the horizontal effective stress is increased (such as when a structure deflects into the adjacent soil), the deviator stress will reduce until $\sigma'_h = \sigma'_v$. If σ'_h is increased further, the vertical effective stress suddenly becomes the confining stress, and the horizontal effective stress becomes the major principal stress (i.e. $\sigma'_3 = \sigma'_v$ and $\sigma'_1 = \sigma'_h$). The differential stress is increased, causing Mohr's circle to expand until it reaches the failure envelope, at which point the soil fails in shear. This is known as the passive condition. The value of K is at a maximum in the passive condition and is known as the passive coefficient of lateral earth pressure, K_p. Values of K_p are typically between 2 and 6.

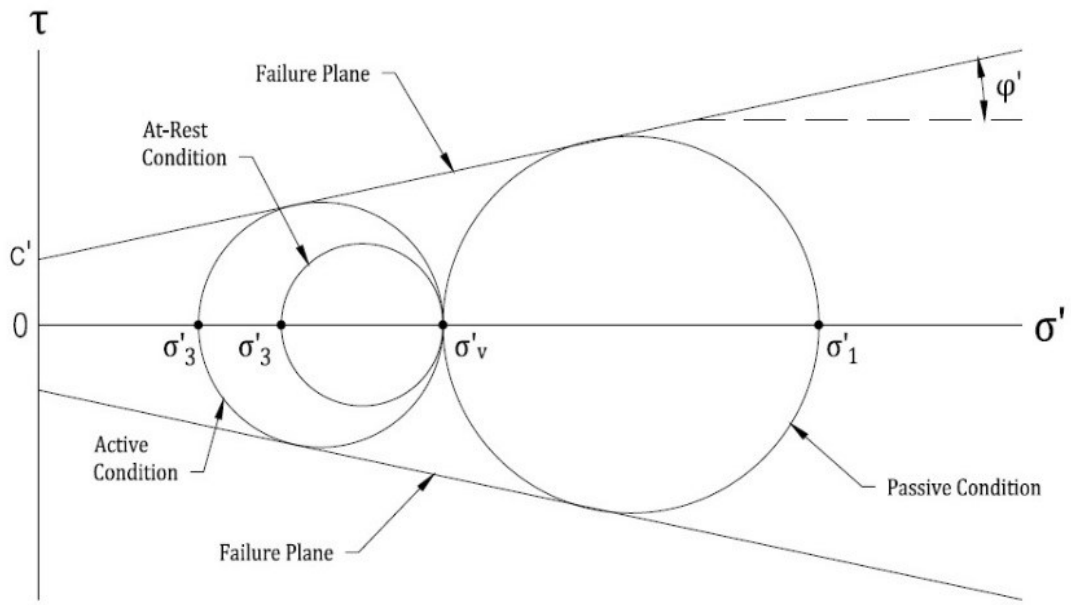

Figure 2.5 Mohr's diagram for at-rest, active, and passive conditions (adapted from (Coduto, 1999)).

Although many contemporary theories exist for predicting lateral earth pressures, all of them are born from the classical work of Charles Coulomb (1736-1806) and William Rankine (1820-1872). Coulomb (1776) used limit equilibrium theory to determine the limiting horizontal pressures acting on a retaining wall at failure in compression and extension, assuming a planar failure surface. His work was later generalized ((Mayniel, 1808);(Müller-Breslau, 1906)) to include the wall-soil interface friction angle, δ; the inclination of the ground surface from horizontal, β; and the inclination of the wall from vertical, α. The resulting formulas are given in Equations 2.8 and 2.9. The latter is seldom used in practice, however, due to the belief that it may overestimate the value of K_p. Consequently, K_p is typically estimated according to the earth pressure theory of Rankine (1857). Rankine developed a stress field solution that assumes a frictionless wall, and a vertical wall-soil interface. Simplified versions of his equations for active and passive coefficients of lateral earth pressure (assuming $\beta = 0$) are provided in Equations 2.10 and 2.11, respectively. Bell (1915) showed analytically that for soils with cohesion ($c \neq 0$), the limits of lateral

earth pressure are extended by $2c\sqrt{K}$, resulting in what are known as the Rankine-Bell earth pressure equations (Equations 2.12 and 2.13).

$$K = \frac{\sigma'_h}{\sigma'_v} \tag{2.5}$$

$$K_{0(NC)} = 1 - \sin\phi' \tag{2.6}$$

$$K_{0(OC)} = K_{0(NC)} OCR^{(sin\phi')} \tag{2.7}$$

$$K_a = \frac{\cos^2(\phi' - \alpha)}{\cos^2\alpha\cos(\delta + \alpha)\left(1 + \sqrt{\frac{\sin(\delta + \phi')\sin(\phi' - \beta)}{\cos(\delta + \alpha)\cos(\beta - \alpha)}}\right)^2} \tag{2.8}$$

$$K_p = \frac{\cos^2(\phi' - \alpha)}{\cos^2\alpha\cos(\delta - \alpha)\left(1 - \sqrt{\frac{\sin(\delta + \phi')\sin(\phi + \beta)}{\cos(\delta - \alpha)\cos(\beta - \alpha)}}\right)^2} \tag{2.9}$$

$$K_a = \tan^2\left(45 - \frac{\phi'}{2}\right) = \frac{1 - \sin\phi'}{1 + \sin\phi'} \tag{2.10}$$

$$K_p = \tan^2\left(45 + \frac{\phi'}{2}\right) = \frac{1 + \sin\phi'}{1 - \sin\phi'} \tag{2.11}$$

$$\sigma'_h = K_a\sigma'_v - 2c\sqrt{K_a} \tag{2.12}$$

$$\sigma'_h = K_p\sigma'_v + 2c\sqrt{K_p} \tag{2.13}$$

In addition to soil densification, compaction causes lateral strains in the soil that are largely irrecoverable, and result in increased lateral earth pressures. Effectively, the soil becomes overconsolidated as the vertical compaction load is removed. For flexible CMP culverts, these compaction-induced lateral earth pressures can be significant, as they magnify the peaking response that occurs during sidefilling.

2.3.2 Ingold, 1979

In addition to increasing the magnitude of lateral earth pressures, the compaction of successive backfill layers around a flexible pipe also has an influence on the resulting distribution of lateral earth pressures. Ingold (1979) described a simple analytical method for predicting the magnitudes and distribution of compaction-induced lateral earth pressures behind retaining walls.

The logic behind Ingold's predicted lateral stress distribution is depicted in Figure 2.6. If z is the depth below grade, then for a layer of soil with an effective unit weight γ' that is placed behind a smooth retaining wall, the vertical effective stress prior to application of the compaction load, $\sigma'_{v(0)}$, is computed according to Equation 2.14:

$$\sigma'_{v(0)} = \gamma' z. \qquad 2.14$$

Assuming there is sufficient lateral yield of the wall to reach the active condition,

$$\sigma'_{h(0)} = K_a \sigma'_{v(0)} = K_a \gamma' z. \qquad 2.15$$

When the compaction load is applied, the vertical soil stress at any given point below the ground surface increases by $\Delta\sigma_v'$. The increase in horizontal soil stress, $\Delta\sigma_h'$, is directly proportional to $\Delta\sigma_v'$, i.e.:

$$\Delta\sigma'_h = K_a \Delta\sigma'_v. \qquad 2.16$$

The distribution of this compaction-induced lateral earth pressure below the ground surface is represented by the solid blue line in Figure 2.6. The vertical and horizontal soil stresses during application of the compaction load, $\Delta\sigma'_{v(1)}$ and $\Delta\sigma'_{h(1)}$, respectively, are given by Equations 2.17 and 2.18:

$$\sigma'_{v(1)} = \sigma'_{v(0)} + \Delta\sigma'_v = \gamma' z + \Delta\sigma'_v \qquad 2.17$$

$$\sigma'_{h(1)} = \sigma'_{h(0)} + \Delta\sigma'_h = K_a \gamma' z + K_a \Delta\sigma'_v = K_a(\gamma' z + \Delta\sigma'_v) \qquad 2.18$$

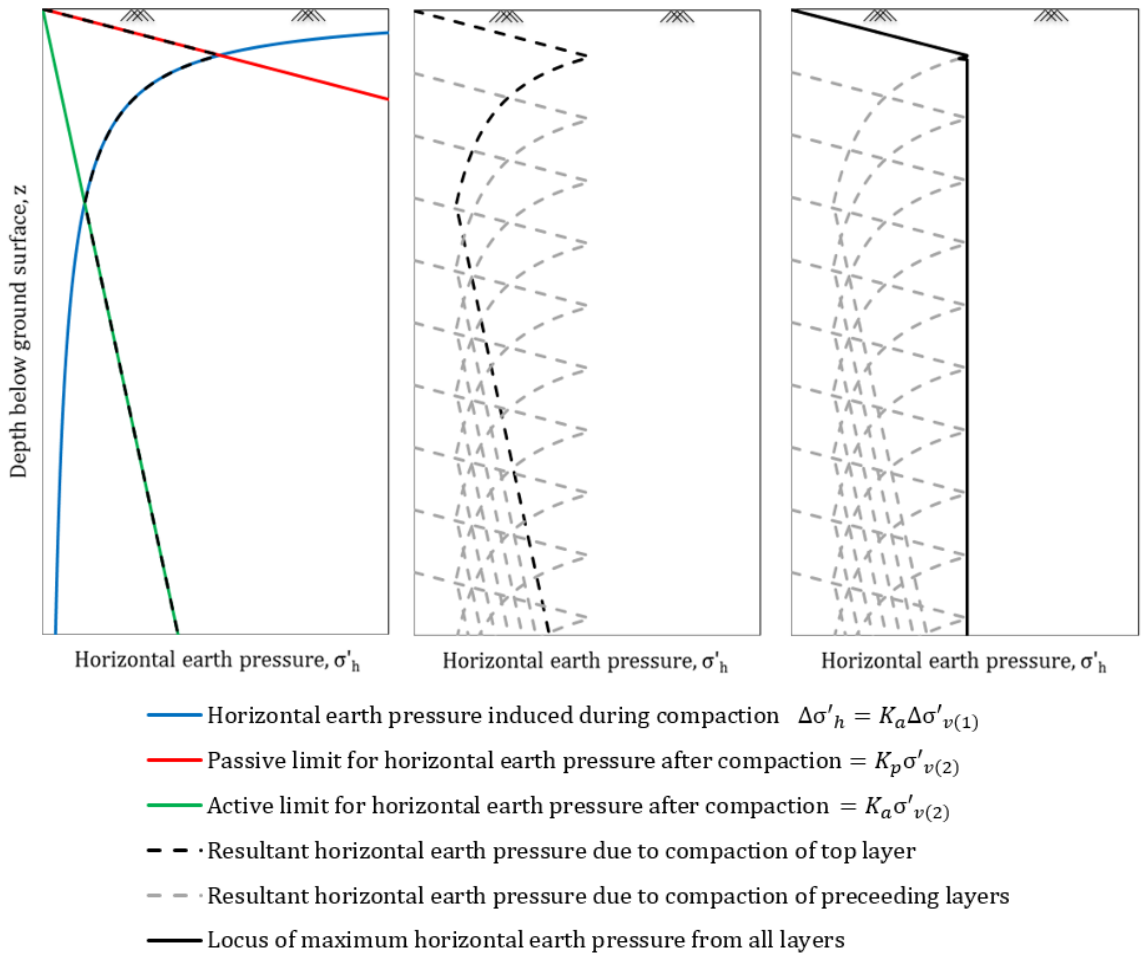

Figure 2.6 Development of horizontal earth pressure distribution below the ground surface after compaction of multiple successive backfill layers behind a retaining wall (after Ingold, 1979).

Once the compaction load is removed, the soil becomes unrestrained at the ground surface and can expand vertically. The vertical stress essentially returns to its initial value, i.e. $\sigma'_v = \sigma'_{v(2)} \approx \sigma'_{v(0)}$ (full recovery is limited due to friction at the soil-structure interface). Conversely, the soil remains confined in the horizontal plane, and the compaction-induced lateral earth pressures are largely retained, i.e. $\sigma'_h = \sigma'_{h(2)} \approx \sigma'_{h(1)}$. Exceptions occur near the ground surface, where low confining (vertical) stresses lead to passive failure of the soil, and at greater depth, where active conditions prevail due to high confining stresses. A critical depth, z_c, therefore exists, above which the

residual horizontal stresses are governed by the passive limit, i.e. $\sigma'_{h(2)} = K_p\sigma'_{v(2)} = K_p\sigma'_{v(0)}$ (depicted by the solid red line in Figure 2.6). If it is assumed that the value of $\gamma' z_c$ is negligible compared to that of $\Delta\sigma'_v$, then z_c can be approximated using Equation 2.19. A critical height of backfill, h_c, also exists, below which the residual horizontal stresses are governed by the active limit, i.e. $\sigma'_{h(2)} = K_a\sigma'_{v(2)} = K_a\sigma'_{v(0)}$ (depicted by the solid green line in Figure 2.6).

$$z_c = \frac{{K_a}^2 \Delta\sigma'_v}{\gamma'} \qquad 2.19$$

The dashed black line in Figure 2.6 represents the residual lateral earth pressure distribution resulting from the placement and compaction of a single layer of backfill soil. The maximum horizontal stress, $\sigma'_{h(max)}$, occurs at the critical depth and can be estimated using Equation 2.20.

$$\sigma'_{h(\max)} = K_p\gamma' z_c \qquad 2.20$$

As successive backfill layers are placed and compacted, the value of $\sigma'_{h(max)}$ follows a straight-line locus (the solid black line in Figure 2.6), providing an estimate of the horizontal stress distribution below the surface of the final compacted backfill soil. Importantly, the shape of this distribution is uniform, as opposed to the linear distribution that would be assumed if compaction effects were not considered. Ingold showed that predictions of wall deflections made using his simple analytical approach agreed favourably with results taken from three case histories.

2.3.3 Elshimi, 2013

Elshimi & Moore (2013) made one of the more recent attempts to incorporate the effects of soil compaction in the finite element modelling of buried pipes. Since explicit modelling of the compaction process including soil densification introduces an enormous amount of complexity (especially in the context of a much larger model), it is preferable to use a simpler method that produces similar results. Previous research has explored means of imposing the anticipated compaction-induced lateral

earth pressures either directly to the culvert (McGrath, 1999) or to the sidefill soil (Taleb & Moore, 1999) after each individual layer is placed. The technique of Taleb and Moore worked well, except that imposing passive lateral earth pressures did not provide an upper limit for the peaking deformations observed in the test structure they were modelling.

When the soil is compacted beside a flexible pipe, the pipe will deflect horizontally, thus relieving a portion of the lateral earth pressure that would normally be sustained in the case of rigid pipe. However, in almost all cases, multiple "passes" of compaction equipment are applied to achieve the desired state of soil compaction. Once plastic lateral strains have already developed in the soil, therefore, additional lateral stresses are introduced, which in turn causes further deflection of the pipe. Elshimi and Moore appropriately described this phenomenon as soil kneading.

Elshimi considered the effect of soil kneading by multiplying the initial lateral pressure (which was set equal to the passive pressure $K_p\sigma'_v$) by an empirical kneading coefficient, K_n. It is shown that this kneading coefficient can be applied without violating the shear failure criterion of the soil, provided a non-zero value of soil cohesion is used that satisfies Equation 2.21, i.e.:

$$c > (K_n - 1)\frac{\sqrt{K_p}}{2}\sigma'_v \qquad 2.21$$

A small value of soil cohesion (4 kPa) was used, which allowed a maximum value for K_n of 2, and was sufficient to produce the desired response for the cases considered in this study. Since the initial lateral pressure is determined using the Rankine-Bell equation for passive earth pressure, the effects of pipe wall-soil friction and inclination of the pipe wall are neglected.

Calculated deformations from a 2D FE model were compared to the measured values for five circular pipes employing different materials (2 CMP, 2 concrete, and 1 high-density polyethylene (HDPE)), diameters, relative flexural stiffnesses, compaction methods, etc. as reported by McGrath et al. (1999). A couple of salient conclusions were drawn:

- The deformations for those pipes which were compacted using a rammer were effectively estimated when a kneading factor of 2 was used.
- It appears that there is no need to model soil compaction (let alone incorporate a kneading factor) for pipes compacted using a small vibratory compactor.

2.4 CMP Degradation

Since the structural integrity of CMP culverts depends on the combined behaviour of the pipe and the surrounding soil, deterioration of either one of these constituents can lead to instability. However, most problems affecting the service lives of CMP culverts are related to the durability of the pipe. CMPs are susceptible to degradation from the combined forces of abrasion and corrosion.

Corrosion is a natural, electrochemical process in which a refined metal seeks to return to a more stable form (Roberge, 2008). The mechanism for corrosion of steel (the metal from which most CMP culverts are made) is illustrated in Figure 2.7, in which the anode and cathode are locations on the surface of the metal. The anode and cathode are connected through the metal by an electronic path, and through the solution (air, water, or soil) by an ionic path. Electrochemical corrosion involves the transfer of electrons from the anode to the cathode, inducing a direct current flow through the corrosion cell.

Steel is an alloy of iron and other elements, primarily carbon. Through a chemical reaction called oxidation, electrons are removed from the iron atoms in the steel and flow towards the cathode, where they are used up in the reduction of oxygen. The reduction reaction requires the simultaneous presence of water and oxygen, the source of which may be dissolved oxygen in the water, moisture in the air, or water and air trapped in the soil. The net effect is that the steel gets converted into hydrated ferric oxide (rust), which has virtually no strength and will quickly wear away, resulting in a loss of metal at the surface of the anode.

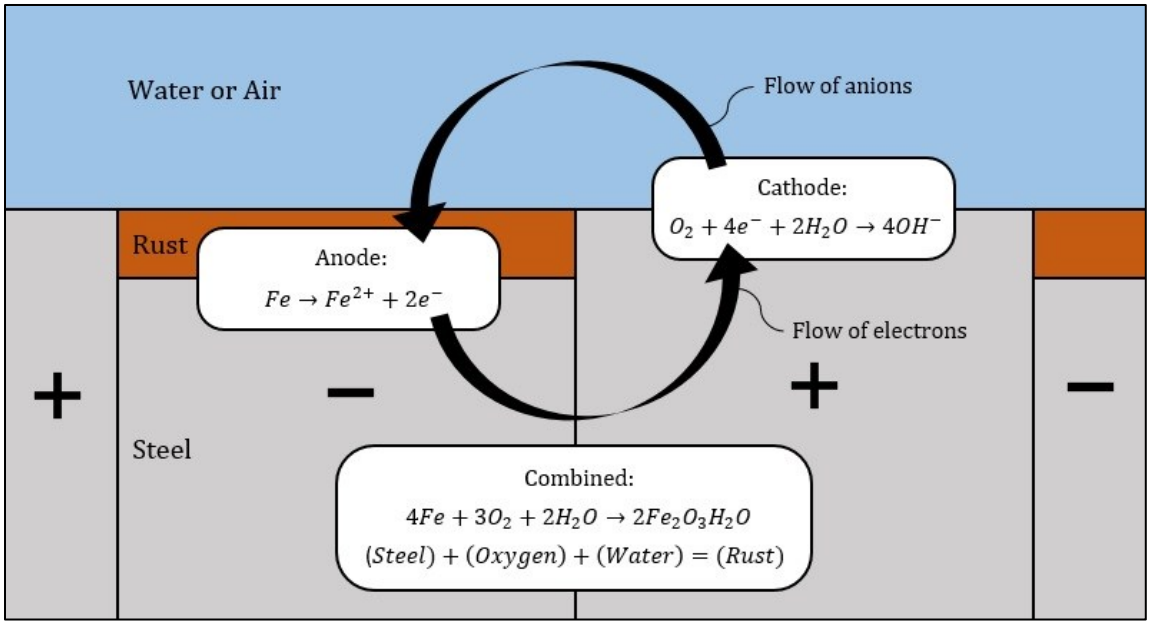

Figure 2.7 Mechanism of electrochemical corrosion of steel (adapted from (Roberge, 2008)).

Some of the primary factors affecting the rate at which corrosion develops include:

- Reactivity of the metal: Metal alloys like steel are highly susceptible to corrosion, while naturally occurring metals such as gold and silver are virtually immune to it, even on geological timescales.
- Acidity: Acidic (low pH) environments accelerate corrosion by supplying hydrogen ions for the reduction of oxygen.
- Resistivity: Dissolved ions, such as those resulting from road de-icing salts, decrease resistivity and quicken corrosion.
- Temperature: Higher temperatures cause faster corrosion as they are associated with increased levels of kinetic energy and, thus, rates of chemical reactions.
- Microbiology: The presence of microorganisms on the surface of the metal can greatly expedite the corrosion process, but is generally only a problem in soil or relatively stagnant water.

The corroded zones in CMP culverts tend to be concentrated along the invert and on the inside of the pipe, as shown in Figure 2.8. This is because the invert is typically in direct contact with water for longer periods of time than any other part of the pipe. Although many CMP culverts include a protective coating such as zinc (galvanization) as part of the design, abrasion from streambed sediment transport can remove this coating over time and expose the underlying metal. Degradation of CMP is not limited to the invert, however. The full circumference of sanitary sewer pipes, for example, are vulnerable to direct attack by corrosive gases released from the wastewater, such as H_2S and SO_2 (EPA, 1991).

Figure 2.8 Invert corrosion of a CMP culvert (Hansen, 2007).

2.5 Experimental Studies

A limited amount of experimental data is available concerning the response of round CMP culverts subjected to earth and live loading. Primary sources include the live load field testing of two large-diameter, round CMP culverts performed by Bakht (1980), a series of trial tests on small-diameter CMP culverts during backfilling by Webb (1995), and the laboratory tests of Mai (2013) on both intact and deteriorated, small-diameter CMP culverts during backfilling and live loading.

2.5.1 Bakht, 1980

Perhaps the most often-cited experimental tests on CMP culverts are those carried out by Bakht (1980). Three in-service culverts located in Ontario, Canada were tested to determine the circumferential thrusts and bending moments generated in the CMP due to live loading. Unfortunately, no testing was carried out during construction, so the pipe response due to earth loading (backfilling) is unknown. Details pertaining to the backfill soil are unavailable, except that it was "composed of well compacted high-quality granular material." Nevertheless, these tests provided valuable empirical data on the behaviour of round CMP culverts subjected to live loading.

The first structure tested was the Deux Rivières culvert (Figure 2.9a), which is comprised of a round, 7.77 m-diameter, 31.1 m-long CMP with a maximum cover height of 2.60 m. The pipe plate corrugation profile was 5.45 mm-thick, with a wavelength (pitch) of 152 mm and an amplitude (depth) of 51 mm. The second structure tested—the Adelaide Creek culvert—will not be discussed here since it has a horizontally elliptical cross-section, and the scope of this thesis is limited to circular culverts. The third and final structure tested was the White Ash Creek culvert (Figure 2.9b), a 7.62 m-diameter round CMP with a length of 23.8 m and a maximum cover height of 1.25 m. The corrugated plate is 4.67 mm-thick with a pitch and depth of 152 mm and 51 mm, respectively.

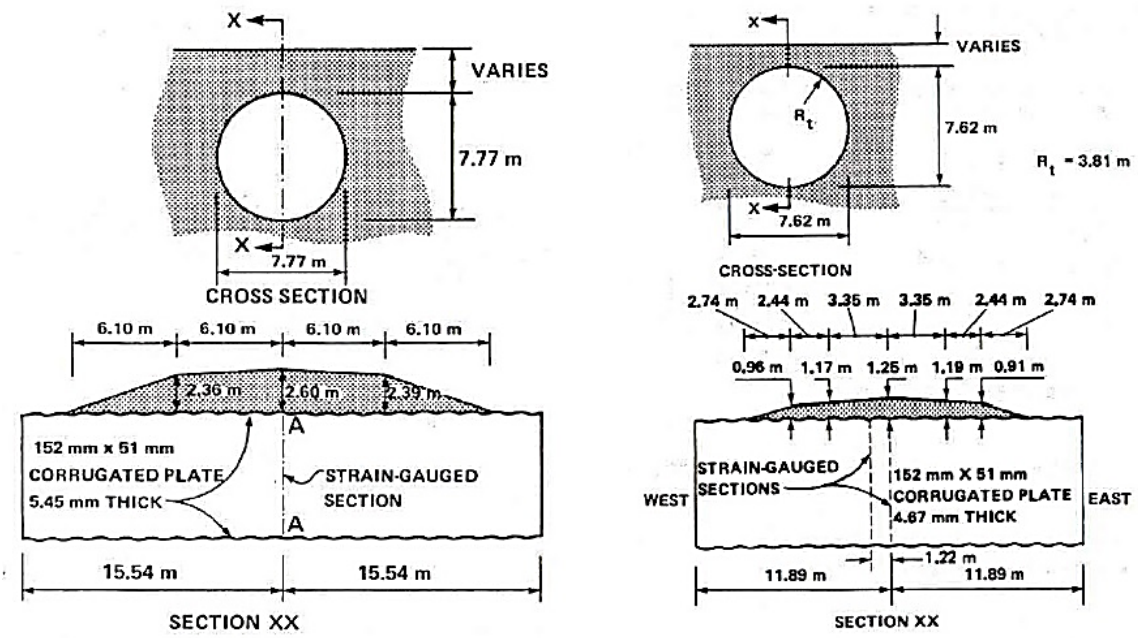

(a) (b)

Figure 2.9 Details of the two culverts tested by Bakht: (a) Deux Rivières and (b)White Ash Creek culverts tested by Bakht (1980).

Figure 2.10 White Ash Creek culvert during live load testing (Bakht, 1980)

Each of the CMP's was instrumented with displacement transducers and uniaxial strain gauges on the inside of the pipes at various locations around the circumference, allowing direct measurements of pipe deflections and indirect measurements of pipe thrusts and moments. The live load was applied using a testing vehicle (shown in Figure 2.10) whose axle weights could be adjusted through the addition or removal

of concrete blocks. Since most of the weight was concentrated on the rear two axles, the live load can be approximated as acting over an effective rectangular area with dimensions measuring 2.44 m wide (along the longitudinal axis of the pipe) by 1.83 long (perpendicular to the longitudinal axis of the pipe). Measurements were taken with the centre of the effective loaded area located at various positions with respect to the centreline of the pipe, as illustrated in Figure 2.11.

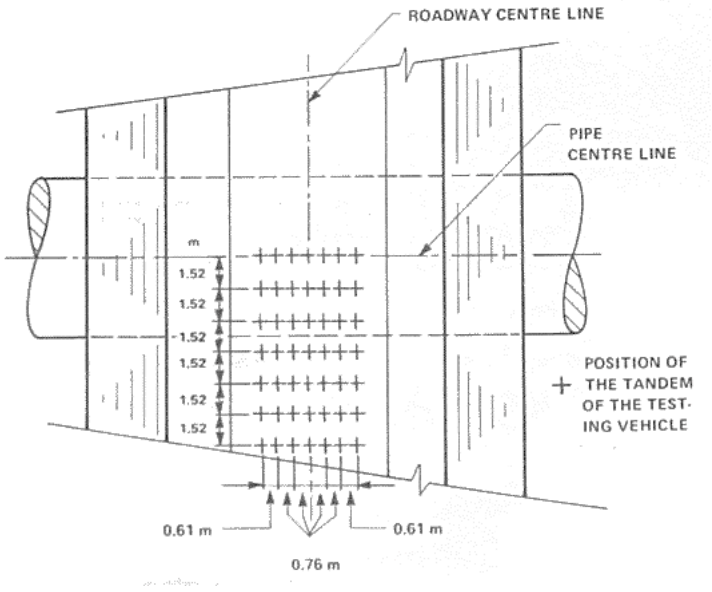

Figure 2.11 Positions of effective rear tandem loads used in field tests by Bakht (1980)

Bakht found that the incremental circumferential thrust distribution in the pipe due to live loading was non-uniform (Figure 2.12(a) and Figure 2.13(a)). This observation was contrary to the widely-held assumption at the time (i.e. that circumferential live load thrusts in flexible culverts are uniformly distributed), which in turn assumed that friction at the pipe-soil interface is negligible. When the rear tandem axles were centred over the longitudinal axis of the pipe (Figure 2.12(a) and Figure 2.13(a)), live load thrusts were maximum at the shoulders and slightly reduced at the crown. As the position of the live load moved in the direction transverse to the longitudinal axis of the pipe, the maximum thrust occurred in the portion of the pipe closest to the live load, and dissipated rapidly away from it (Figure 2.12(b) and Figure 2.13(b)). In some instances, this resulted in tension developing on the opposite side of the pipe.

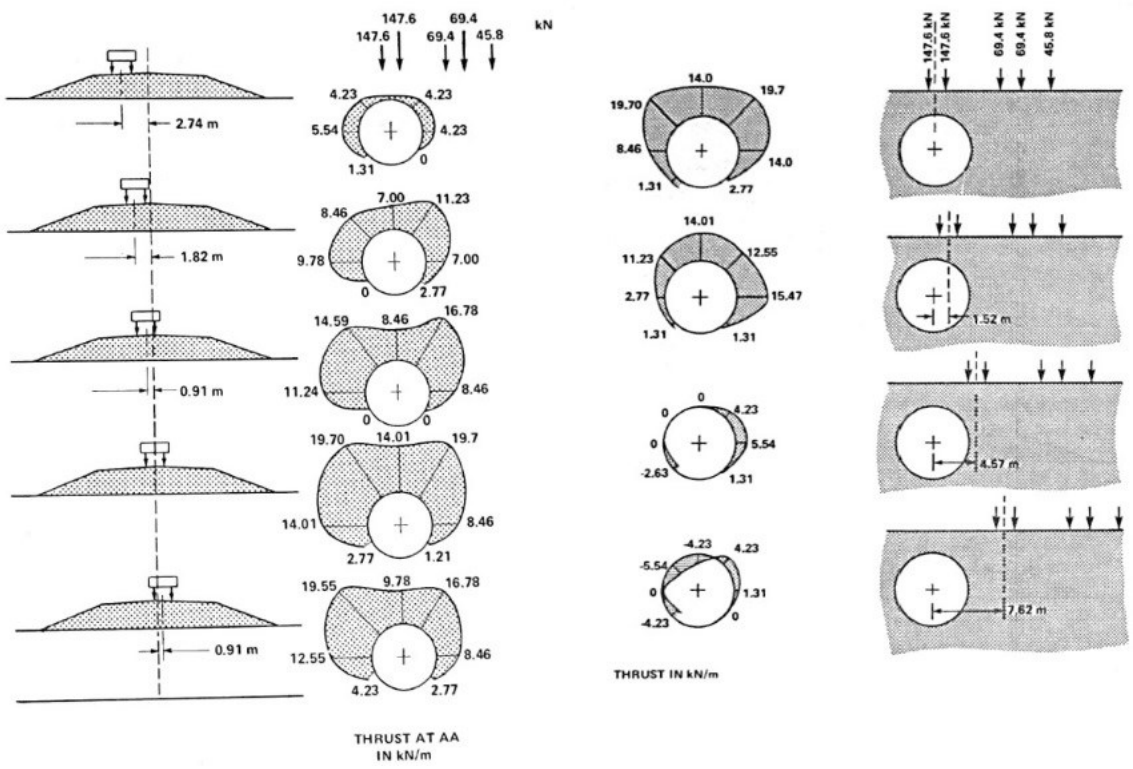

(a) (b)

Figure 2.12 Live load thrust distributions in Deux Rivières culvert with variation of the position of the testing vehicle: in the (a) transverse direction, and (b) longitudinal direction (Bakht, 1980)

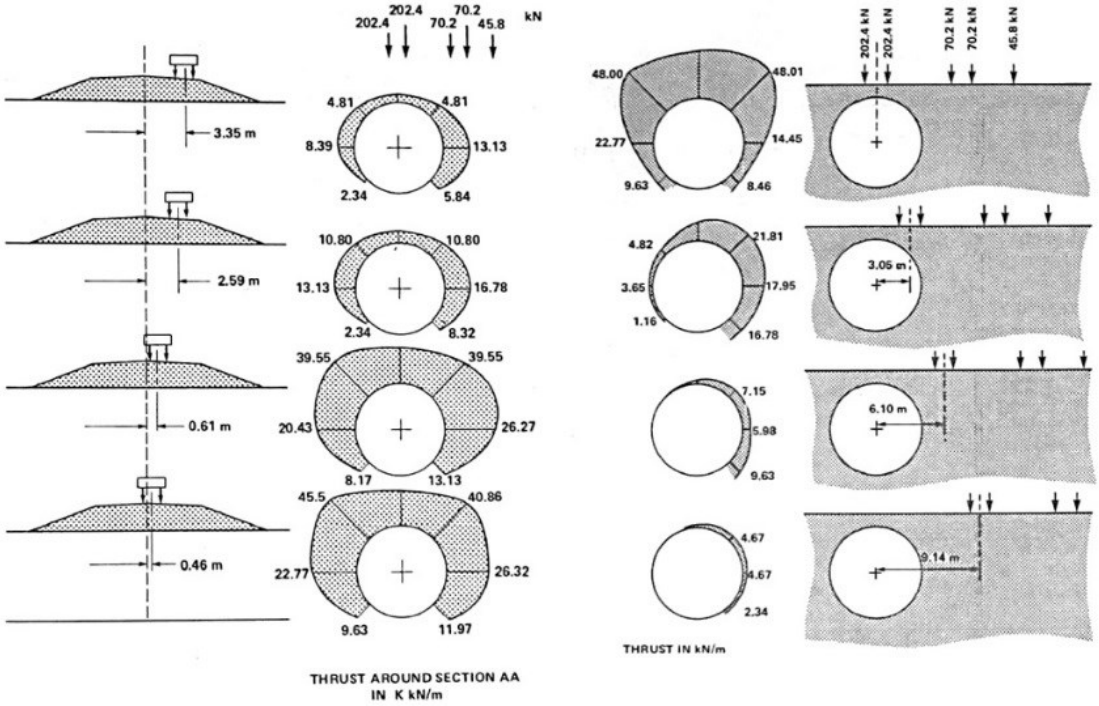

(a) (b)

Figure 2.13 Live load thrust distributions in White Ash Creek culvert with variation of the position of the testing vehicle: in the (a) transverse direction, and b) longitudinal direction (Bakht, 1980)

Another interesting finding was that the distance of the live load from a given section of the pipe had a different influence in the transverse (Figure 2.14(a)) and longitudinal (Figure 2.14(b)) directions. As the position of the live load moved away from a given section of the pipe in the longitudinal direction, live load thrusts dispersed about twice as rapidly as they did in the transverse direction. Live load bending moments were found to be negligible in both the Deux Rivières and White Ash Creek culverts, because these CMPs are flexible relative to their surrounding soils.

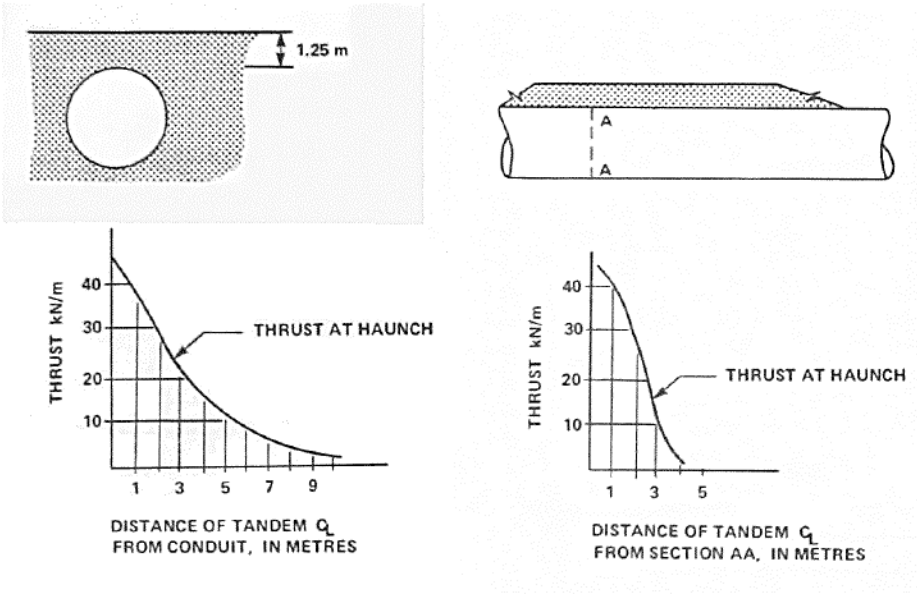
1.25 m
THRUST kN/m
40
30
20
10
THRUST AT HAUNCH
1
3
5
7
9
DISTANCE OF TANDEM C_L
FROM CONDUIT, IN METRES
A
A
THRUST kN/m
40
30
20
10
THRUST AT HAUNCH
1
3
5
DISTANCE OF TANDEM C_L
FROM SECTION AA, IN METRES

(a) (b)

Figure 2.14 Live load thrust at haunch with variation of distance of the testing vehicle in the (a) transverse direction, and (b) longitudinal direction (Bakht, 1980)

2.5.2 Webb, 1995

Fifteen years after Bakht's experimental tests, Mark Webb (1995) conducted a series of field studies of buried pipe behaviour during backfilling. Several full-scale field installations were conducted at the University of Massachusetts, Amherst, using different materials and geometries. Pipe materials included reinforced concrete, corrugated and profile wall high-density polyethylene (HDPE), and corrugated metal. This review will focus on those tests conducted using corrugated metal pipes.

A total of 14 tests were performed. For each test, all three types of pipe (concrete, plastic, and metal) were installed end to end in the same excavated trench. The metal pipes tested were 3.1 m-long, round CMPs with inside diameters (IDs) measuring 0.914 m and 1.524 m. Sections of pipe measuring 1.2 m in length were placed at the free ends to minimize the effects of the ends of the pipes on the test sections. Test pipes were placed inside the trench on a layer of bedding soil, then heavily instrumented prior to being covered with approximately 1.2 m of fill material. For the tests on the CMPs, backfill was placed in equal lifts approximately 305 mm thick. Imported backfill was used up to a height of 150 mm above the top of the pipe, and in-situ material was used to fill the remainder of the trench. Two more lifts of sidefill (backfill placed between the invert and crown elevation) were placed for the larger pipe than for the smaller pipe. The following parameters were measured after placing each successive lift of backfill material: pipe wall strains, pipe profiles, elevations, in-situ density and moisture, soil strains, horizontal soil stress at the interface of backfill and native soil, vertical soil stress, pipe-soil interface pressures, and soil penetration resistance. The primary field test variables consisted of trench width, in-situ soil type, backfill material type, degree of backfill compaction, haunching (compaction of soil under the haunches, which cannot be accessed with the same compaction equipment used elsewhere) techniques, bedding material type, and degree of bedding compaction.

The properties of the pipes tested were characterized by their hoop stiffness and bending stiffness. The hoop stiffness is the ratio of load (p) to the diametric strain ($\Delta D/D$) under external hydrostatic pressure and is defined by Equation 2.1. The bending stiffness is the ratio of the force per unit length of pipe to the change in inside diameter in a parallel plate test (ASTM D2412) and is defined by Equation 2.2.

$$PS_H = \frac{p}{\Delta D/D} = \frac{p}{\frac{pr}{EA}} = \frac{EA}{r} \qquad 2.22$$

$$PS_B = \frac{F}{\Delta y} = \frac{EI}{0.149r^3} \qquad 2.23$$

The CMPs used in these tests are considered to have high hoop stiffness, and are flexible in bending (as opposed to rigid). Properties of the CMPs used in the field tests are summarized in Table 2.1.

Table 2.1 CMP properties for field tests by Webb (1995).

Parameter	Symbol	Units	Value	
Internal Diameter	D_i	m	0.914	1.524
Corrugation profile (pitch x depth)	-	mm	68 x 13	76 x 25
Pipe plate thickness	t	mm	1.63	1.63
Weight of pipe	W_p	kN/m	0.37	0.88
Modulus of elasticity of steel	E	GPa	205	205
Pipe plate cross-sectional area	A	mm^2/mm	1.64	1.88
Pipe plate moment of inertia	I	mm^4/mm	31.0	142.0
Pipe hoop stiffness	PS_H	kN/m/m	730,000	500,000
Pipe bending stiffness	PS_B	kN/m/m	429	420

Some key observations based on the test results for the CMPs are as follows:

- In all cases, placement (and compaction, if applicable) of the sidefill soil caused the diameter of the pipe to contract horizontally (negative horizontal deflection) and expand vertically (positive vertical deflection). This response is commonly referred to as “peaking”.

- In all cases, placement of backfill soil above the crown of the pipe caused negative vertical deflection and positive horizontal deflection.
- The method of compaction of the sidefill soil had a significant influence on the shape and magnitudes of pipe deflection. In general, it seems that the use of equipment delivering a greater amount of compaction energy (i.e. rammer vs. vibratory plate, or vibratory plate vs. no compaction equipment) results in greater peaking during sidefilling, and less deflection during backfilling above the crown.
- For rammer-compacted tests, greater peaking during sidefilling (and less deflection during backfilling above the crown) was observed for tests that used silty sand backfill than for tests that used stone backfill. This could be explained in-part by silty sand's comparatively lower friction angle, and therefore higher coefficient of lateral earth pressure (K).
- Greater peaking—in terms of both percent and absolute deflection—was observed for the larger-diameter (1.524 m) pipe than for the small-diameter (0.914 m) pipe.
- Horizontal earth pressures in the backfill soil near the trench wall at the level of the springline showed little increase until backfill material was placed over the top of the pipes, after which they increased relatively linearly.
- Vertical earth pressures in the backfill soil at a level 150 mm above the top of the pipe showed a reduction of approximately 10% in the soil over the crown compared to the soil over the sidefill. This may be evidence of positive arching.

2.5.3 Mai, 2014

More recently, Mai et al. (2014a) conducted experimental tests on two steel culverts with different degrees of corrosion that were exhumed from the field. The first culvert, denoted CSP1, exhibited significant corrosion on either side of the invert. The second culvert, denoted CSP2, was essentially intact with only minor corrosion on

either side of the invert. Both culverts were buried in an 8-m long, 8-m wide test pit in a laboratory at Queen's University, and tested under earth loading and live loading.

Both round CSPs in this study measured 1.8 m in diameter and 3.0 m in length. The corrugation profiles were identical, having a pitch of 67.7 mm, a depth of 12.7 mm, and an intact plate thickness of 4.5 mm. For CSP1, the average remaining wall thicknesses along the east and west side of the invert were 48% and 70%, respectively. For CSP2, average remaining wall thicknesses were 90% along the east side of the invert and 83% along the west side. The intact CSP properties are summarized in Table 2.2.

Table 2.2 CSP properties for experimental tests by Mai et al. (2014a).

Parameter	Symbol	Value CSP1/CSP2	Units
Diameter	D	1.8	m
Length (with extension culverts)	L	6.0	m
Corrugation profile	-	68 x 13	mm
Intact plate thickness	t	4.5	mm
Modulus of elasticity of steel	E	200	GPa
Pipe plate cross-sectional area	A	4.87	mm^2/mm
Pipe plate moment of inertia	I	95.5	mm^4/mm

The backfill material used for both test CSPs was a well-graded sandy gravel (SW-GW). Soil compaction was achieved using a vibrating plate tamper to a compacted state of 95% Standard Proctor Density (SPD). For CSP1, the bedding (soil immediately underlying the pipe) consisted of a 0.84 m-thick layer of compacted material. For CSP-2, the bedding consisted of 100 mm of loose (uncompacted) material underlain by a 0.6 m-thick layer of compacted material. The sidefill was placed using 150 mm-thick, uncompacted lifts for CSP1 and 300 mm-thick, compacted lifts for CSP2. Above the crown elevation, both CSPs were backfilled and compacted using 300 mm-thick lifts to a final cover height of 0.9 m. Live load testing was carried out under 0.9 m cover,

before removing 0.3 m of soil and the repeating the live load testing under 0.6 m cover. Finally, CSP1 was tested to failure.

Live loads were applied through both a single steel pad simulating the load from a single wheel pair (SW) and two pads simulating the load from a single axle (SA). The SW load was applied to the soil surface directly above the centerline (transversely and longitudinally) of the pipe. The SA load was applied at the soil surface through two (2) wheel pairs directly over the centreline of the pipe longitudinally, and 0.9 m on either side of the centreline in the transverse direction, resulting in a 1.8 m centre-to-centre spacing between wheel pairs. The dimensions of each steel pad measured 250 mm (transversely) by 600 mm (longitudinally). Applied forces were based on the CSA CL-625 and the AASHTO design trucks, including dynamic allowances and multiple presence factors to produce a full service-load. A longitudinal cross-section of the test setup is shown in Figure 2.15. The calculated design loads for various load cases are given in Table 2.3.

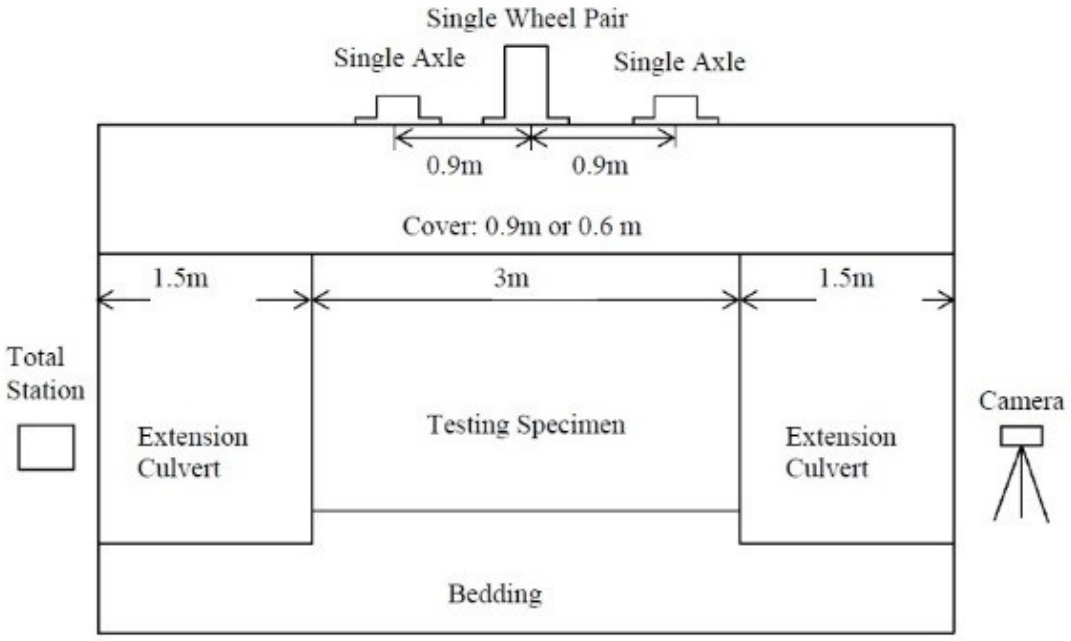

Figure 2.15 Longitudinal section for experimental tests by Mai et al. (2014a)

Table 2.3 Design loads for experimental tests by Mai et al. (2014a).

Cover Height	Load Type	Design Load (kN)	
		CSA	AASHTO
0.6 m	SW	112	91
0.6 m	SA	224	182
0.9 m	SW	106	87.5
0.9 m	SA	214	175

Each CSP was instrumented with string potentiometers to measure the change in diameter, reflective prisms to monitor the deflected shape (via total station), and uniaxial strain gauges to permit post-test calculations of pipe forces, namely thrusts and bending moments.

Selected results for the tests with 0.9 m cover are displayed graphically in Figure 2.16 and Figure 2.17. Some of the key results from the tests are as follows:

- During sidefilling, the vertical expansion (peaking) was similar for CSP-1 and CSP-2, while the horizontal contraction of CSP-1 was 53% higher than that of CSP-2. This difference in pipe response to sidefilling was attributed to the different stiffnesses of the two pipes and the two sidefill soils.
- As the backfill height exceeded the crown elevation, CSP-1 contracted in the vertical direction and expanded in the horizontal direction. In contrast, CSP-2 experienced negligible deflection during backfill above the crown. This response was attributed to the different stiffnesses of the sidefill soils and the deterioration in CSP-1.
- During live loading, the relationship between thrust and applied force was approximately linear for both CSPs under 0.9 m cover, but non-linear under 0.6 m cover. The thrust in CSP-2 was higher than the thrust in CSP-1 at the same applied force with the same cover height (i.e., 71.6% higher under a 100-

kN, SW load with 0.9 m cover). Calculated thrust forces in the corroded areas of CSP-1 were very small.

- Both CSPs exhibited a non-linear relationship between bending moment and applied force for all live load tests.
- Both thrust and bending moment due to live loading were increased when the cover height was reduced from 0.9 m to 0.6 m, confirming the benefits of deeper cover.
- During the failure test, CSP-1 contracted vertically by 87.5 mm at the peak force, which represented a diameter change of 4.8% after backfilling. The strips of steel between the perforations in the corroded area of the haunches began to buckle close to the ultimate load, while plastic hinges developed across the crown at the same time. Despite being heavily deteriorated, CSP-1 did not fail until reaching a SW load of 170 kN (a SA load of 340 kN), which is 90% of the fully-factored SA load for both the CSA and AASHTO design trucks. This suggests that culverts with less deterioration than CSP-1 may have adequate remaining structural capacity.

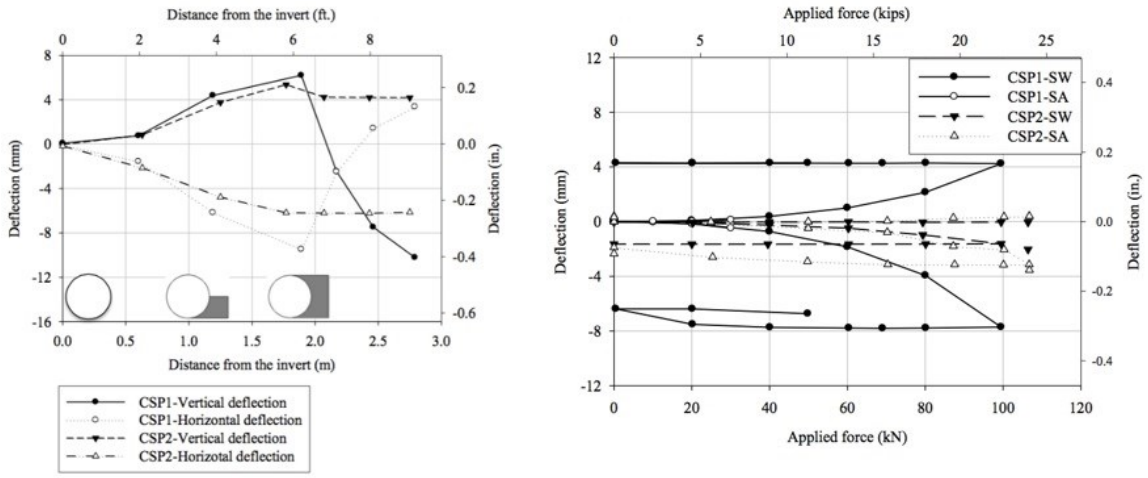

Figure 2.16 Vertical and horizontal deflections during backfilling and live loading with 0.9 m cover (Mai, 2013)

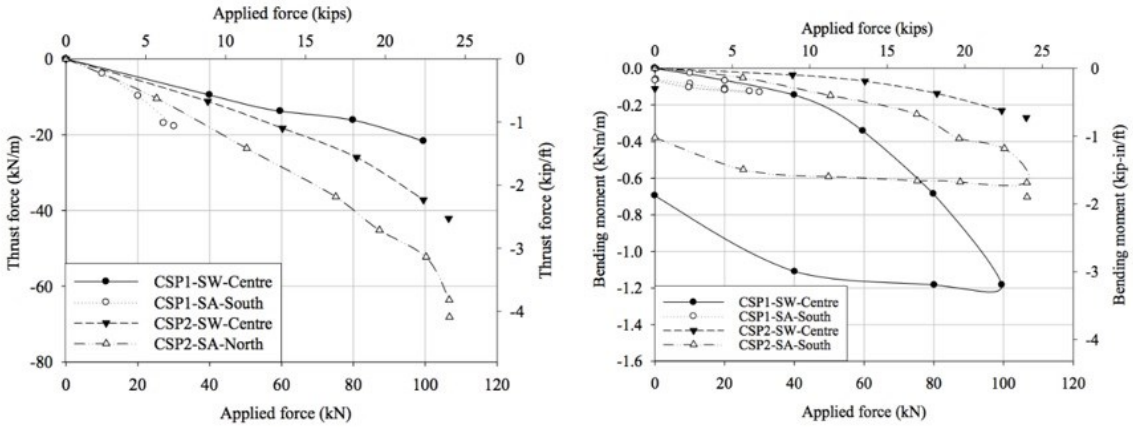

Figure 2.17 Maximum thrusts and bending moments during live loading with 0.9 m cover (Mai, 2013)

2.6 Numerical Studies

The complex response of flexible culverts subjected to earth and live loading makes them difficult to analyze using analytical methods. The finite element method, on the other hand, is well-suited to account for this complex soil-structure interaction. Two-dimensional (2D) finite element analyses of flexible culverts began with Katona (1976) and the development of CANDE. Further contributions were made by Duncan (1979) and Seed & Raines (1988). These 2D methods relied on approximating the three-dimensional dissipation of live loads through the cover soil by converting the actual surface load to an "equivalent" 2D line load. Comparison of these methods with the results of full-scale field tests (Bakht, 1980) revealed that such approximations lead to significant overestimations of calculated circumferential thrust.

2.6.1 Moore and Brachman, 1994

Moore and Brachman (1994) were the first researchers to investigate the use of a three-dimensional (3D) finite element (FE) model for analysis of flexible circular culverts subjected to live loading. Their semi-analytic approach reduced the size of the three-dimensional problem considerably by using a two-dimensional finite element mesh in the transverse direction and harmonic modelling (a Fourier Integral) along the longitudinal direction. Two assumptions are implicit in this

approach: (1) the pipe and embankment ends do not appreciably affect the overall response of the pipe (use of prismatic geometry is required), and (2) all material behaves elastically. The 3D FE procedure was calibrated by successfully predicting the stresses for a 3D problem with a known solution. It was then used, along with conventional 2D FE models, to estimate the response of one of the structures (the Deux Rivières culvert) previously field tested by Bakht (1980).

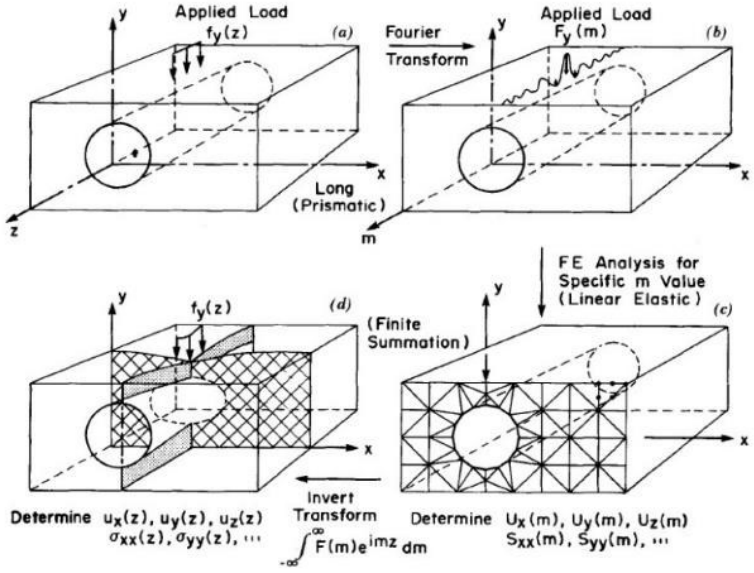

Figure 2.18 Semi-analytic FE model by Moore & Brachman (1994).

The CMP was modelled as plain pipe using solid rectangular elements. Properties of the CMP elements were assigned based on two different structural theories: isotropic and orthotropic. For both cases, the effective thickness is calculated from Equation 2.3. The isotropic model assumes the same elastic modulus in each direction, calculated per Equation 2.4. This provides a good approximation of the bending stiffness EI and axial stiffness EA of the real plate in the circumferential direction, but significantly overestimates the longitudinal bending stiffness. The orthotropic model assigns different elastic properties in the circumferential and longitudinal directions, resulting in a longitudinal bending stiffness that is about 150 times lower than the circumferential bending stiffness (a much better approximation to the actual plate behaviour that is achieved with the isotropic model). Given the lack of available information about the backfill material, two different soil moduli, 30 MPa and 80 MPa,

were selected for the analysis on the basis that they represent probable upper and lower-bound values for the depths of backfill considered.

Moore and Brachman drew the following conclusions based on their study:

- The general pattern of thrust predicted by the 3D FE analysis is superior to 2D FE analysis.
- Although circumferential thrust estimates were somewhat influenced by the modulus of the soil, large adjustment of the soil modulus had a reasonably small effect. Other quantities such as circumferential bending moments and deflections may be more sensitive to soil modulus but were not considered in this study.
- Analysis using the orthotropic structural theory suggested it may not be essential to model the low longitudinal bending stiffness of the pipe. However, excessive estimates of thrusts at locations away from the vehicle load suggest that the use of long prismatic geometry may not be valid.

2.6.2 Girges and Abdel-Sayed, 1995

A comparative study of the results obtained from three-dimensional and two-dimensional FE analyses of a circular CMP subjected to live loading was carried out by Girges and Abdel-Sayed (1995). The CMP used in the study had a diameter of 7.6 m and a length of 30 m (for the 3D analysis). The pipe plate profile was 152 x 51 mm (pitch by depth) with a wall thickness of 7.0 mm. The steel was assumed to have an elastic modulus of 200 GPa and a Poisson's ratio of 0.3, while the soil modulus of elasticity and Poisson's ration were taken as 35 MPa and 0.35, respectively. The following conclusions were drawn based on the results of the study:

- Based on the 3D FE analysis, vertical pressure in the cover soil dissipated with a slope of 1 vertical to 1 horizontal (1V:1H) in the transverse direction, which was the same applied by the OHBDC. In the longitudinal direction, however, the pressure dissipated at 5V:1H, compared to the slope of 2V:1H recommended by OHBDC or AASHTO's specified slope of 1V:0.875H.

- The magnitude of thrust did not differ appreciatively when comparing the 3D and 2D models, although there was a significant reduction in bending moments, especially at the crown.

2.6.3 El-Sawy, 2003

El-Sawy (2003) performed three-dimensional FE analyses of two (2) culverts previously field tested by Bakht (1980), namely the circular Deux Rivières culvert and the horizontally elliptical Adelaide Creek culvert. Two (2) different geometries were considered for the Deux Rivières culvert: the actual geometry (

Figure **2.19**(a)), in which the geometry at the ends of the culvert is explicitly modelled, and a long prismatic geometry (

Figure **2.19**(b)), in which it is implicitly assumed that the ends of the culvert do not significantly affect the response of the central section. Both isotropic and orthotropic structural shell (plate) theories were used for the CMP. For the orthotropic case, the effective plate thickness and elastic modulus in the circumferential direction are calculated from Equations 2.3 and 2.4. The effective elastic modulus in the longitudinal direction is calculated from Equation 2.5. This produces a longitudinal axial stiffness equal to that of the actual corrugated plate, but significantly overestimates the longitudinal bending stiffness (it is only possible to satisfy one of these, along with accurate axial and bending stiffness in the circumferential direction). This approach contrasts with that of Moore and Brachman (1994), whose orthotropic model satisfied the longitudinal bending stiffness but overestimated the longitudinal axial stiffness.

$$\bar{t} = \sqrt{\frac{12I_p}{A_p}} \qquad 2.24$$

$$\bar{E}_{circumferential} = \bar{E}_\theta = \frac{12E_pI_p}{\bar{t}^3} \qquad 2.25$$

$$\bar{E}_{longitudinal} = \bar{E}_L = \frac{A_pE_p}{\bar{t}} \qquad 2.26$$

Soil was assumed to behave elastically with the same two values of elastic modulus used by Moore and Brachman, namely 30 MPa and 80 MPa. No attempt was made to model the culvert response during construction and earth loading due to a lack of available information. Consequently, the results from the FEA are due to live loads only.

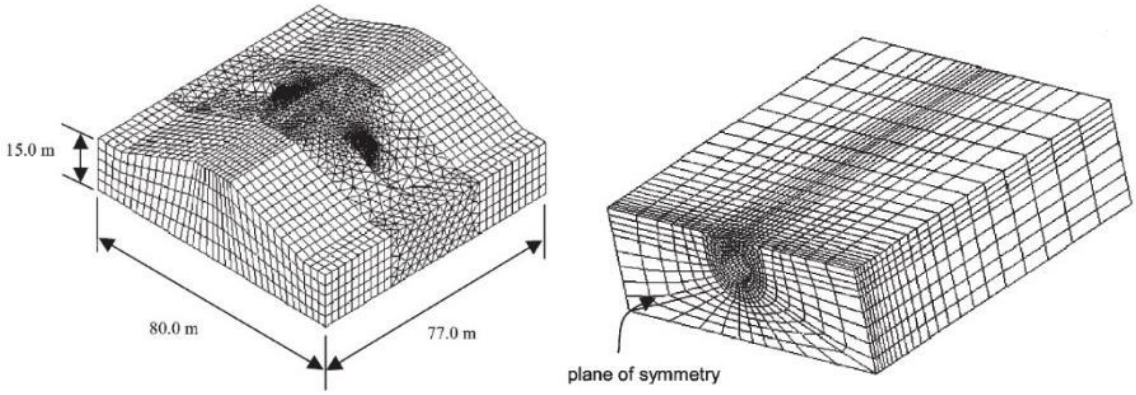

(a) (b)

Figure 2.19 Geometries used in the 3D FE models of El-Sawy(2003): (a) actual; and b) long prismatic.

The following observations were made based on the results of the FE analyses of the circular Deux Rivières culvert:

- The isotropic culvert model produced poor results (significantly overestimated the circumferential thrusts and produced unrealistically high values of longitudinal thrust).
- The orthotropic culvert model produced circumferential thrust distributions that agree more closely with the experimental values (Bakht, 1980) than the predictions of Moore and Brachman (1994). It was suspected that this is due to the different orthotropic plate model used (i.e. accurate longitudinal axial stiffness instead of accurate longitudinal bending stiffness).
- The orthotropic 3D FE model provided good estimates of maximum circumferential thrusts (located at the shoulders), which were about 33% higher than experimental values. Bending moments showed less agreement,

indicating that they may be more sensitive to proper modelling of the soil behaviour and soil-structure interaction effects.

- Circumferential thrusts decay in a short distance in the longitudinal direction, which justifies the use of the long prismatic geometry.

2.6.4 El-Taher and Moore, 2008

EL-Taher and Moore (2008) performed the first numerical study of the remaining structural capacity of corroded CMP culverts. They carried out a parametric study using 2D FE models that considered circular pipes with corrosion along the bottom half.

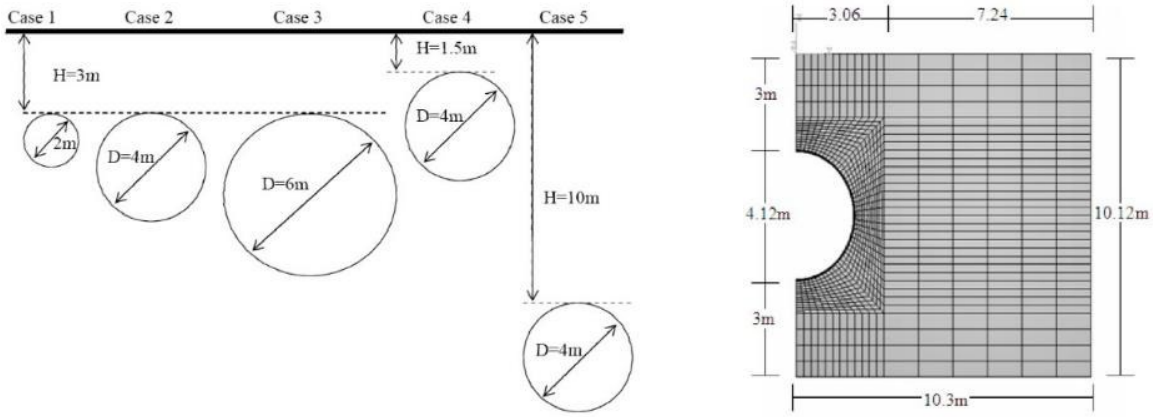

Figure 2.20 Design cases and typical finite element mesh used by El-Taher and Moore (2008)

The five design cases considered in the study are shown in Figure 2.20, along with the FE mesh for design case 2. Test variables included the circumferential extent of corrosion across the invert (90˚, 135˚, and 180˚), percentage of remaining plate thickness (100%, 42.5%, 12.5%, and 1.5%), pipe diameter (2.0 m, 4.0 m, and 6.0 m), and cover depth (1.5 m, 3.0 m, and 10 m). A corrugation profile of 152 x 51 mm, intact plate thickness of 3.0 mm, elastic modulus of 200 GPa, moment of inertia of 1,057.25 mm^4/mm, and cross-sectional area of 3.522 mm^2/mm was used for each analysis. Four equal rows of solid rectangular elements were used to model the CMP with a total thickness defined by Equation 2.3. The effective modulus of elasticity, assigned

in accordance with Equation 2.4, produces values of circumferential normal stiffness, $(EA)_\theta$, and flexural rigidity, $(EI)_\theta$, comparable to those of the actual plate. To simulate the reduction in pipe thickness associated with corrosion (which was approximated as occurring uniformly across the invert), rows of elements were progressively removed from the inside of the pipe.

$$\bar{t} = \sqrt{\frac{12E_pI_p}{E_pA_p}} \qquad 2.27$$

$$\bar{E} = \frac{E_pA_p}{\bar{t}} \qquad 2.28$$

Well-graded granular soil was considered as the backfill material modelled using linear-elastic behaviour. The 2D FE analyses considered the CMPs to be buried in their initial state (i.e. pipe response during construction and earth loading was not modelled), and did not include the application of live loads. Test models (considering the pipe in an intact, buried state) were successfully calibrated against closed form solutions prior to simulating corrosion. Changes in the factor of safety against yielding, FS_y, and factor of safety against buckling, FS_b, are assessed as corrosion develops. Two primary conclusions are:

- The factor of safety against yielding FS_y decreases almost linearly with decreasing plate thickness (Figure 2.21). This occurs because the reduction in thickness across the invert has minimal effect on the total thrusts and bending moments in the pipe.
- Yielding remained the critical design condition for the studied cases. Reductions in buckling stability are not likely important unless the structure is buried in poor quality backfill soil.

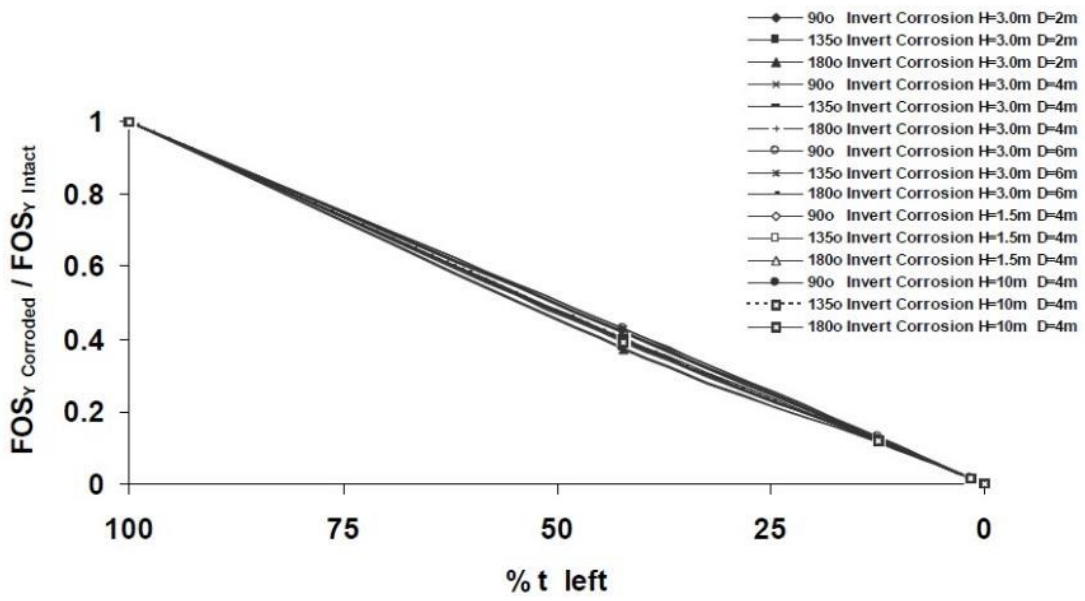

Figure 2.21 Reductions in stability against yield versus percentage of original plate thickness (El-Taher & Moore, 2008)

2.6.5 Mai, 2014

Mai et al. (2014b) conducted 2D FE analyses to predict the structural response of two (2) culverts prior to the experiments described in section 2.5.3 (Mai et al., 2014a).

All the analyses in this study employed linear-elastic soil behaviour. Values of elastic modulus for the 95% SPD backfill were calculated using the method proposed by Scott et al. (1977). The soil modulus for the loose sidefill around CSP1 was calculated based on confined pressure (Selig, 1990). Constant soil modulus with depth was assumed to simplify the FE analysis. The interface between the soil and the corrugated pipe was modelled as rigid (fully bonded) for all cases.

The corrugated pipes were modelled in two dimensions using a plain shell with "equivalent" properties calculated from Equations 2.24 and 2.25. Two different finite element software packages, CANDE-2007 Level 2 and ABAQUS version 6.9, were used to compare their performance. With ABAQUS, it was possible to define various thicknesses around the pipe circumference. The pipe circumference was therefore divided into nine sections and assigned effective properties based on the actual average remaining wall thicknesses, which were previously measured using an

ultrasonic gauge (Mai et al., 2012). Table 2.4 summarizes the properties of the plain shell used to model CSP1 (denoted as the "beam element approach"), along with the corresponding properties of the actual, corrugated section. Modelling the thickness variations in CANDE is not possible, and therefore the average minimum thickness was used to model the whole culvert.

Table 2.4 Bending and hoop stiffness of plain and corrugated section for CSP1 (Mai et al., 2014b).

		Beam element approach				Corrugated section			
	Angle from the invert	$\bar{E}$ (GPa)	$\bar{t}$ (mm)	EI × 10^3 (Nm²/m)	EA × 10^6 (N/m)	$\bar{E}$ (GPa)	$\bar{t}$ (mm)	EI × 10^3 (Nm²/m)	EA × 10^6 (N/m)
S1	33.75–45° (L[a])	51.5	15.3	15.3	787	200	3.64	15.3	787
S2	22.5–33.75° (L)	46.9	15.3	13.9	716	200	3.31	13.9	716
S3	11.25–22.5° (L)	53.4	15.3	15.9	816	200	3.78	15.9	816
S4	0–11.25° (L)	61.7	15.3	18.5	945	200	4.37	18.5	945
S5	0–11.25° (R[b])	57.3	15.3	17.2	878	200	4.06	17.2	878
S6	11.25–22.5° (R)	37.0	15.2	10.9	563	200	2.60	10.9	563
S7	22.5–33.75° (R)	33.5	15.2	9.8	508	200	2.35	9.8	508
S8	33.75° to 45° (R)	48.9	15.3	15.6	748	200	3.46	15.6	748
Intact	45°–45°R[c]	63.6	15.3	19.1	975	200	4.51	19.1	975

[a] On the left side of the invert in the 2-D model.
[b] On the right side of the invert in the 2-D model.
[c] The section haunch-crown-haunch of the 2-D model remains intact.

The finite element mesh used in the buried pipe models is shown in Figure 2.22. Simulation of the effect of backfilling was achieved by first activating the bedding and pipe, then activating each soil layer (150 mm-thick for CSP1 and 300 mm-thick for CSP2) in successive stages. No attempt was made to account for the residual horizontal earth pressures induced by compaction and their associated effects on pipe deflections during sidefilling. The vertical boundaries were set at 3.1 m (or 1.7 times the pipe diameter) from the edge of the pipe, and the distance between the invert and the bottom boundary was 0.7 m.

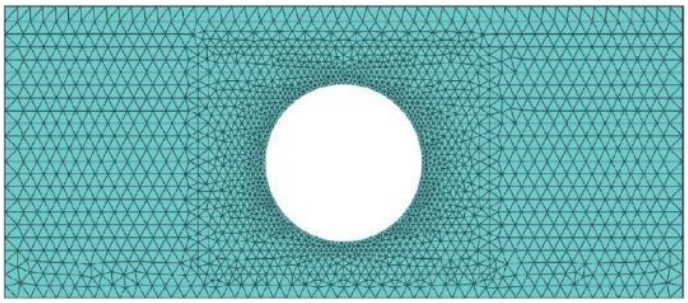

Figure 2.22 ABAQUS FE mesh used in analyses by Mai et al. (2014b).

The surface live load was simulated by applying a uniform pressure with a width of 250 mm positioned at the centreline of the pipe. Several different approaches were used to convert the 3D live load into an "equivalent" 2D line load, i.e. methods by Katona (1976) and Moore (McGrath et al., 2002) for the single axle (SA) load, and the method of Petersen et al. (2010) for the single wheel pair (SW) load.

Comparison of pipe deflections and thrust forces produced by the 2D FE models to the experimental results revealed the following:

- All models produced linear relationships between deflection and applied load, and between thrust force and applied load. Experimental results, however, are non-linear, especially for more deteriorated CSP1. This is the main reason for this difference is likely the linear-elastic material models used to model the soil and pipe.
- Both models overestimate the horizontal diameter change, which was negligible.
- The results suggest that heavily deteriorated culverts cannot be adequately modelled with current methods, but that CANDE can be used in favour of more complex software to model relatively intact corrugated metal culverts.

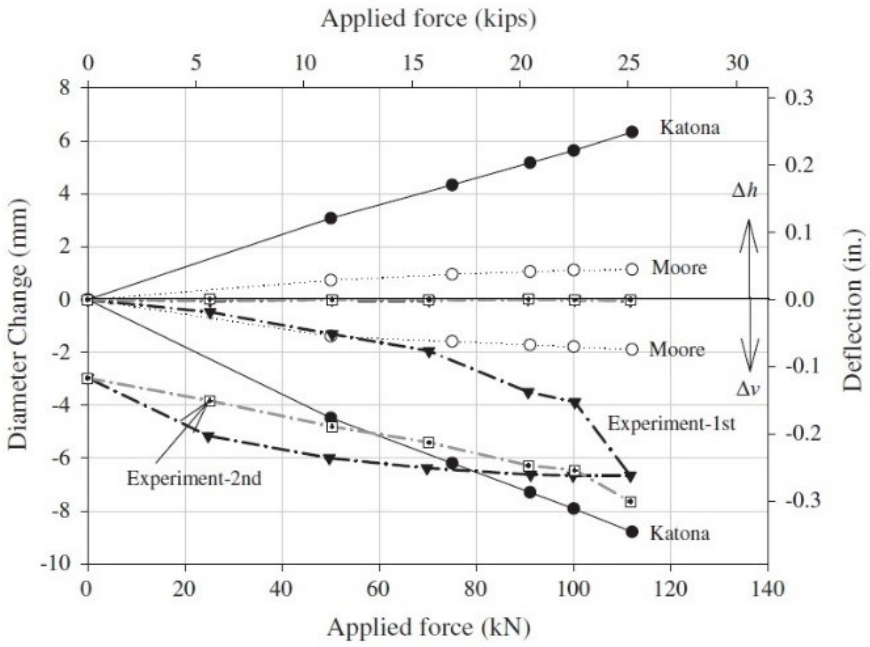

Figure 2.23 Horizontal and vertical diameter change of CSP2 during the test with axle load and 0.6 m cover (Mai et al., 2014b).

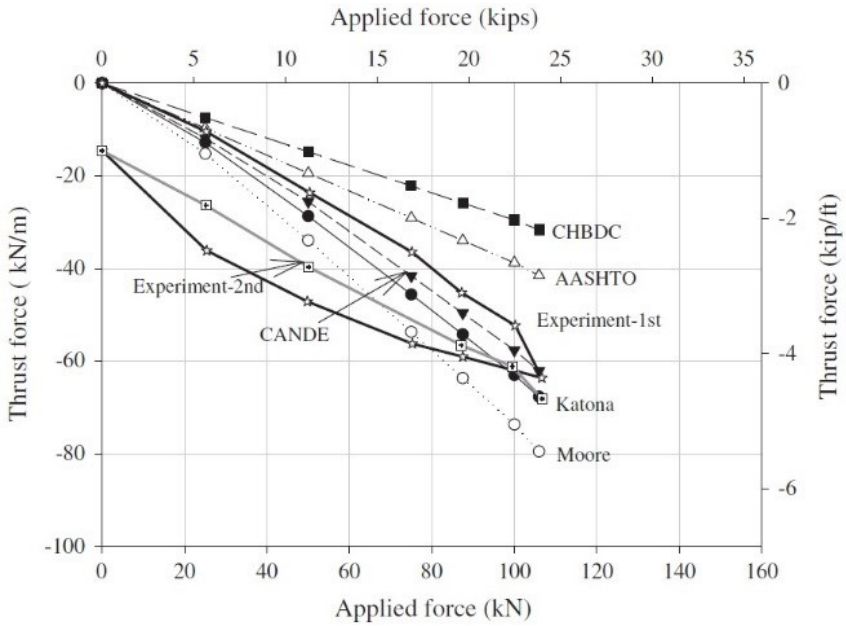

Figure 2.24 Maximum thrust force under live load for CSP2 with axle load and 0.9 m cover (Mai et al., 2014b).

CHAPTER 3:
DEVELOPMENT OF A THREE-DIMENSIONAL FINITE ELEMENT MODEL FOR CORRUGATED METAL PIPE CULVERTS

3.1 Introduction

In recent years, two-dimensional (2D) finite element (FE) modelling has been used to explore how the structural integrity of a corrugated metal pipe (CMP) culvert is affected by degradation of one or both of its constituent materials (i.e. the pipe metal and/or surrounding soil). The stability of deteriorated culverts under dead loading (El-Taher & Moore, 2008) and live loading (Mai et al., 2014b) have been examined. Although much understanding has been gained from this research, several simplifying assumptions were inherent in these models which may limit their ability to provide further insight into the problem. Most prominently, perhaps, is the use of linear elastic constitutive soil models together with fully bonded conditions at the soil-pipe interface. The mechanical behaviour of real soil involves a significant degree of non-linearity. In soil-structure interaction problems such as the one considered here, it seems reasonable to expect that the non-linear behaviour of the soil—together with that of the soil-structure interface—would have an effect on the response of the structure. Furthermore, 2D models are limited in their ability to account for certain aspects of the actual, 3D problem. Such aspects include surface live load spreading through the cover soil, the structural behaviour of a corrugated pipe, and the influence of corrosion patterns that vary in both the longitudinal and circumferential directions of the CMP. Although many 3D models have been developed for intact corrugated metal culverts subjected to live loading (e.g. Girges & Abdel-Sayed (1995), El-Sawy (2003), MacDonald (2010), Elshimi (2011)), none of them (to the knowledge of the author) have been used to investigate the influence of corrosion. This chapter details the development of a comprehensive, 3D, non-linear

FE model capable of simulating the behaviour of both intact and corroded CMP culverts.

3.2 Experimental Details

The full-scale laboratory experiments carried out by Mai et al. (2014a) at Queen's University are considered here for validation of the new, 3D model. Specifically, the intact culvert from the experiment—which is referred to as CSP2—is modelled during construction (dead loading) and under live loading conditions, using the approach described in the following sections. This experiment was selected for calibration purposes due to the availability of well-documented details (e.g. geometry, material properties, test methodology, etc.), in addition to the comparatively high degree of accuracy that might be expected for measurements made in a controlled laboratory environment versus those made in the field.

3.3 Numerical Details

3.3.1 General

The commercially-available geotechnical engineering finite element software package Plaxis 3D AE.01 (Brinkgreve, 2015) was used to develop the model described herein. Numerical methods such as the finite element method (Zienkiewicz & Taylor, 2005) are well suited to deal with complex boundary value problems such as those involving soil-structure interaction. The first step in the finite element method is to discretize the entire problem domain into a finite number of geometric entities (volumes, areas, and/or lines), which are referred to as "elements". Adjacent elements are connected to one another by shared points, or "nodes", which, at a minimum, are located at the corners of the elements (for line elements, nodes are located at each end). Equilibrium and compatibility conditions are satisfied at each node by solving a set of simultaneous equations of the following general form for each element:

$$\{f\} = [K]\{u\}, \tag{3.1}$$

Where {f} is a vector of nodal forces, [K] is the element stiffness matrix, and {u} is a vector of nodal displacements. The total force is applied in incremental (load) steps, and the equations for each step are solved in an iterative manner until some specified convergence criteria are reached. Once the displacements are known, then the strains and stresses can be determined.

3.3.2 Mesh and Boundary Conditions

The total dimensions of the 3D model measured 8.0 m-long, 6.0 m-wide, and 3.4 m-high. The extents of the side and bottom boundaries of the model correspond to those of the walls and floor of the concrete test pit that was used in the experiment, respectively. Therefore, any end effects that may influence the results of the 3D model should have also been present in the experiment. Default boundary conditions were maintained at all stages of the analyses (i.e. top = free, sides = normally fixed, and bottom = fully fixed).

The soil continuum in Plaxis 3D is discretized into ten-noded tetrahedral (3D) soil elements. The CMP was modelled using plates, which are discretized into six-noded, triangular (2D) plate elements. The interface between the soil and the CMP was modelled using interface elements, which consist of pairs of nodes that are compatible with the six-noded triangular side of a soil or plate element. The mesh was automatically generated by specifying a global coarseness value of "fine" (which corresponds to a relative element size factor, r_e, equal to 0.7 at the outer regions of the model, with local refinement (r_e = 0.5) near the CMP. The resulting mesh consisted of 179,069 soil elements and 258,844 nodes.

3.3.3 CMP

Ideally, the geometry of the CMP would be explicitly modelled in three dimensions using volume (or "soil") elements. This way, the development of corrosion (i.e. progressive reduction in thickness of the pipe plate) could be modelled simply by deactivating incremental layers of the CMP volume in successive calculation phases. However, since the corrugation profile of the pipe plate (67.7 mm-pitch by 12.7 mm-

depth by 4.5 mm-thick) in this case is very fine relative to the total dimensions of the model, this approach would require an extremely large number of very small elements. In the current version of Plaxis 3D, this causes the 3.6 GB RAM memory limit of the input program to be exceeded. Therefore, the common approach of modelling the corrugated plate of the pipe as an "equivalent" plain plate with orthotropic material properties was adopted.

The structural response of a pipe is controlled by its flexural rigidity, *EI*, and axial stiffness, *EA*, where *E, I,* and *A* are the elastic modulus, moment of inertia, and cross-sectional area of the pipe plate, respectively. A corrugated plate has unique values of flexural rigidity and axial stiffness in the directions perpendicular and parallel to the corrugations. For a corrugated pipe, these directions correspond to the longitudinal and circumferential (denoted by the subscripts '$_L$' and '$_\theta$') directions of the pipe, respectively. Since the pipe is materially isotropic (it has the same value of elastic modulus in all directions, i.e. $E_L = E_\theta = E$), its anisotropic behaviour is due to directionally-dependent geometric properties ($I_L < I_\theta$ and $A_L < A_\theta$). Upon converting the corrugated plate to an "equivalent" plain plate, the same rectangular cross-section results in both directions (i.e. $\bar{I}_L = \bar{I}_\theta = \bar{I}$, and $\bar{A}_L = \bar{A}_\theta = \bar{A}$). Therefore, orthotropic values of elastic moduli, $\bar{E}_L$ and $\bar{E}_\theta$, are assigned such that $EI_L = \bar{E}_L\bar{I}$ and $EI_\theta = \bar{E}_\theta\bar{I}$. The properties of the equivalent orthotropic plate were computed using Equations 3.2 through 3.9 (Aagah & Aryannejad, 2014).

$$\bar{t} = \sqrt{\frac{12I}{\mathrm{A}}} \tag{3.2}$$

$$\bar{\gamma} = \frac{\gamma A}{\bar{A}} \tag{3.3}$$

$$\bar{E}_\theta = \frac{EI_\theta}{\bar{I}} \tag{3.4}$$

$$\bar{E}_L = \frac{EI_L}{\bar{I}} \tag{3.5}$$

$$\bar{\nu} = 0 \tag{3.6}$$

$$\bar{G}_{\theta R} = \frac{\bar{E}_{\theta}}{2(1+\nu)} \quad 3.7$$

$$\bar{G}_{LR} = \frac{\bar{E}_{L}}{2(1+\nu)} \quad 3.8$$

$$\bar{G}_{\theta L} = \frac{\sqrt{\bar{E}_{\theta} + \bar{E}_{L}}}{2(1+\nu)} \quad 3.9$$

where,

$\bar{t}$ = thickness of the orthotropic plate;

$\bar{\gamma}$ = unit weight of the orthotropic plate;

$\bar{E}_{\theta}$ = elastic modulus of the orthotropic plate in the longitudinal direction;

$\bar{E}_{L}$ = elastic modulus of the orthotropic plate in the circumferential direction;

$\bar{\nu}$ = Poisson's ratio of the orthotropic plate;

$\bar{G}_{\theta R}$ = circumferential out-of-plane shear modulus of the orthotropic plate;

$\bar{G}_{LR}$ = longitudinal out-of-plane shear modulus of the orthotropic plate; and

$\bar{G}_{\theta L}$ = in-plane shear modulus of the orthotropic plate.

It should be noted that by using the above equations, only three (3) out of the four (4) flexural rigidity/axial stiffness values are accurately modelled. While the flexural rigidity calculated for the orthotropic plate is equal to that of the actual plate in both directions, the axial stiffness of the orthotropic plate is only accurate in the circumferential direction (i.e. $EA_{\theta} = \bar{E}_{\theta}\bar{A}$, but $EA_{L} \neq \bar{E}_{L}\bar{A}$). The longitudinal axial stiffness of the orthotropic plate, in this case, is underestimated by approximately 25%.

Plaxis 3D uses a local coordinate system for plates that consists of orthogonal axes 1, 2, and 3. The local axes of the plate in the 3D model were oriented such that axes 1, 2, and 3 coincide with the longitudinal (L), circumferential (θ), and radial (R) directions of the pipe, respectively. The conventions for the structural forces computed by Plaxis based on the local coordinates are shown in Figure 3.1.

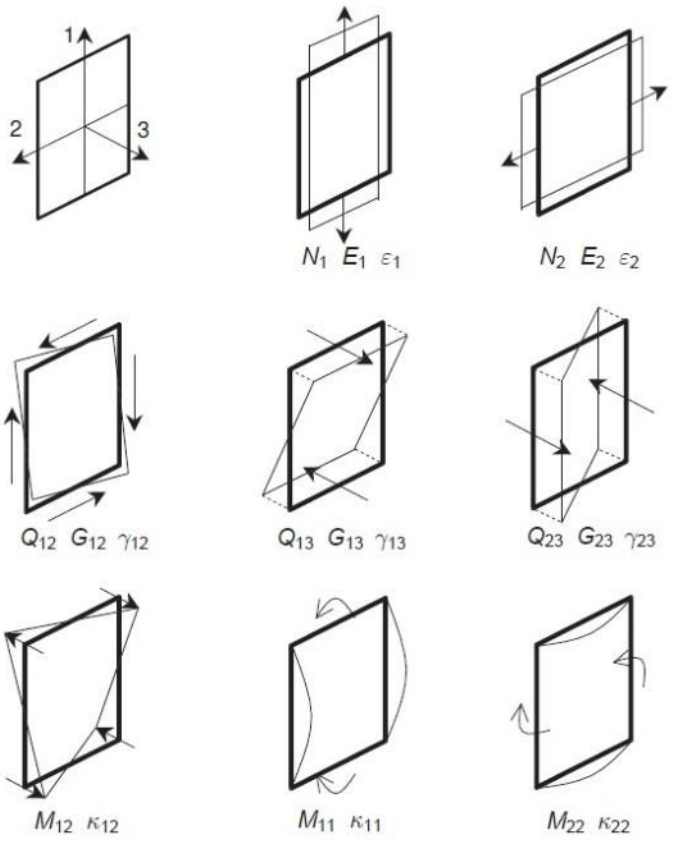

Figure 3.1 Definition of positive normal forces (N), shear forces (Q), and bending moments (M) for structural plate elements based on a local system of axes (Plaxis bv, 2013).

Actual (isotropic) properties of the intact CMP plate are given in Table 3.1. The equivalent (orthotropic) plate properties are given in Table 3.2. The severity of corrosion is described in terms of the percentage of the intact plate thickness remaining, P_t. Since the objective here is simply to demonstrate that the model is capable of accounting for the effects of corrosion, analyses are only conducted for values of P_t equal to 100 % (i.e. fully intact), 50%, and 10%. For the same reason, the effects of corrosion are assumed to be uniformly distributed along the length and around the circumference of the pipe.

Table 3.1 Actual (isotopic) material properties of the intact and corroded CMPs.

Parameter	Symbol	Value	Units
Plate thickness	t	4.50	mm
Unit weight	γ	77	kN/m^3
Elastic modulus	E	200	GPa
Cross-sectional area	A	4.87	mm^2/mm
Moment of inertia	I	95.28	mm^4/mm
Poisson's ratio	ν	0.3	-

Table 3.2 Equivalent (orthotropic) material properties of the intact and corroded CMP.

Parameter		Symbol	Value	Units
Plate thickness		$\bar{t}$	15.32	mm
Unit weight		γ	24.47	kN/m^3
Elastic moduli	Circumferential	$\bar{E}_\theta$	63,567,033	kPa
	Longitudinal	$\bar{E}_L$	5,066,248	kPa
Poisson's ratio		$\bar{\nu}$	0	-
Shear moduli	Circumferential Out-of-plane	$\bar{G}_{\theta R}$	24,488,859	kPa
	Longitudinal Out-of-plane	$\bar{G}_{LR}$	1,948,557	kPa
	In-plane	$\bar{G}_{\theta L}$	6,902,173	kPa
Cross-sectional area		$\bar{A}$	15.32	mm^2/mm
Moment of inertia		$\bar{I}$	299.78	mm^4/mm

3.3.4 Soil

The actual behaviour of soil can be simulated to various degrees of accuracy depending on the constitutive model used. Simple soil models are advantageous in the sense that they require fewer input parameters and result in relatively quick calculation times. More advanced soil models generally have more inputs (some of which may be difficult to estimate or measure) and are computationally expensive,

but often produce more realistic results. Three different constitutive soil models from the Plaxis 3D library were evaluated in developing the model: Linear Elastic, Mohr-Coulomb, and Hardening Soil.

3.3.4.1 Linear Elastic model

The Linear Elastic (LE) model is the simplest of the three soil models used in this study. It is based on Hooke's Law of isotropic elasticity and has only two primary input parameters: Young's modulus, E, and Poisson's ratio, ν. The former defines the slope of the normal stress-strain curve, while the latter defines the ratio of normal strains that occur in planes perpendicular and parallel to the direction of the applied stress. It is possible to use Poisson's ratio creatively, together with Plaxis 3D's staged construction mode, to obtain soil stress states that cannot be generated by gravity loading alone (as explained in section 3.3.7). All strains in the LE model are fully reversible, and the soil is assumed to have infinite strength. Although the LE model is generally considered to be inadequate for modelling soil, it produces very fast calculation times and is unlikely to result in numerical instability. As such, the LE model may still be useful for obtaining a quick first approximation of the problem and to help evaluate the modelling procedure. The soil properties used for the LE soil model are given in Table 3.3.

Table 3.3 Soil properties used for LE soil model.

Parameter	Symbol	Value	Units
Unit weight	γ_s	21.9	kN/m^3
Elastic modulus	E_s	60,000	kPa
Poisson's ratio	ν	0.3	-

3.3.4.2 Mohr-Coulomb model

The Mohr-Coulomb (MC) model is a linear elastic, perfectly plastic model, and is of intermediate complexity. The MC model behaves the same as the LE model, provided the maximum shear stress in the soil remains less than the soil's shear strength.

However, at any specific point in the soil, no additional normal stress can be applied once the shear strength is exceeded. Furthermore, all strains that occur beyond this point are irreversible. The shear strength of the soil is defined by the well-known Mohr-Coulomb failure criterion, i.e.:

$$\tau_s = c' + \sigma' \tan \varphi'; \qquad 3.10$$

where c' is the effective cohesion, φ' is the effective internal friction angle of the soil, and σ' is the effective stress acting normal to the potential failure plane. All soils in this study are assumed to be dry (i.e. $\sigma' = \sigma$). The total strain, ε, is the sum of the elastic (fully recoverable) strain, ε^e, and plastic (irrecoverable) strain, ε^p. The soil stiffness is the same during unloading as it is during loading, as illustrated in Figure 3.2.

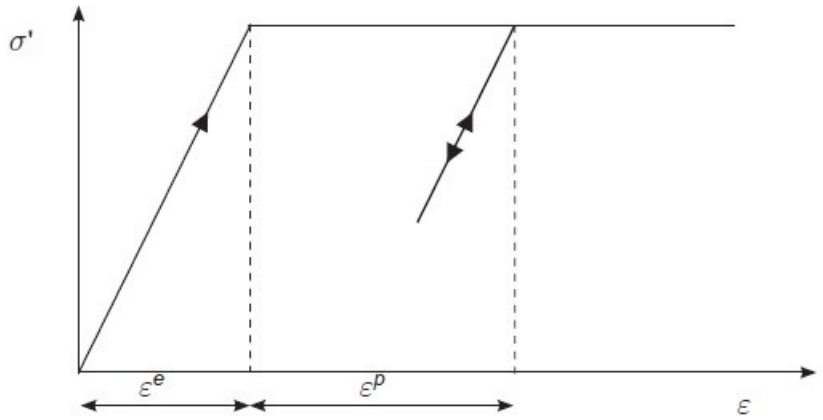

Figure 3.2 Typical linear elastic-perfectly plastic model (Plaxis bv, 2015).

The MC model has five primary input parameters: E, ν, c', φ', and ψ'. The angle of dilation, ψ', defines the amount of volumetric strain that occurs during shearing. A significant shortcoming of the MC model is that Young's modulus is assumed to be constant with depth. The stiffness of a real soil is highly dependent on the stress level. The assumption of constant stiffness saves on computational effort, but may not produce realistic deformations in certain situations. The soil properties used for the MC model are given in Table 3.4.

Table 3.4 Soil properties used for MC soil model.

Parameter	Symbol	Value	Units
Unit weight	γ_s	21.9	kN/m^3
Elastic modulus	E_s	60,000	kPa
Poisson's ratio	ν	0.3	-
Cohesion	c'	5	kPa
Friction angle	φ'	40	°
Dilation angle	ψ'	0	°

3.3.4.3 Hardening Soil model

The Hardening Soil (HS) model is an advanced model that is based on the theory of plasticity, and which is capable of simulating many of the important aspects of soil behaviour. Most notably, it accounts for the fact that soil stiffness is dependent on the stress level, as well as on the stress path history of the soil. This is accomplished by using three different stiffness parameters: the triaxial loading (secant) modulus, E_{50}; the triaxial unloading-reloading modulus, E_{ur}, and the oedometer loading modulus, E_{oed}. All three moduli are stress-dependent; their input values in Plaxis 3D (i.e. E_{50}^{ref}, E_{oed}^{ref}, and E_{ur}^{ref}) each relate to a common reference pressure, p_{ref}, for which the default value of 100 kPa was used. A total of seven (7) primary input parameters are required: E_{50}^{ref}, E_{oed}^{ref}, E_{ur}^{ref}, ν, c', φ', and ψ'. The over-consolidation ratio, *OCR*, can also be specified and accounted for during initial stress generation.

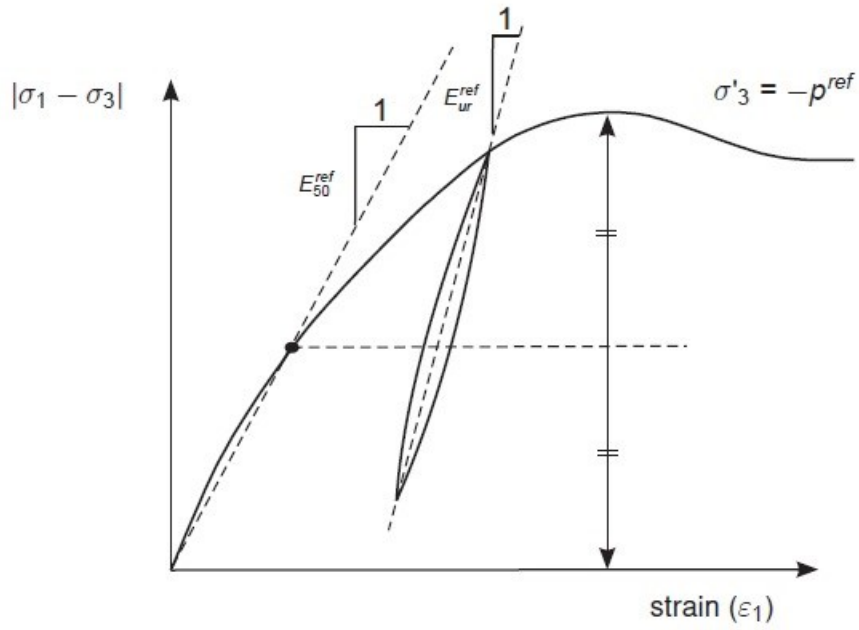

Figure 3.3 Definition of E_{50}^{ref} and E_{ur}^{ref} for drained triaxial test results (Plaxis bv, 2015).

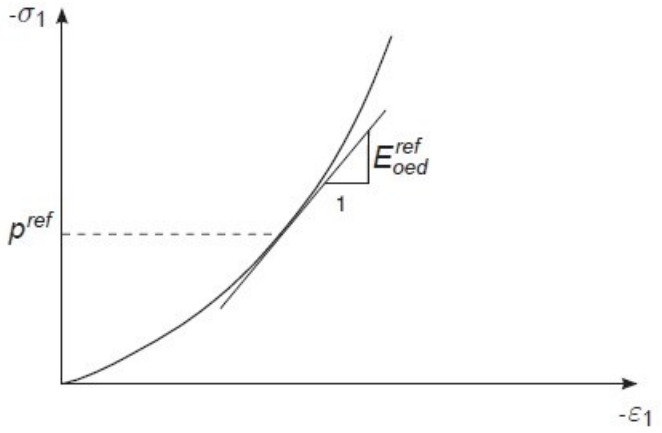

Figure 3.4 Definition of E_{oed}^{ref} for oedometer test results (Plaxis bv, 2015).

In contrast to the MC model, the yield surface of the HS model is not fixed; it can expand due to plastic straining (Figure 3.5). The shear yield surface can expand up to the ultimate Mohr-Coulomb failure surface, and this phenomenon is referred to as strain hardening. The HS model also includes a second type of yield surface to close the elastic region for isotropic compression. This surface is known as the cap yield surface and expands as a function of the pre-consolidation stress. The total yield contour of the HS model is shown in Figure 3.6.

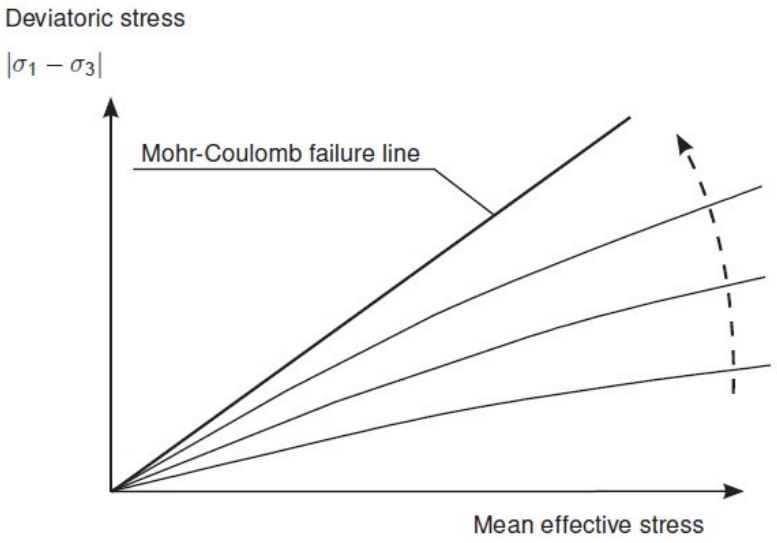

Figure 3.5 Expanding yield loci with increasing plastic shear strain (Plaxis bv, 2015).

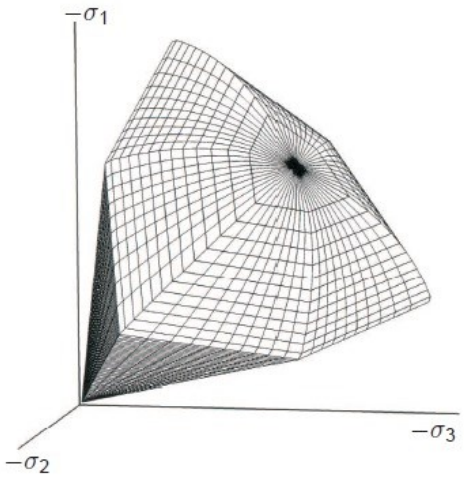

Figure 3.6 Representation of total yield contour of the HS model in principal stress space (Plaxis bv, 2015).

Although it demands greater computational effort and produces longer calculation times than the MC and LE models, the HS model may produce more accurate results for certain types of problems. It is worth noting that the HS model still neglects several aspects of real soil behaviour, including strain softening due to soil dilatancy and de-bonding effects; the effects of cyclic loading and cyclic mobility; and the higher soil stiffness that exists at small strain levels. The soil properties used for the HS soil model are given in Table 3.5.

Table 3.5 Soil properties used for HS soil model.

Parameter	Symbol	Value	Units
Unit weight	γ_s	21.9	kN/m^3
Secant modulus	E_{50}^{ref}	60,000	kPa
Oedometer modulus	E_{oed}^{ref}	48,000	kPa
Unloading-reloading modulus	E_{ur}^{ref}	180,000	kPa
Poisson's ratio	ν	0.3	-
Cohesion	c'	5	kPa
Friction angle	φ'	40	°
Dilation angle	ψ'	0	°

3.3.5 Soil-Pipe Interface

The interface between the soil and the CMP is physically different from the contact between adjacent volumes of soil, and thus its mechanical behaviour is also unique. Specifically, the strength and stiffness of the interface may be less than that of the soil. When the shear or tensile strength of the interface is exceeded, slippage and gapping can occur and affect the forces that are transmitted to the pipe.

Interfaces have traditionally been modelled using a Mohr-Coulomb model. The parameters c' and φ' are analogous to the adhesion between the soil and the CMP, and the interface friction angle, respectively. These parameters can be obtained from the results of direct shear tests. In Plaxis 3D, strength and stiffness parameters can be assigned to the interface independent of the soil parameters. Alternatively, the strength and stiffness of the interface can be taken as a percentage of the values of the adjacent soil, using a strength reduction factor, R_{inter} (where $0.01 < R_{inter} < 1.0$). When R_{inter} is used, and the adjacent soil is the LE model, only the stiffness of the interface is reduced, while slippage/gapping cannot occur. When the adjacent soil is modelled using a more advance soil model, such as the HS model, only the relevant parameters (c', φ', ψ', $E = E_{ur}$, and ν) are picked up. In this study, only one interface condition is considered, in which the interface parameters are taken from the adjacent soil using $R_{inter} = 0.6$ (Allen, et al, 1988).

3.3.6 Modelling Sequence

The model was analyzed at various stages using Plaxis 3D's staged construction mode. Three main states were examined:

1. Dead loading of intact culvert;
2. Dead + live loading of intact culvert; and
3. Dead + live loading of corroded culvert.

Each of these major states was further subdivided into several phases, such that the model results could be analyzed at intermediate stages during dead and live loading.

3.3.6.1 Dead Loading

The modelling sequence for the construction (i.e. dead loading) of the culvert is illustrated in Figure 3.7. Here, a simplified case is presented, in which compaction effects are ignored. Incorporating the effects of compaction, as described in section 3.3.7, requires an additional phase for each layer that is compacted.

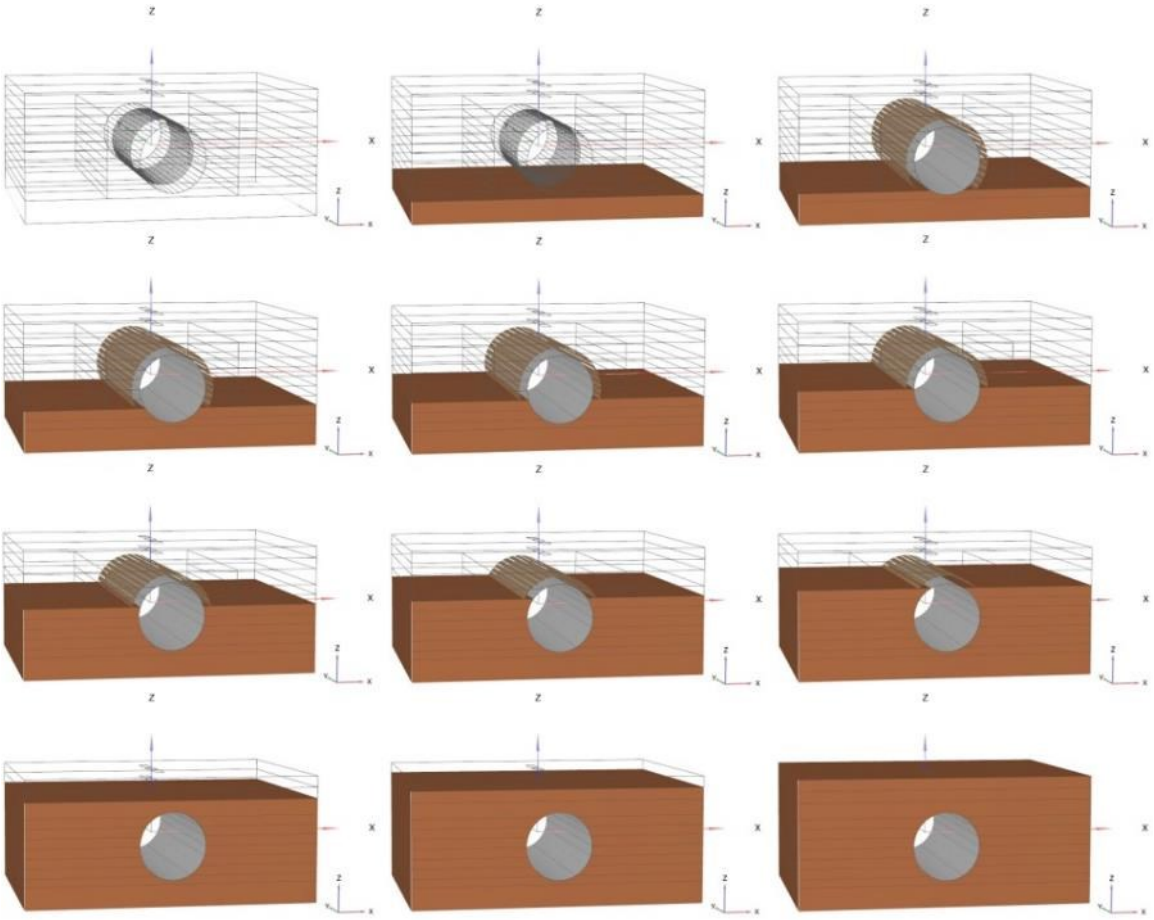

Figure 3.7 Modeling sequence for culvert construction without compaction effects.

In the first phase, the bottom layer (0.6 m-thick) was activated. In phase 2, the 100 mm-thick bedding, the CMP, and the soil-CMP interface were activated. The sidefill was activated in six (6) layers (approximately 0.3 m-thick each) in phases 3 to 8. In phases 9 to 11, 0.3 m of cover soil is progressively activated, up to a total cover depth of 0.9 m.

3.3.6.2 Live Loading of Intact Culvert

Live loading of CSP2 was modelled for the four load cases shown in Table 2.3. The total applied force was converted to a uniformly-distributed surface load and applied to a rectangular loading plate at the ground surface. The loading plate was 0.6 m-long by 0.25 m-wide (area = 0.15 m^2) and positioned at the centreline of the culvert (both longitudinally and transversely). The total live load was applied in incremental

phases such that the load-deflection response of the model culvert could be analyzed and compared to the experimental measurements.

3.3.6.3 Live Loading of Corroded Culvert

Live loading of the corroded culvert was modelled in a similar manner to that of the intact culvert, except that the material properties of the orthotropic CMP plate were adjusted to reflect the reduction in thickness of the actual (isotropic) plate. The corroded plate properties were computed using equations 3.2 to 3.9 for $t = t_0 P_t$, where t_0 is intact plate thickness.

3.3.7 Compaction Effects

During construction, the soil is placed on either side the pipe (and hence referred to as "sidefill") and compacted in successive layers, which are typically 150 mm to 300 mm-thick. The compaction process can result in high residual lateral soil pressures. These pressures effectively squeeze the pipe and can cause the crown to "peak" (i.e. deflect upwards). It is not entirely clear whether this peaking response during side filling has an influence on the resulting stress regime in the pipe. Therefore, one of the objectives of this model is to explore this question. If there is an influence, it would be desirable to account for it in the model.

Explicit modelling of the compaction process including densification of the soil would add enormous complexity to the model and is not essential to the problem considered in this study. Therefore, the objective here is simply to account for the *effects* of sidefill compaction in terms of the structural response of the CMP.

Recent efforts to incorporate compaction effects in culvert models (Elshimi & Moore, 2013) consisted of specifying a large value for the coefficient of lateral earth pressure, K, which was then used by the software to generate the post-compaction stresses in each layer. In Plaxis 3D, however, horizontal stresses are not computed using K, except during the initial calculation phase (for LE and MC soil models, the horizontal stresses generated from gravity loading are a function of Poisson's ratio). Therefore, the same approach could not be used here.

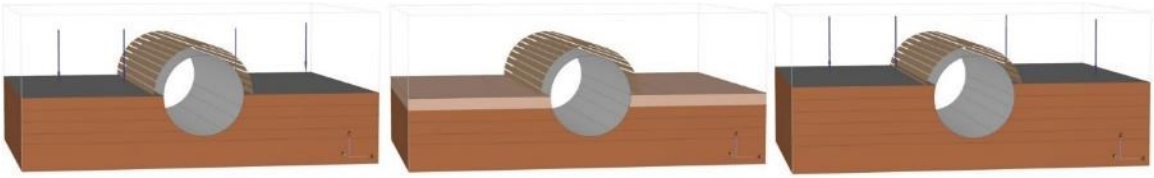

(1) (2) (3)

Figure 3.8 New procedure for simulating the effects of compaction next to a culvert pipe:(1) activate layer and apply load; (2) remove load; and (3) repeat for next layer.

An alternative procedure for incorporating the effects of compaction in the 3D model using the HS soil model is illustrated in Figure 3.8. Each compacted layer is applied in two (2) phases. The first phase consists of activating the new layer and applying an effective uniform vertical compaction load to the surface (the magnitude of which must be empirically-determined). In the second phase, the compaction load is removed. Due to hardening of the soil, residual lateral stresses should be developed, as in reality. It is anticipated that this technique would not produce the desired results when either the LE or MC soil models are used, since their material behaviour is largely (or entirely) elastic, and removing the compaction load would simply cause all incremental stresses and strains to be completely reversed.

Figure 3.9 shows the horizontal stress distributions produced from a simple numerical experiment employing the technique described above for three 0.3 m-thick layers of laterally confined soil and a vertical compaction load of 30 kPa. Separate tests were performed using the LE, MC, and HS soil models. Using the LE and MC models, the resulting horizontal stress distribution remains unchanged compared to before the compaction load was applied. Using the HS model, the resulting horizontal stress distribution is close to that expected (see Ingold (1979)).

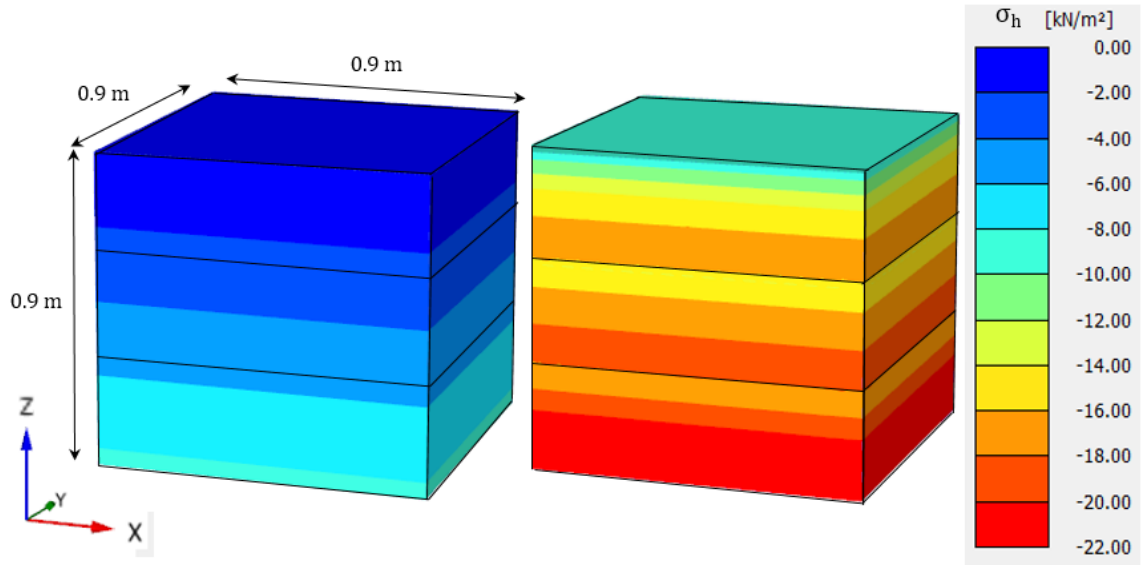

(a) (b)

Figure 3.9 Horizontal stress distributions resulting from a simple numerical experiment to assess compaction effects: (a) LE and MC models; and (b) HS model.

3.4 Results and Discussion

3.4.1 Dead Loading

The incremental changes in vertical and horizontal diameters during backfilling are plotted in Figure 3.10. As expected, both the LE and MC soil models were unable to accurately capture the peaking response of the pipe that was measured in the experiment. The LE model produced less than 1 mm of deflection in both vertically and horizontally. This is not surprising since any lateral strains that result from the application of the compaction load are completely recovered upon its removal. The MC model produced some noticeable peaking response, yet to a much smaller degree than was measured experimentally; a vertical expansion of 1.8 mm and horizontal contraction of 0.5 mm were computed upon completion of backfilling up to 0.9 m cover, versus experimental values of 4.2 mm and 6.1 mm, respectively. This can be attributed to the fact that some portion of the compaction-induced lateral strains are not recovered due to local yielding of the soil upon removal of the compaction load. The HS model captured the peaking response quite well. Vertical and horizontal deflections (5.0 mm and 4.3 mm, respectively) were within 19% and 30% of

experimental values (4.2 mm and 6.1 mm). These results indicate that the strain-hardening behaviour of the HS soil model was effective at transferring the compaction-induced lateral loads to the pipe.

3.4.1.1 Deflections

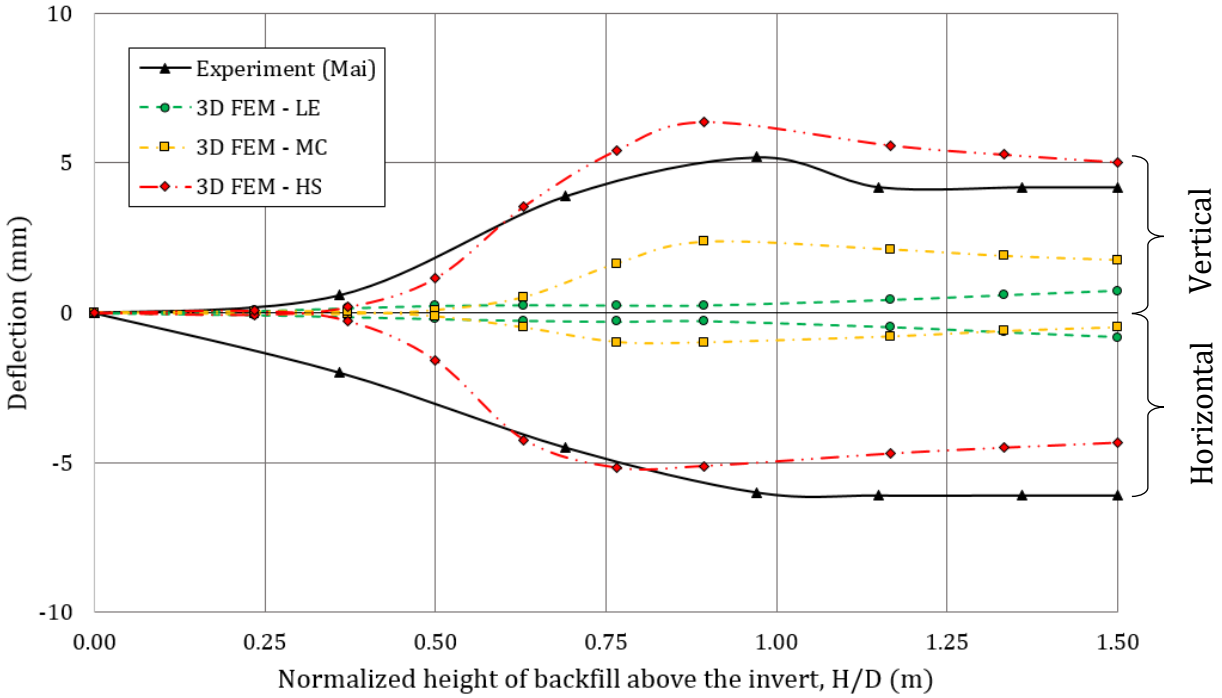

Figure 3.10 Vertical and Horizontal deflections during backfilling of CSP2 up to 0.9 m cover.

3.4.1.2 Thrusts

Figure 3.11 shows the total circumferential thrust distribution around CSP2 predicted by the model upon completion of backfilling up to 0.9 m cover. Experimental results are shown only near the crown (from shoulder to shoulder) because, as noted by Mai (2013) noted that there was unexpected tension measured in the bottom half of the pipe, which was likely erroneous. Results from the 3D FEM match relatively well with experimental results across the top half of the pipe for all soil models. However, the thrust at the crown is slightly underestimated using the LE model. This seems reasonable given that no yielding occurs in the LE soil, and thus the arching effect would be greater (and resulting thrust in the pipe smaller)

compared to the MC and HS models. The dead load thrust distribution around the pipe is relatively uniform for the MC and HS models. Maximum values are observed at the springlines (about 23 kN versus 19 kN at the crown for the HS model) for both the MC and HS models. In contrast, the location of maximum dead load thrust for the LE model was at the haunches (32 kN, compared to 12kN at the crown and 24 kPa at the invert).

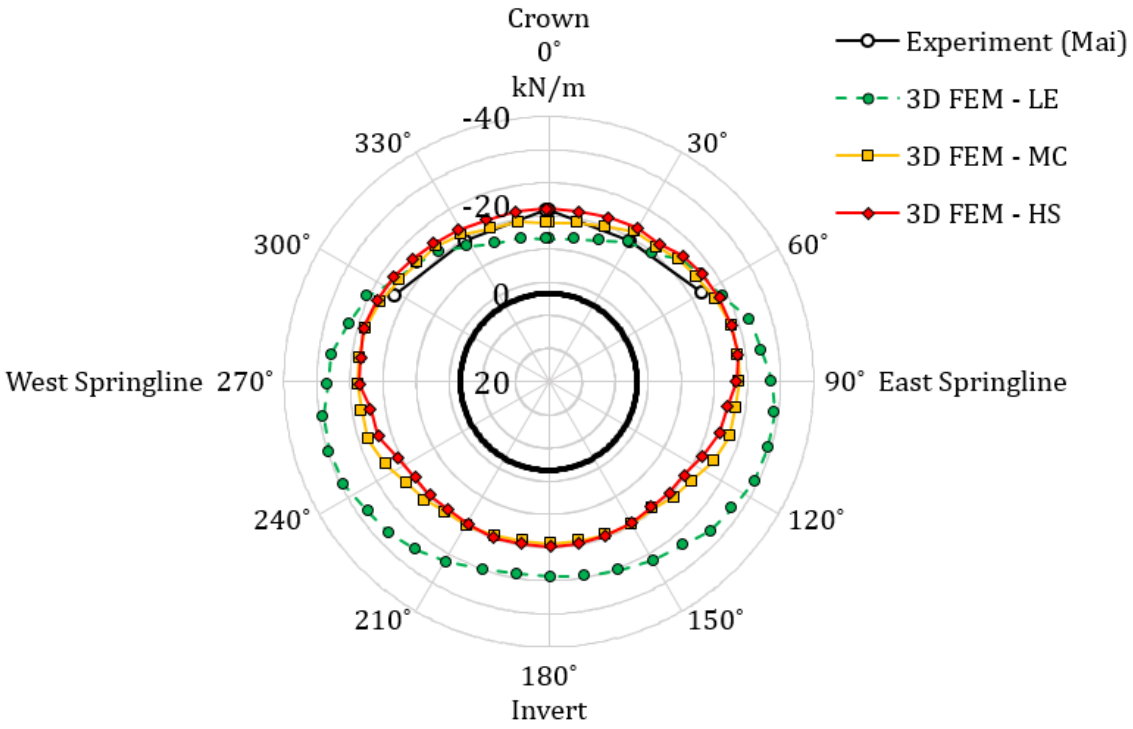

Figure 3.11 Circumferential thrust distributions around CSP2 upon completion of backfilling with 0.9 m cover.

3.4.2 Live Loading

3.4.2.1 Deflections

Figure 3.12 shows the model results for vertical and horizontal deflections during live loading with the SA load and 0.6 m cover. It is evident that the non-linear relationship between deflection and applied load was not captured by the 3D FE models using linear elastic soils. The 2D FE model by Mai et al. (2014b), which also utilized a linear-elastic soil model, was similarly unsuccessful in capturing this trend. However, the

trend was captured reasonably well by the 3D FE model using either the MC or HS soil models.

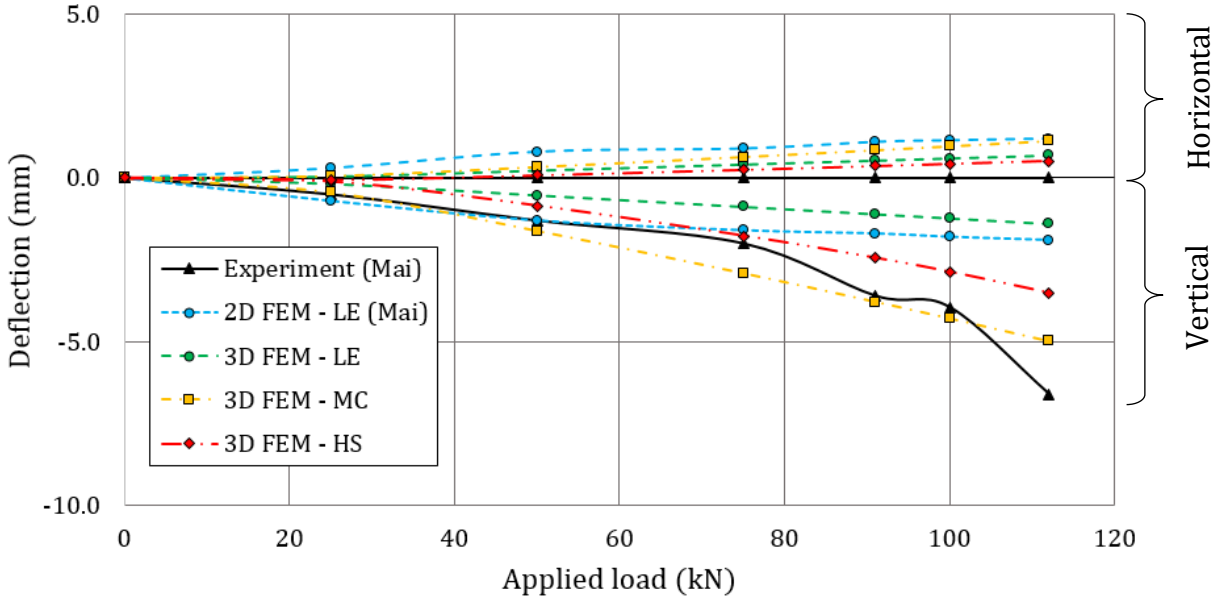

Figure 3.12 Vertical and horizontal deflections in CSP2 during single axle (SA) loading with 0.6 m cover.

3.4.2.2 Thrusts

The incremental circumferential thrust distribution around the pipe due to a single axle load of 87.5 kN with 0.9 m cover is shown in Figure 3.13. The magnitude of thrust at the crown for the LE model was only about 36% of the experimental value. Live-load thrust distributions from the MC and HS models were very similar (i.e. within 1% of each other), both of which matched the measured values very closely except at the crown. The experimental thrust distribution indicates a reduction of approximately 13 kN from the shoulder to the crown, while the 3D FEM results remain relatively constant between the shoulders, with maximum values occurring at or near the crown. Notably, only one experimental data point exists between the shoulders. Therefore, any error potentially associated with that data point would have a significant influence on the interpreted thrust distribution across the top of the pipe. Further supporting this possibility is the fact that a similar reduction of thrust at the crown was not observed in any of the other experimental load cases.

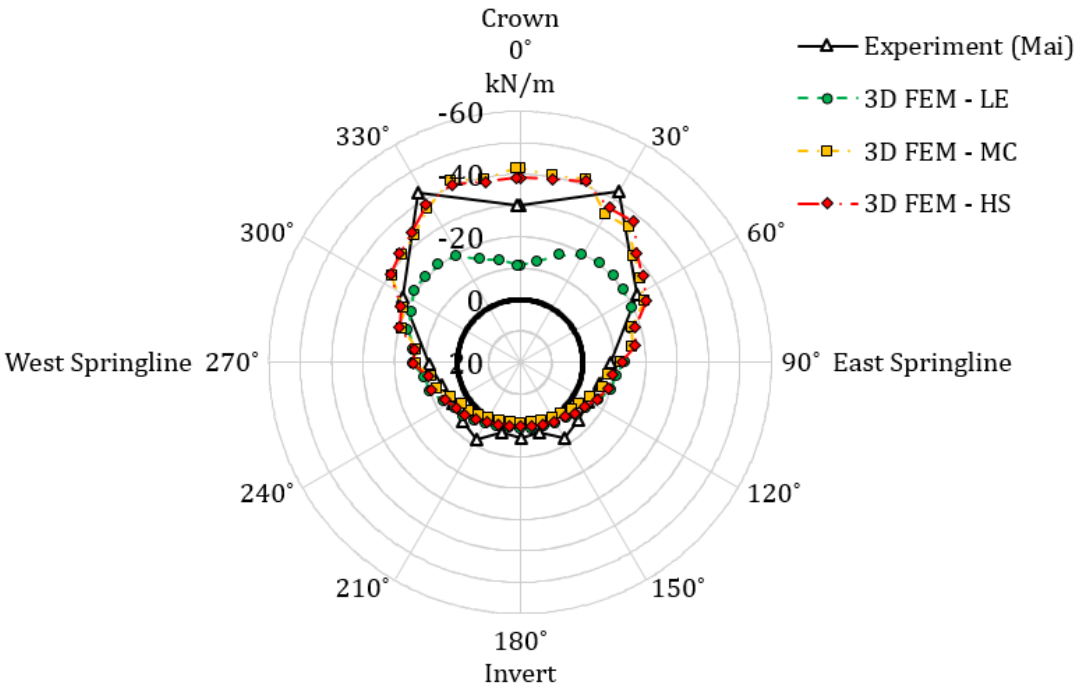

Figure 3.13 Incremental thrust distribution around CSP2 due to 87.5 kN single axle (SA) load with 0.9 m cover.

The maximum thrust force in CSP2 during SA loading with 0.9 m and 0.6 m cover is plotted in Figure 3.14 and Figure 3.15, respectively. Both cover depths show similar trends; only the magnitudes of thrust are higher for the case with 0.6 m cover. The thrust forces predicted by the 3D FE model with the LE soil were significantly less than measured values (39 kN versus 114 kN at an applied load of 100 kN). Furthermore, the LE model produced a linear load-thrust trend, in contrast to the non-linear response measured experimentally. Although the 2D model by Mai also failed to capture the non-linear behaviour of the culvert, it did provide a much more accurate prediction of live-load thrust than the 3D model. The most likely explanation for this is that the 2D model relied on the use of a load-spreading factor for determining an "equivalent" line load to apply at the ground surface. This factor was developed to produce (generally) conservative values of thrust for typical loading conditions. Conversely, load spreading in the 3D model is accounted for explicitly. Since the LE soil model has infinite strength, the load spreading is maximized and a smaller portion of the applied load is transferred to the pipe. Live-load thrusts from

the 3D FEM using the MC and HS models are nearly identical (106 kN and 110 kN, respectively, for an applied force of 100 kN). Both models agree closely with the experimental results in terms of both magnitude and the non-linear trend. However, the experimental curve diverge from the 3D FEM results at the very end of the curve. This could be due to the small amount of cohesion (5 kPa) that was necessarily assigned to the MC and HS models to provide numerical stability. This amount of cohesion may be sufficent to prevent some of the local yielding within the soil, thereby reducing the portion of the applied load that is transferred to the pipe.

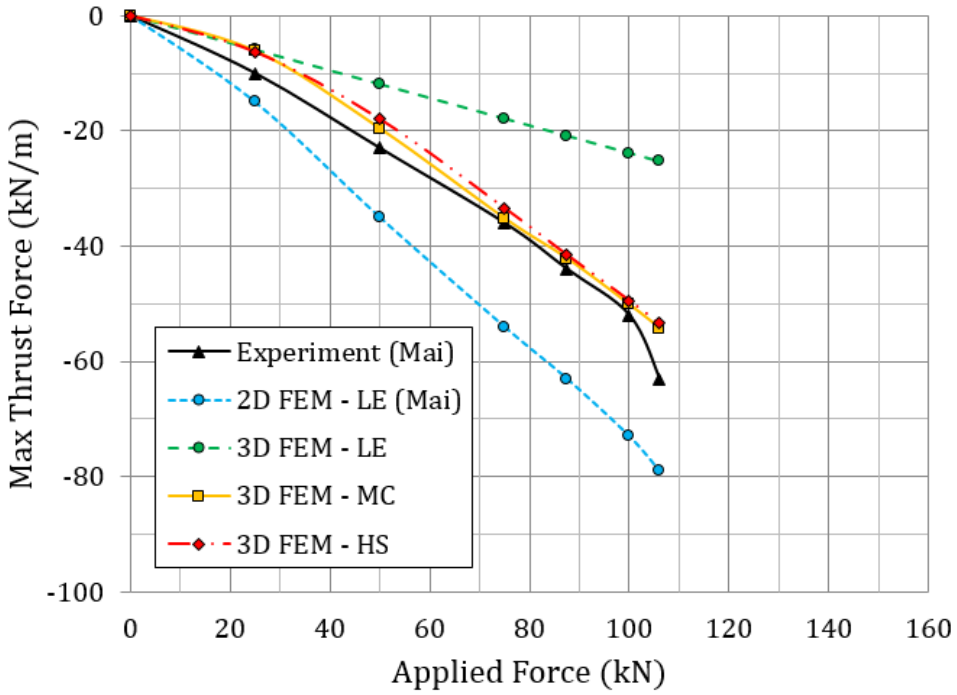

Figure 3.14 Maximum incremental thrust in CSP2 during single axle (SA) loading with 0.9 m cover.

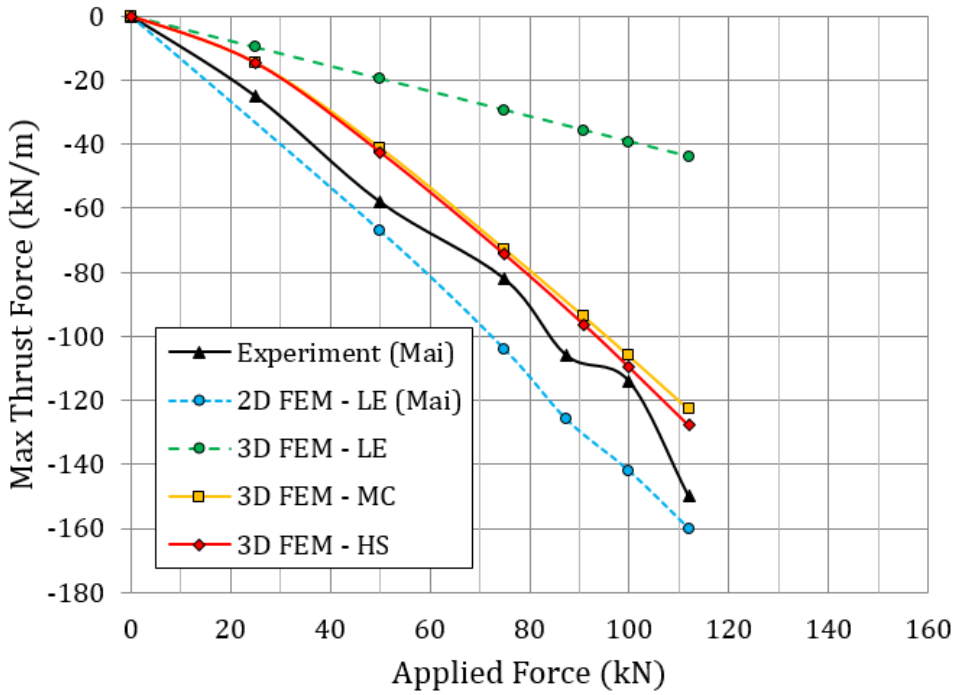

Figure 3.15 Maximum incremental thrust in CSP2 during single axle (SA) loading with 0.6 m cover.

3.4.2.3 Bending Moments

The incremental circumferential bending moment distribution due to a single axle load of 87.5 kN is shown in Figure 3.16. The magnitudes of the bending moments are small (i.e. < ±0.5 kN·m/m), owing to the relative flexibility of the pipe considered. Regardless, the distribution of live load bending moments around the CMP was well captured using the HS model, and to a lesser degree using the MC model. The live load bending moments were underestimated when the LE model was used.

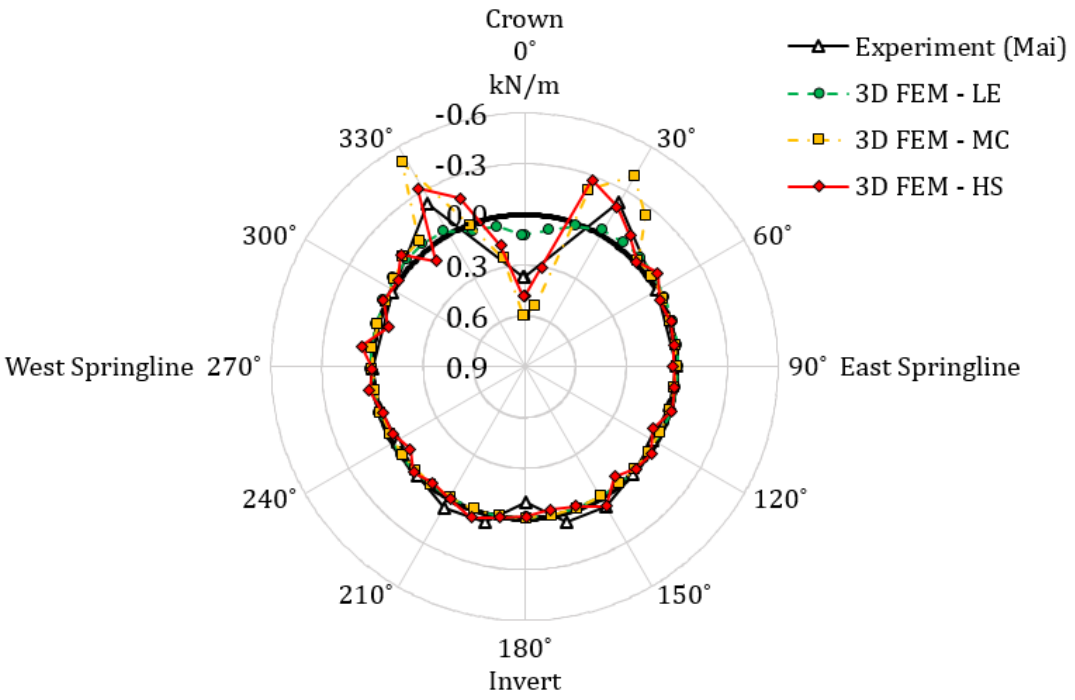

Figure 3.16 Maximum incremental bending moment distribution around CSP2 due to 87.5 kN single axle (SA) load with 0.9 m cover.

The maximum live load bending moment in the pipe during SA loading with 0.6 m cover is shown in Figure 3.17. The general trend (i.e. non-linear) observed in the experiment was clearly captured by the MC and HS models, while the results produced by the LE model were linear and less accurate.

Overall, the model predicted the structural response of the culvert observed in the experimental tests with reasonable accuracy, especially using the HS soil model.

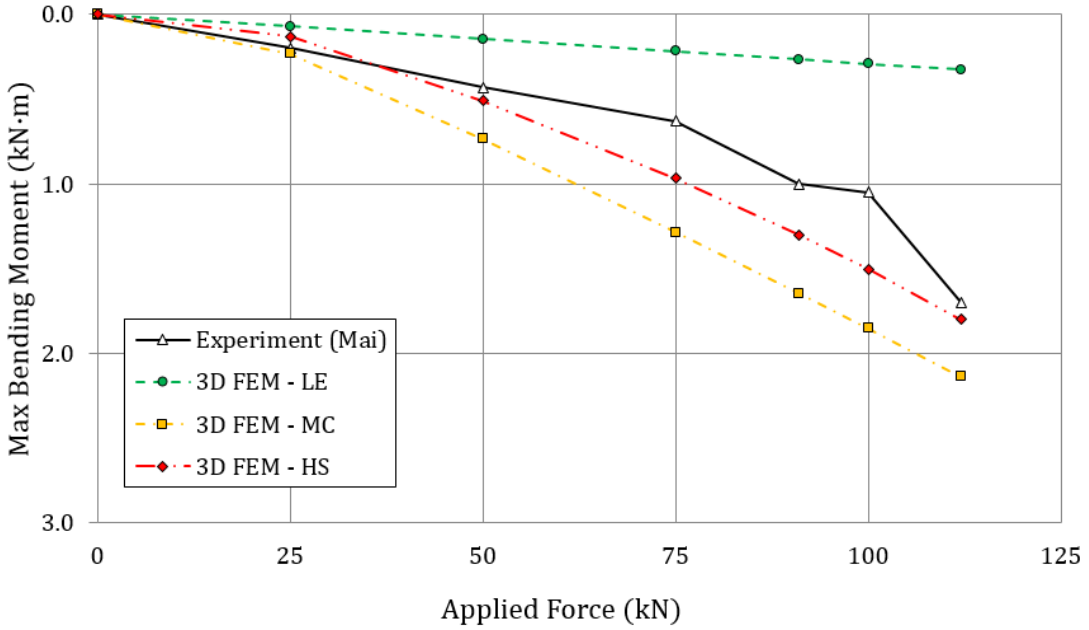

Figure 3.17 Maximum incremental bending moment in CSP2 during single axle (SA) loading with 0.6 m cover.

3.5 Conclusions

The following conclusions are made:

1. The HS soil model accurately captured the experimental peaking response of the culvert during backfilling. the MC model was less accurate, and the LE model was inaccurate. The HE soil model was therefore effective at transferring the simulated compaction-induced loads from the soil to the pipe.
2. The LE soil model did not predict the dead load thrusts as well as the MC and HS models.
3. Live-load thrust distributions from the MC and HS models were within 1% of each other, and both matched the experimental data closely everywhere except at the crown.
4. The non-linear load-bending moment curve observed in the experiment was well captured by the MC and HS models; the results produced by the LE model were linear and inaccurate.

5. The observed performance of the developed 3D finite element model is deemed sufficient for proceeding with a parametric study in the following chapters.

CHAPTER 4:
PARAMETRIC STUDY FOR INTACT CORRUGATED METAL PIPE CULVERTS

4.1 Introduction

This Chapter presents results from a parametric study for round (i.e. circular cross-section), intact CMP culverts. The parametric study was based on three-dimensional finite element analyses, which were carried out using the software package Plaxis 3D.

The purpose of the study was to determine the most important geometric and material parameters governing the behaviour of the culvert pipe. Specifically, five (5) parameters were varied: diameter of the pipe, height of cover soil, secant modulus of backfill soil, internal friction angle of backfill soil, and the strength reduction factor of the soil-pipe interface. Each parameter is examined in terms of its effects on thrusts and bending moments in an intact (i.e. non-corroded) culvert pipe during live loading.

4.2 Numerical Details

4.2.1 Geometry, Mesh and Boundary Conditions

The three-dimensional geometry of the models used in this study is presented schematically in Figure 4.1 and Figure 4.2. In general, the models contain the same features described in Chapter 3. One notable difference is the addition of a pavement surface. The pavement surface (which is present in most culverts) constitutes a relatively stiff layer at the ground surface and thus has a major influence on the amount of live load that gets transferred to the pipe. Furthermore, the inclusion of the pavement surface helps to prevent numerical instability associated with local bearing failures of the soil at the locations where live loads are applied.

The extent of the overall model boundaries varied as a function of the pipe diameter, D. In the longitudinal (or "y") direction, the model length was set at $8D$. The transverse (or "x") direction boundary dimension was also set at $8D$, leaving $3.5D$ between the

outermost edges of the pipe and the nearest model boundaries. In the vertical (or "z"), direction, the bottom model boundary was set at 3.5D below the invert of the pipe. Results of sensitivity analyses indicated that further extension of the overall model boundaries had negligible effects on the output from the area of interest (i.e. near the centre of the model).

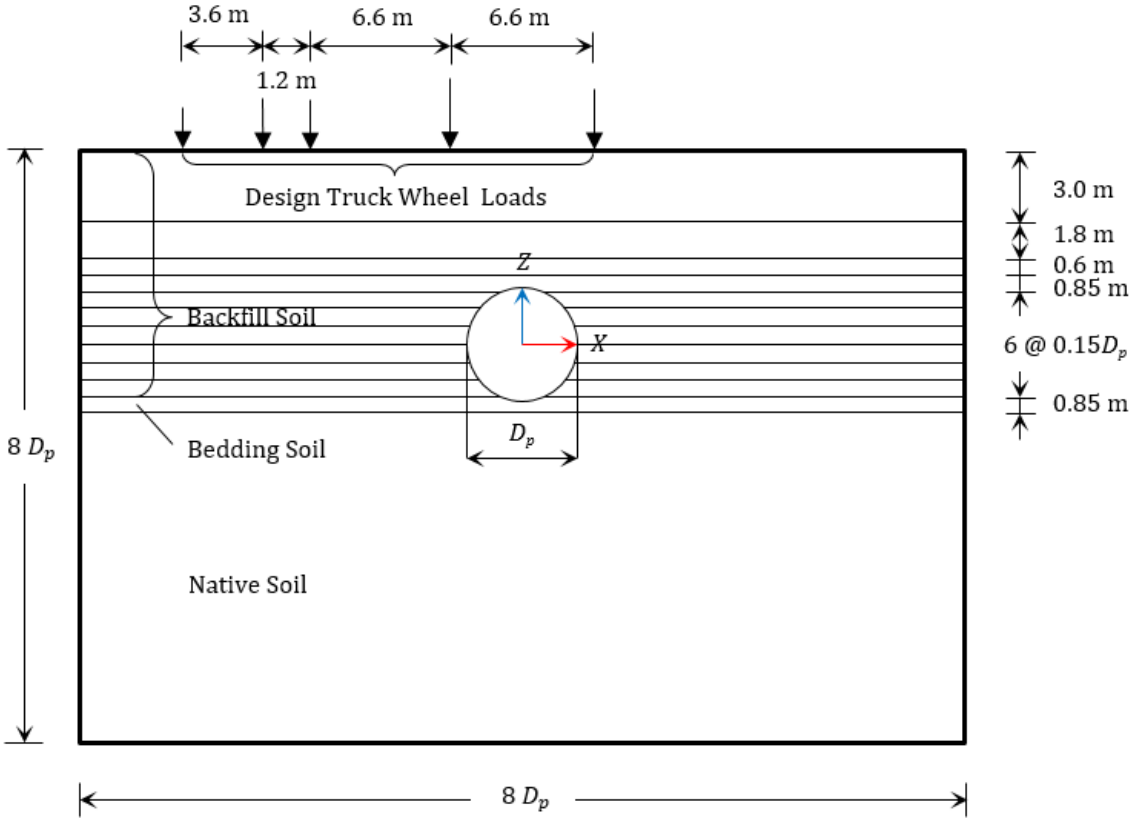

Figure 4.1 Vertical cross-section schematic of 3D model geometry.

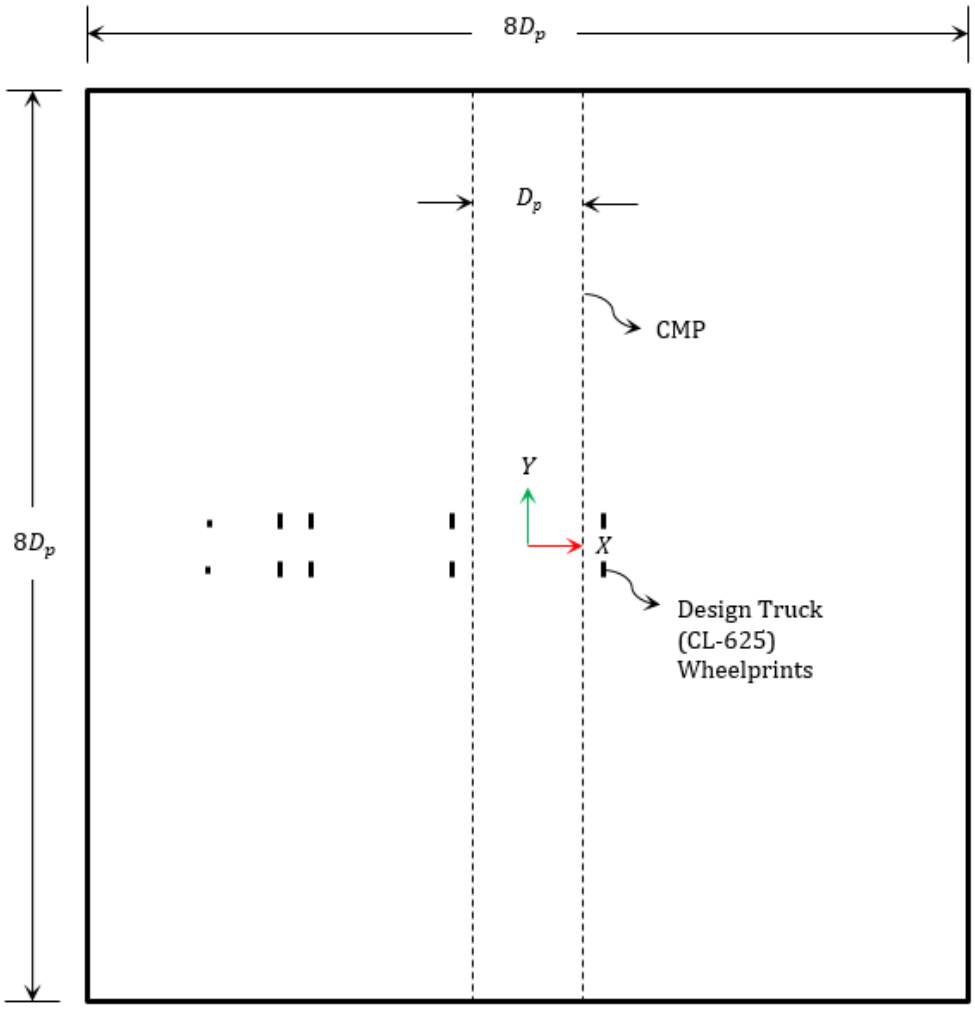

Figure 4.2 Plan view schematic of 3D finite element model geometry.

Each model consists of three different soil materials: Native Soil, Bedding Soil, and Backfill Soil. A 0.6 m-thick layer of Bedding Soil was placed directly underneath the pipe. To avoid poor-quality elements resulting from sharp angles in the geometry, the top surface of the Bedding Soil was placed slightly ($0.05D$) above the invert of the pipe. Similarly, the bottom surface of the 7th layer of Backfill Soil was set slightly below the crown. The Backfill Soil between the invert and crown of the pipe was divided into 6 layers of equal thickness, or $0.15D$. Four (4) more layers of Backfill Soil were defined, whose top surfaces correspond to cover heights of 0.6 m, 1.2 m, 3.0 m, and 6.0 m above the top of the CMP. Wheelprints for the application of live loads were created at each of the four cover heights based on the CL-625 design truck, positioned

such that the centreline of the rear two axles was in line with the centreline of the pipe (and the origin of the model). An interface feature was created around the entire circumference of the pipe, where it contacts the surrounding soil.

A cut section through a typical 3D model displaying element contours is shown in Figure 4.3. A finite element mesh—consisting of the same types of elements described in Section 3.3.2—was automatically generated by the Plaxis software. A relative element size factor r_e = 1.0 ("medium") was assigned to most model features, while r_e = 0.3 ("very fine") was assigned to the wheelprints and the innermost one half (longitudinally) of the CMP. The pavement surface was modelled using the same type of 2D triangular plate elements used for the pipe. Model boundary conditions were the same as described in Section 3.3.2.

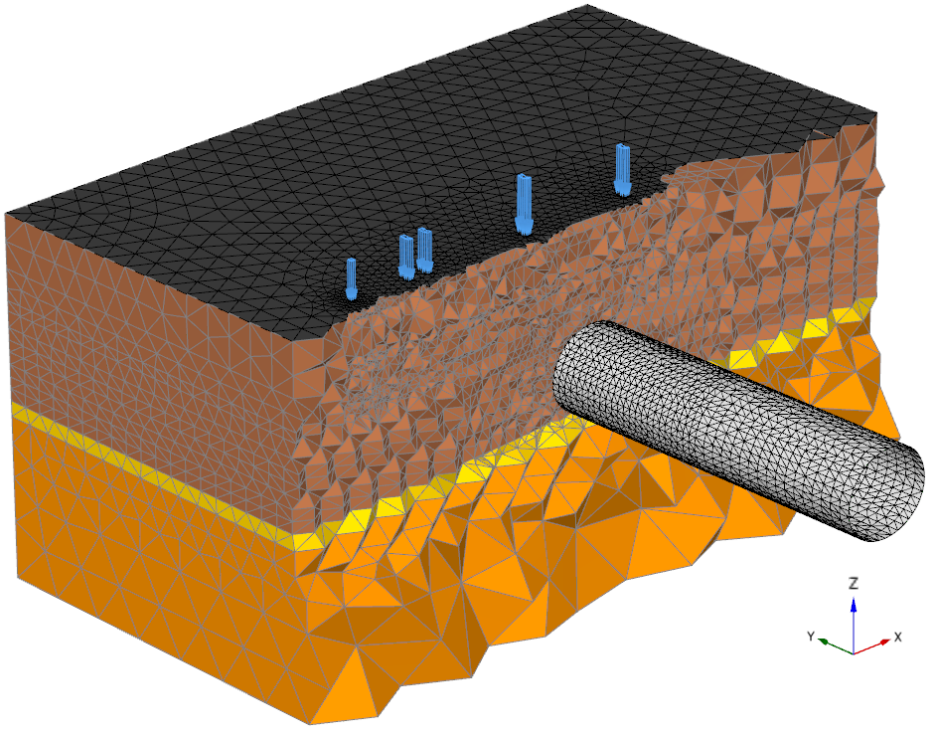

Figure 4.3 Cutaway section of the three-dimensional finite element mesh used in the parametric study (D = 5.0 m, H_c = 6.0 m).

4.2.2 Material Properties

The corrugated metal pipe was modelled using orthotropic plates, and the same approach described in Section 3.3.3. Input parameters of the CMP plate are given in

Table 4.1 All analyses are based on pipes made from conventional corrugated plates, i.e. with corrugation profiles of 152 mm x 51 mm (pitch x depth). An intact pipe plate thickness of 5.0 mm was used for all analyses. The influence of pipe flexibility on the model results was investigated by varying the diameter of the pipe, while the corrugation profile and plate thickness were held constant for all analyses.

Table 4.1 Input parameters of the orthotropic plate used to model the CMP.

Parameter		Symbol	Value	Units
Plate thickness		$\bar{t} = d$	60.36	mm
Unit weight		$\bar{\gamma} = \gamma$	7.84	kN/m^3
Elastic moduli	Circumferential	$\bar{E}_\theta = E_2$	20,373,235	kPa
	Longitudinal	$\bar{E}_L = E_1$	113,662	kPa
Poisson's ratio		$\bar{\nu} = \nu_{12}$	0	-
Shear moduli	Circumferential Out-of-plane	$\bar{G}_{\theta R} = G_{23}$	7,835,860	kPa
	Longitudinal Out-of-plane	$\bar{G}_{LR} = G_{13}$	43,716	kPa
	In-plane	$\bar{G}_{L\theta} = G_{12}$	585,282	kPa

Three different soil materials were included in the model: 'Native Soil', 'Bedding Soil', and 'Backfill Soil'. The Native Soil was modelled using the MC soil model (to reduce computational effort of the model), while the Bedding Soil and Backfill Soil were modelled using the HS soil model. The soil parameters used in this study are given in Table 4.2. Some of the material parameters (friction angle, secant modulus, and interface strength reduction factor) were varied as part of the parametric study, while the other soil parameters were held constant. The oedometer modulus E_{oed}^{ref} and unload-reload modulus E_{ur}^{ref} of the Backfill Soil were varied in proportion to the secant modulus E_{50}^{ref}, maintaining a constant relationship between the three stiffness moduli (E_{oed}^{ref} =0.8 E_{50}^{ref}, and E_{ur}^{ref} = 3.0E_{50}^{ref}). The specified stiffness values for the HS model are based on a reference pressure of 100 kPa.

Table 4.2 Soil properties used for the parametric study.

Parameter	Symbol	Values			Units
		Native Soil	Bedding Soil	Backfill Soil	
Soil model	-	MC	HS	HS	-
Unit weight	γ_s	20.0	18.0	20	kN/m^3
Cohesion	c'_{ref}	5	5	5	kPa
Internal friction angle	φ'	36	32	Varies	°
Young's modulus	E'	60	-	-	MPa
Poisson's ratio	ν'	0.3	-	-	-
Secant modulus	E_{50}^{ref}	-	40	Varies	MPa
Oedometer modulus	E_{oed}^{ref}	-	30	$0.8E_{50}^{ref}$	MPa
Unload-reload modulus	E_{ur}^{ref}	-	120	$3.0E_{50}^{ref}$	MPa
Interface strength reduction factor	R_{inter}	0.6	0.6	Varies	-

4.2.3 Modelling Sequence and Loading

The model was carried out using a staged construction approach, as in Chapter 3. In the initial phase, the native soil, bedding soil, CMP, and soil-pipe interface were all activated. All displacements were reset to zero at the end of this phase. Conversely, soil stresses and pipe forces were not reset; the initial stress regime was developed during this stage based on gravity loading.

The backfill soil layers were activated in successive steps up to the various specified cover heights. Symmetry is preserved during this process, i.e. it is assumed that the backfill on either side of the pipe is placed at the same rate and there is no differential loading.

Once the desired cover height is reached, a (weightless) pavement surface and the live loads are activated. Live loading is based on the CL-625 tandem axle design truck

(CSA, 2014). Axle and wheel loads for the CL-625 truck are shown in Figure 4.4. The wheel loads indicated were uniformly distributed over the area of each wheelprint.

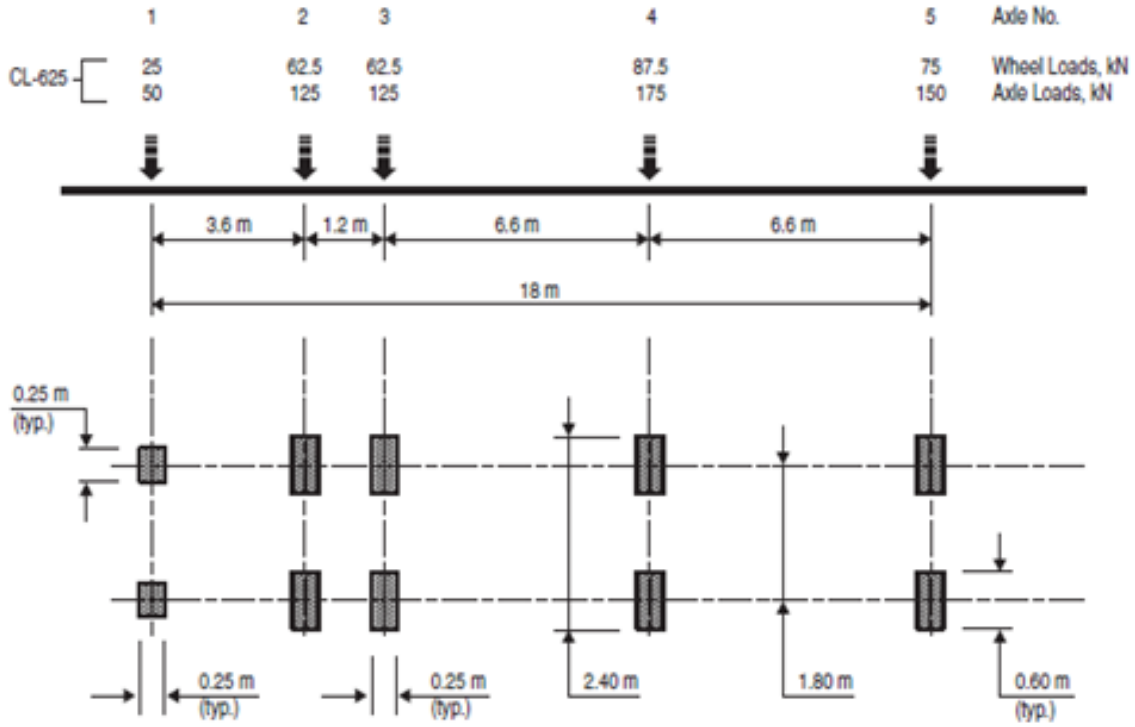

Figure 4.4 CL-625 design truck wheel and axle loads (CSA, 2014)

4.2.4 Study Parameters

The following five (5) parameters were varied to evaluate their influence on the structural forces (thrust and bending moment) in the pipe during live loading:

- Diameter of Pipe, D
- Height of Soil Cover, H_c
- Secant Modulus of Soil, E_{50}^{ref}
- Internal Friction Angle of Soil, φ'
- Strength Reduction Factor for Soil-Pipe Interface, R_{inter}

The baseline, minimum, and maximum values for each of the study parameters are given in Table 4.3. Twenty (20) simulations in total were carried out as part of the study. Four (4) different heights of soil cover were considered: 0.6 m, 1.2 m, 3.0 m, and 6.0 m. For each of the remaining parameters, five (5) different values were used.

Pipe diameters of 2.0 m, 3.5 m, 5.0 m, 6.5 m, and 8.0 m were used. The secant modulus of the backfill soil was varied between 15, 30, 60, 90, and 120 MPa. The friction angle of the backfill soil was varied between 32, 34, 36, 38, and 40°. Strength reduction factors of 0.2, 0.4, 0.6, 0.8, and 1.0 were considered for the soil-pipe interface.

Table 4.3 Baseline, minimum, and maximum values used for parametric study of intact culverts.

Parameter	Symbol	Values			Units
		Min	Baseline	Max	
Diameter of Pipe	D	2.0	5.0	8.0	m
Height of Soil Cover	H_c	0.6	1.2	6.0	m
Secant Modulus of Soil	E_{50}^{ref}	15	60	120	MPa
Internal Friction Angle of Soil	φ'	32	36	40	°
Strength Reduction Factor for Soil-Pipe Interface	R_{inter}	0.2	0.6	1.0	N/A

The parametric study consisted of running a series of 3D FEM simulations. In each simulation, a single input variable was changed from its baseline value, while all other variables were kept constant. Interaction effects that may occur when varying multiple parameters in the same simulation were not explored in the current study. One notable exception is the three (3) stiffness parameters (E_{50}^{ref}, E_{oed}^{ref}, and E_{ur}^{ref}) of the backfill soil, which were varied in proportion to one another as explained in Section 4.2.2.

Two main output variables were considered: maximum thrust and maximum bending moment in the pipe. Further distinction is made between dead load forces (i.e. thrusts/bending moments resulting from the self-weight of the pipe and surrounding soil), live load forces (i.e. incremental thrusts/bending moments due to live loads only), and total forces (i.e. thrusts/ bending moments due to combination of dead and live loads). It is important to note that when discussing maximum forces (Sections 4.3.2 to 4.3.7), the maximum total force in the CMP is not simply a summation of the

maximum dead load force and the maximum live load force. The reason for this is that the maximum dead load force and the maximum live load force occur at different locations on the pipe circumference.

4.3 Results and Discussion

Unless otherwise noted, results discussed in this section pertain to the cross-section of the CMP in the centre of the model, i.e. directly below the centreline of the design truck, as shown in Figure 4.2.

4.3.1 Baseline Case

The following sections describe the output from the model for the baseline case, the input parameters for which are given in Table 4.3.

4.3.1.1 Forces

The total circumferential thrust in the culvert at various stages is shown in Figure 4.5. When the backfill just reaches the crown, the thrust distribution is highly non-uniform, with very little thrust at the crown and the maximum thrust at the invert. After placement of 1.2 m of cover, the thrust is substantially increased and its distribution becomes more uniform. Still, the thrust at the springlines is about 67% and 50% greater than the thrust at the crown and invert, respectively. The maximum thrust is located just below the springlines. The thrust at the crown is increased by about 33% when the live load is applied. This increase in thrust was not uniform around the pipe; the thrust at the invert remained practically unchanged.

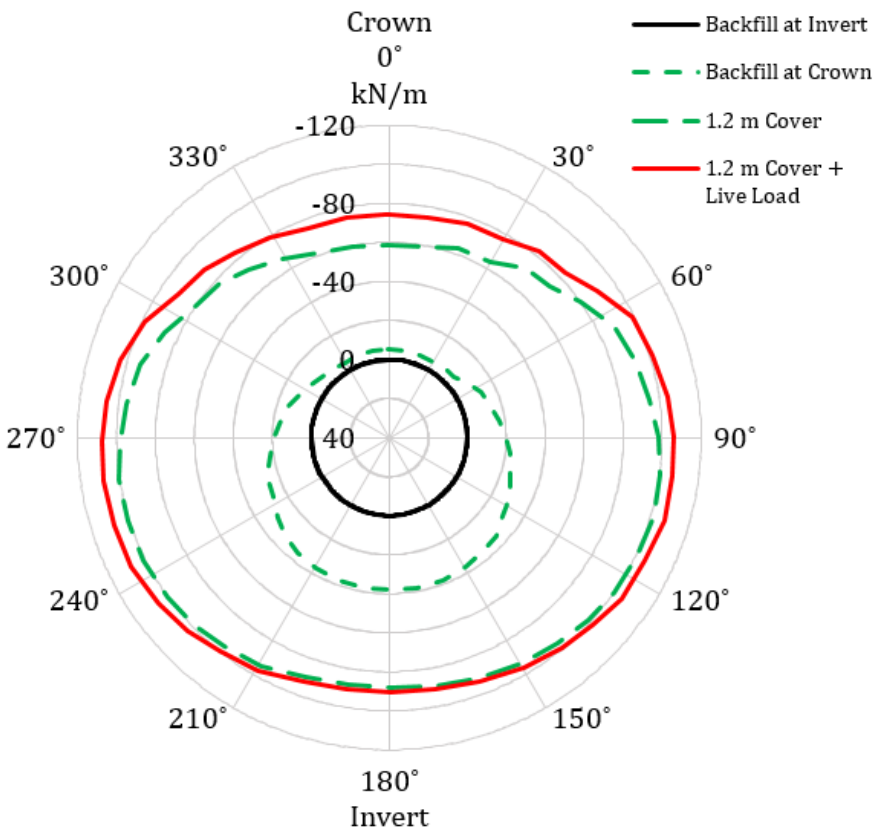

Figure 4.5 Total circumferential thrust around the pipe at various stages.

Figure 4.6 shows the total circumferential bending moment in the culvert at various stages. Under 1.2 m of cover, the largest bending moments in the pipe are just below the springlines and just inside the haunches. While the magnitude of the bending moments may seem small (the maximum total bending moment at this stage is only 2.8 kN·m/m), these forces convert to significant bending stresses in the pipe, owing to the very low moment of inertia of the corrugated plate. The total calculated stresses from bending under 1.2 m of cover are of the same order of magnitude as the stresses from axial compression (thrust). At the locations of the maximum bending moment, the maximum bending stress is higher than the axial stress.

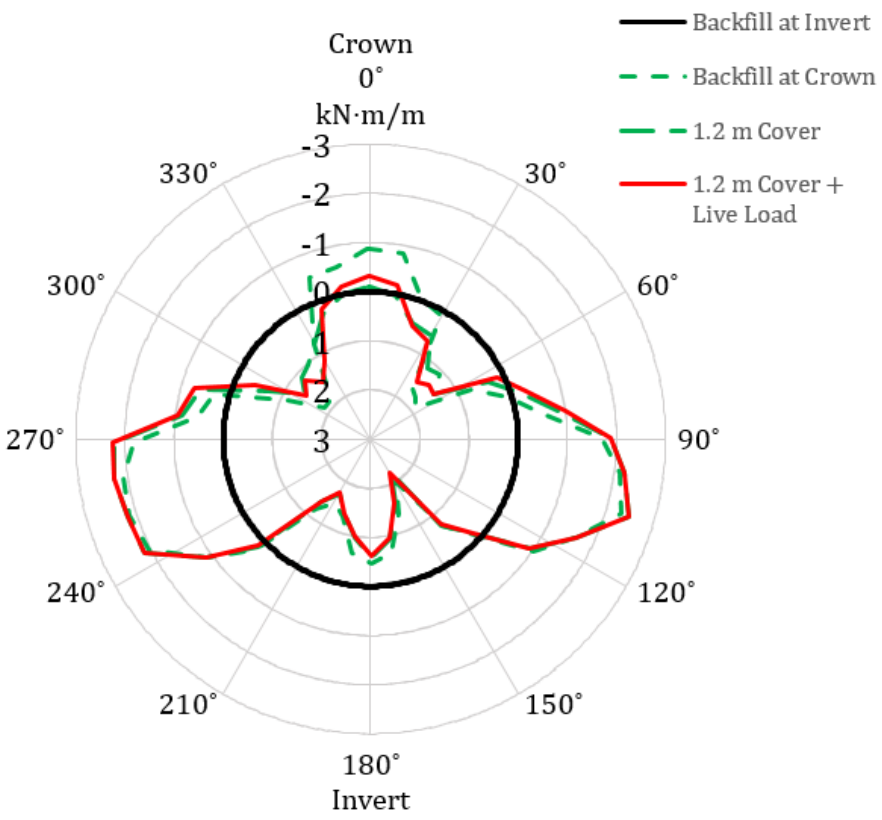

Figure 4.6 Total bending moment distribution around CMP with 1.2 m cover.

4.3.2 Effect of Pipe Diameter

The diameter of the pipe had the second largest influence of any of the study parameters on the maximum total thrust (next to height of soil cover), and the largest influence on the maximum total bending moment.

The relationship between pipe diameter and maximum thrust (dead, live, and total) is slightly non-linear, as shown in Figure 4.7. Again, it is important to note that the maximum total thrust is not a summation of the maximum dead and live load thrusts, since these occur at different locations around the pipe circumference. With respect to the dead load thrust curve, the non-linearity may be due to the volume of soil directly above the shoulders of the pipe. The volume—and thus weight—of the soil in this zone varies with the square of the pipe diameter, whereas the remaining volume of soil in the rectangular column directly above the pipe is linearly proportional to the pipe diameter. With respect to the live load thrust curve, the non-linearity may be

explained by the geometry of the live load wheelprints. In the baseline case where D = 5.0 m, each of the rear two axles of the design truck are completely outside of the pipe outline (the distance between the two rear axles is 6.6 m). When D = 2.0 m, the rear axles are even further away from the edges of the pipe. Therefore, it is perfectly sensible that a smaller portion of the live load would reach the pipe in this case. Conversely, a larger portion of the live load reaches the pipe for larger pipe diameters. When D = 8.0 m, the rear two axles are both completely inside the outline of the pipe.

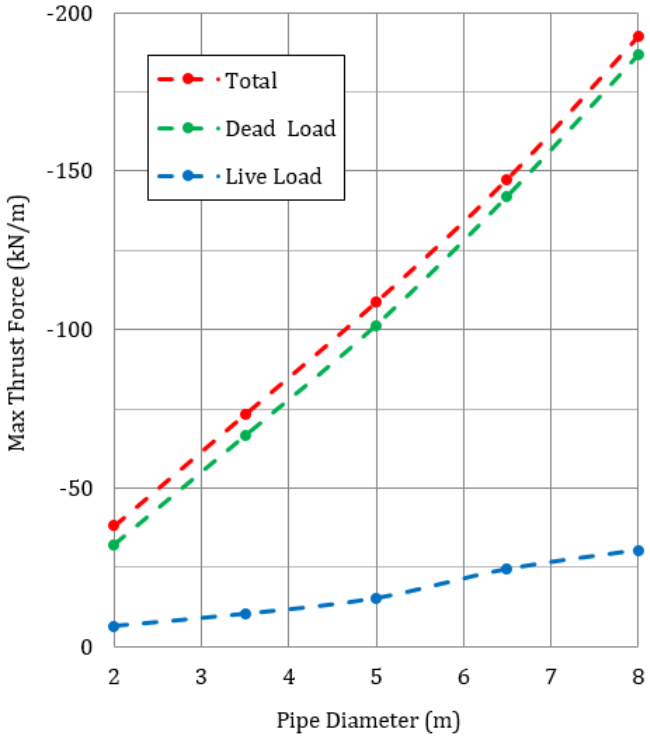

Figure 4.7 Effect of pipe diameter on maximum thrust.

The relationship between pipe diameter and maximum bending moment is shown in Figure 4.8 and is clearly non-linear. With respect to the dead load bending moment curve, the non-linearity may be explained by the fact that the lateral earth load varies in proportion to the square of the height (diameter) of the pipe (i.e. area of simplified pressure triangle = $K\gamma_s D(D/2) = K\gamma_s D^2$. Since the moment arm is directly proportional to the pipe diameter, the resulting moment ($K\gamma_s D^2(D) = K\gamma_s D^3$) would be proportional

to the cube of the pipe diameter. This logic agrees with the trend of the dead load moment curve shown in the Figure 4.8.

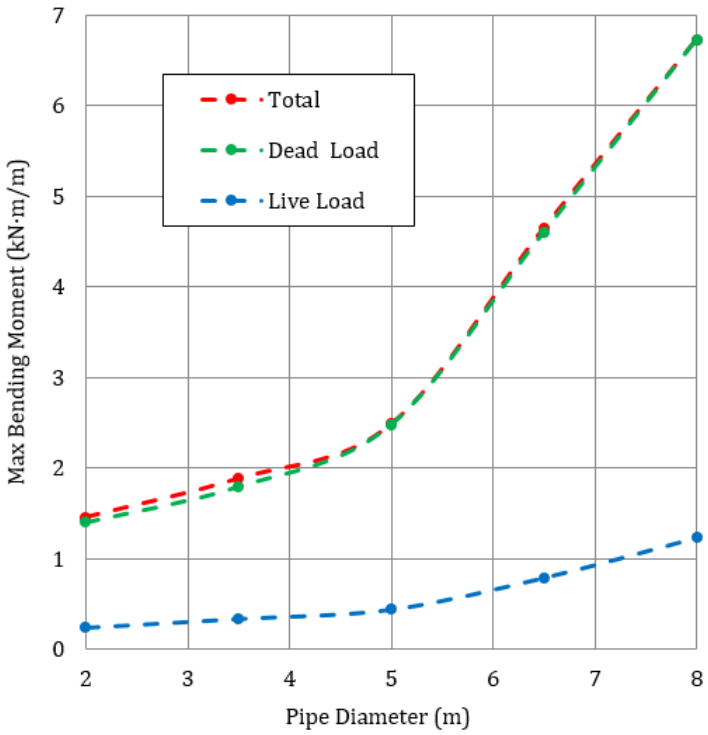

Figure 4.8 Effect of pipe diameter on the maximum bending moment.

4.3.3 Effect of Height of Soil Cover

The height of soil cover had the largest influence on the maximum total thrust. As expected, the maximum dead load and live load thrust are both linearly proportional to the height of soil cover, as shown in Figure 4.9. The dead load thrust increases with increasing cover height due to the additional volume of soil above the pipe. The live load thrust decreases with increasing cover height as the load is able to spread out further and a greater portion of the total live load is transferred away from the pipe.

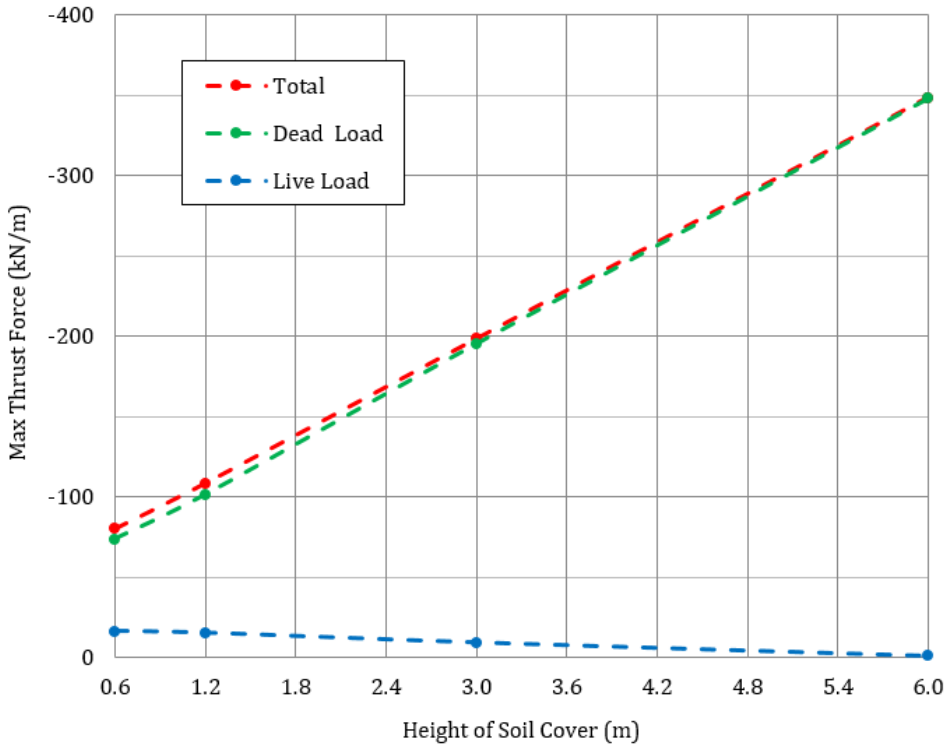

Figure 4.9 Effect of height of soil cover on maximum thrust.

The height of soil cover had a moderate influence on the maximum total bending moment (Figure 4.20). The relationship between maximum dead load moment and height of soil cover is only very slightly non-linear, as shown in Figure 4.10. As expected, maximum dead load moment increases with increasing cover height. The maximum live load moment decreases with increasing cover, and is highly non-linearity for cover heights less than about 2m. A possible explanation for this is that the maximum live load moment occurs at the shoulders, which is relatively close to the truck wheelprints in the baseline case. Under shallow cover heights, a large portion of the live load is probably transferred to the shoulders. As the cover height increases, the live load spreads and is transferred to the pipe in a more distributed fashion.

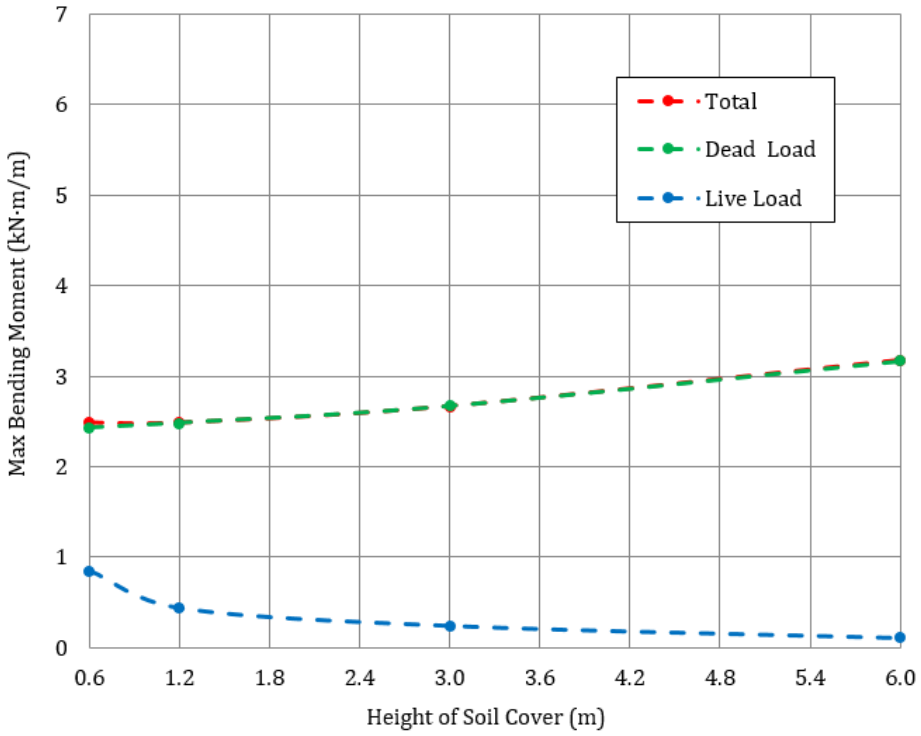

Figure 4.10 Effect of height of soil cover on the maximum bending moment.

4.3.4 Effect of Secant Modulus of Soil

The secant modulus appears to have only a very minor effect on the maximum thrust in the pipe (Figure 4.17), and a slightly more significant effect on the maximum bending moment (Figure 4.20).

Both the maximum dead load thrust and maximum bending moments increased with decreasing stiffness of the backfill soil (Figure 4.11 and Figure 4.12, respectively). A plausible explanation for this could be that less positive arching occurs when the stiffness of the sidefill soil is reduced.

Figure 4.12 shows that the maximum bending moment is comparatively more sensitive to the secant modulus than is the maximum thrust. This is probably because looser sidefill soil cannot provide as much lateral support to the pipe, which forces a greater portion of the applied load to be supported through bending versus axial compression (i.e. thrust). This effect is non-linear; it appears to be most pronounced for loose backfill soils (i.e. when $E_{50}^{ref} \leq 30$ MPa).

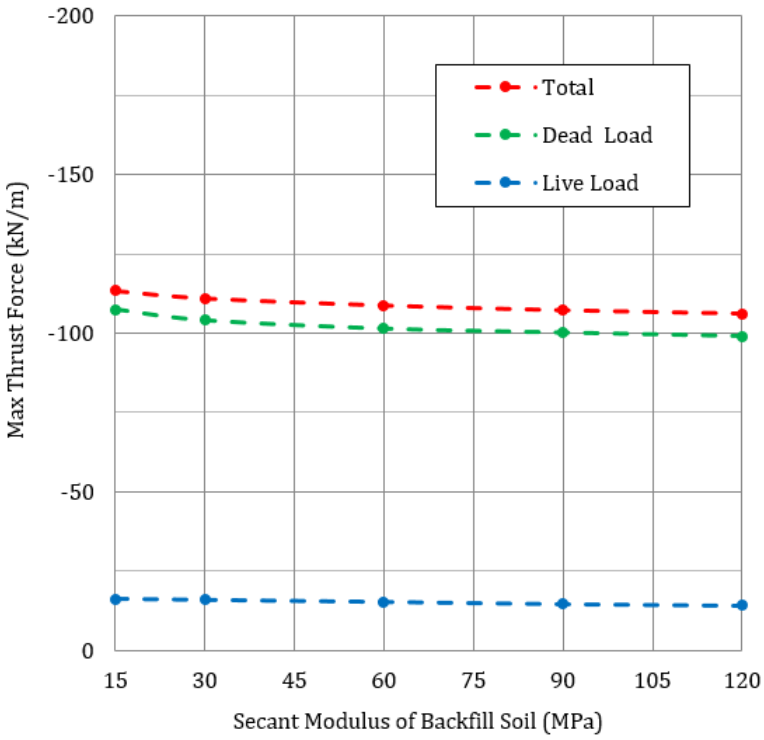

Figure 4.11 Effect of secant modulus of backfill soil on maximum thrust.

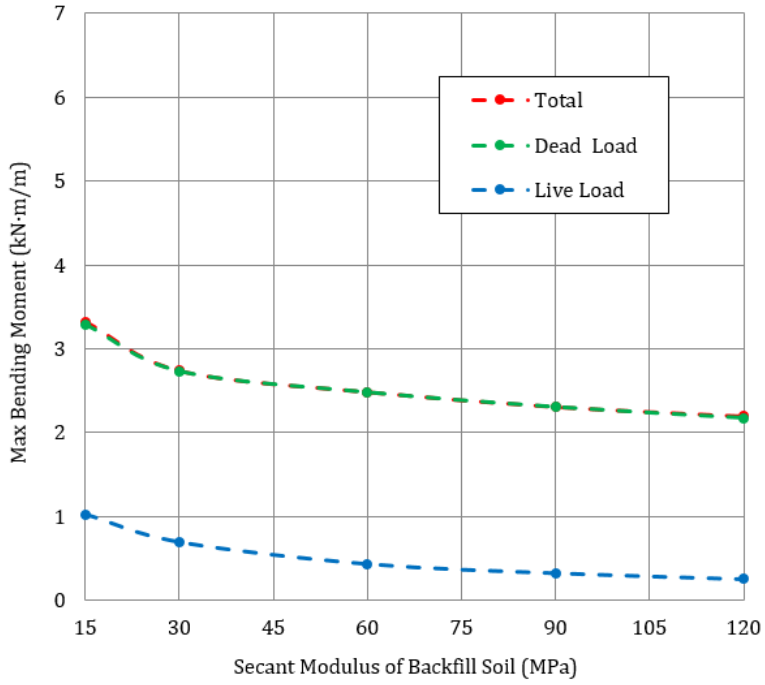

Figure 4.12 Effect of secant modulus of backfill soil on the maximum bending moment.

4.3.5 Effect of Internal Friction Angle of Backfill Soil

In general, the internal frictional angle of the backfill did not have an appreciable effect on either the maximum thrust (Figure 4.17) nor the maximum bending moments (Figure 4.20) in the pipe. These results may be influenced by the small amount of cohesion (5 kPa) that was used to prevent numerical instability. It is possible that the cohesion value was just large enough to reduce the amount of local yielding that would have otherwise occurred in the Backfill Soil around the pipe by a non-negligible amount.

Figure 4.13 shows that both the maximum dead and live load thrusts decreased very slightly as the friction angle increased. This is attributed to the increase in positive arching that is expected with a reduction in shear strength of the soil directly above the pipe. A similar relationship was observed between the friction angle and the maximum dead and live load moment (Figure 4.14).

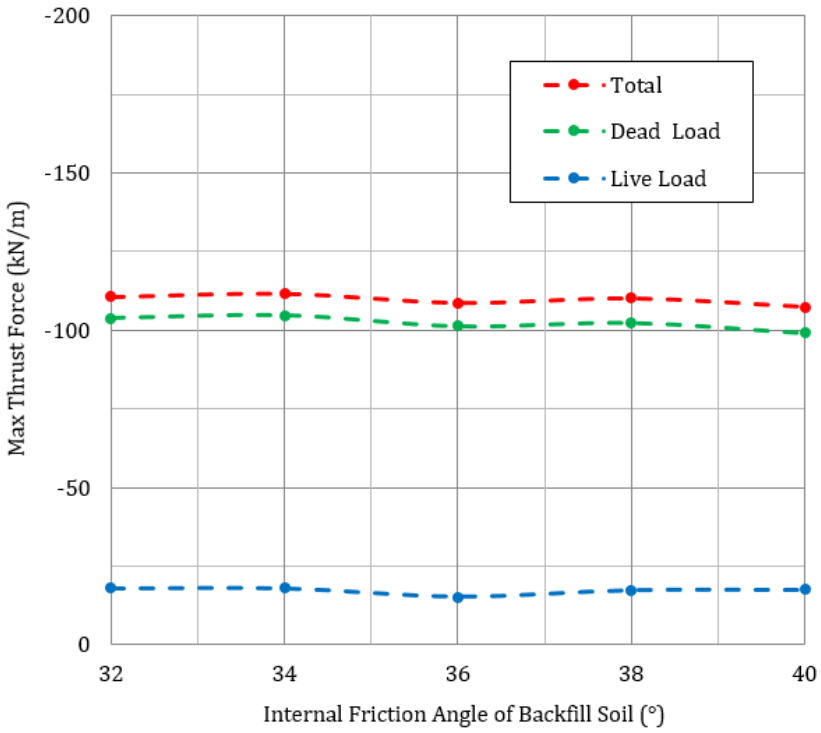

Figure 4.13 Effect of internal friction angle of backfill soil on maximum thrust.

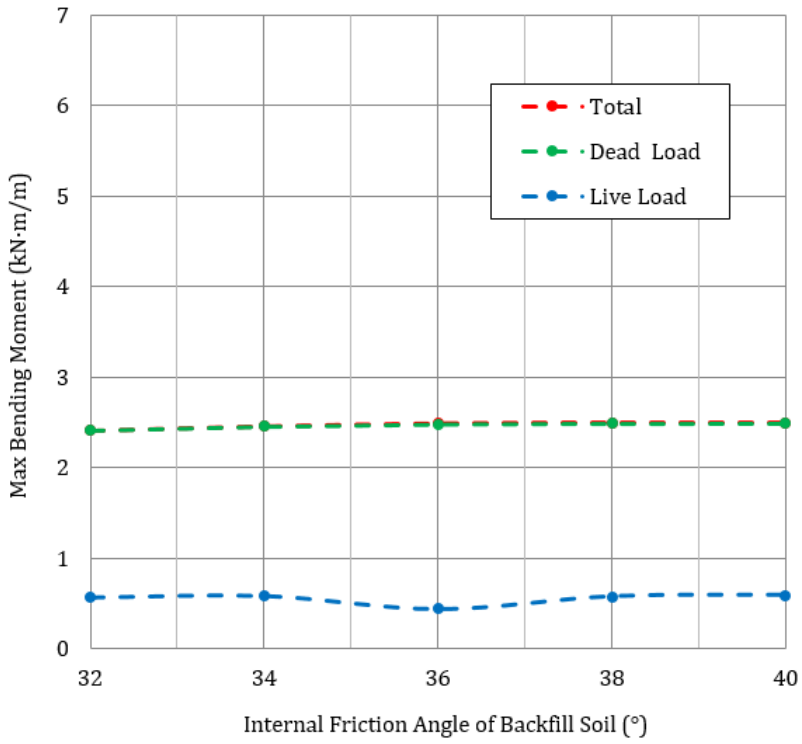

Figure 4.14 Effect of internal friction angle of backfill soil on the maximum bending moment.

4.3.6 Effect of Strength Reduction Factor of Soil-Pipe Interface

The strength reduction factor of the soil-pipe interface, R_{inter}, had the third largest effect on the maximum total thrust in the pipe (Figure 4.17) and the second smallest effect on maximum total bending moments (Figure 4.20).

Figure 4.15 shows how both the maximum dead and live load thrust increases with increasing R_{inter}. This is attributable to positive soil arching. When the backfill soil is able to slip across the pipe more easily, a greater portion of the applied load can flow around the pipe, instead of being transferred through it. This effect is more pronounced in the dead load thrust curve than in the live load thrust curve, probably due to the geometry of the wheelprints in the baseline case (i.e. the wheelprints are outside of the pipe outline, and a significant portion of the load is already transferred away from the pipe, without help from arching).

Figure 4.16 does not reveal a clear trend between R_{inter} and the maximum dead or live load bending moments. Furthermore, the small variation of magnitude of bending moment suggest that it is relatively insensitive to R_{inter}.

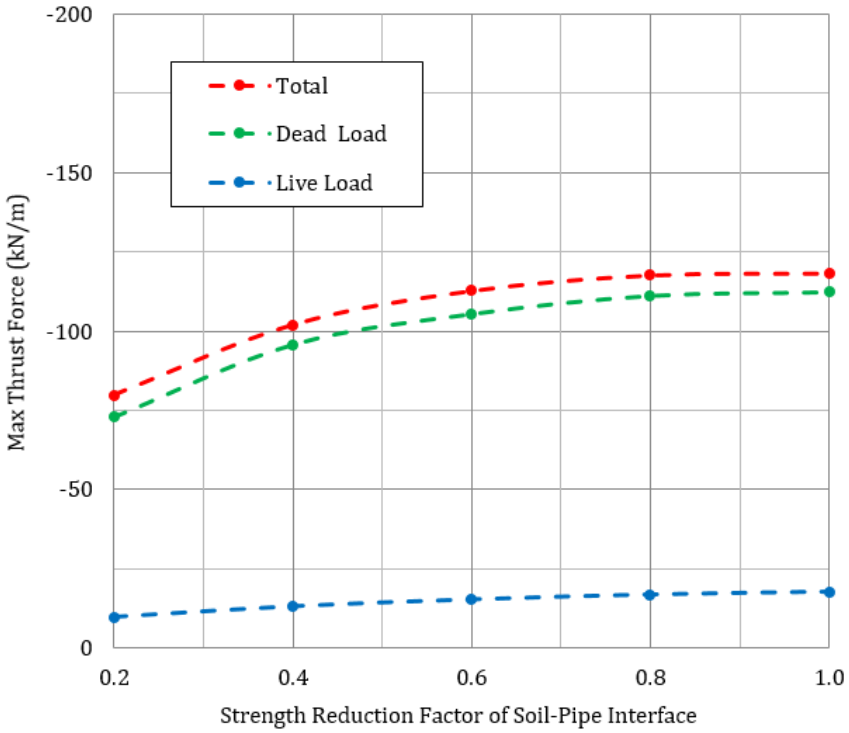

Figure 4.15 Effect of strength reduction factor of the soil-pipe interface on maximum thrust.

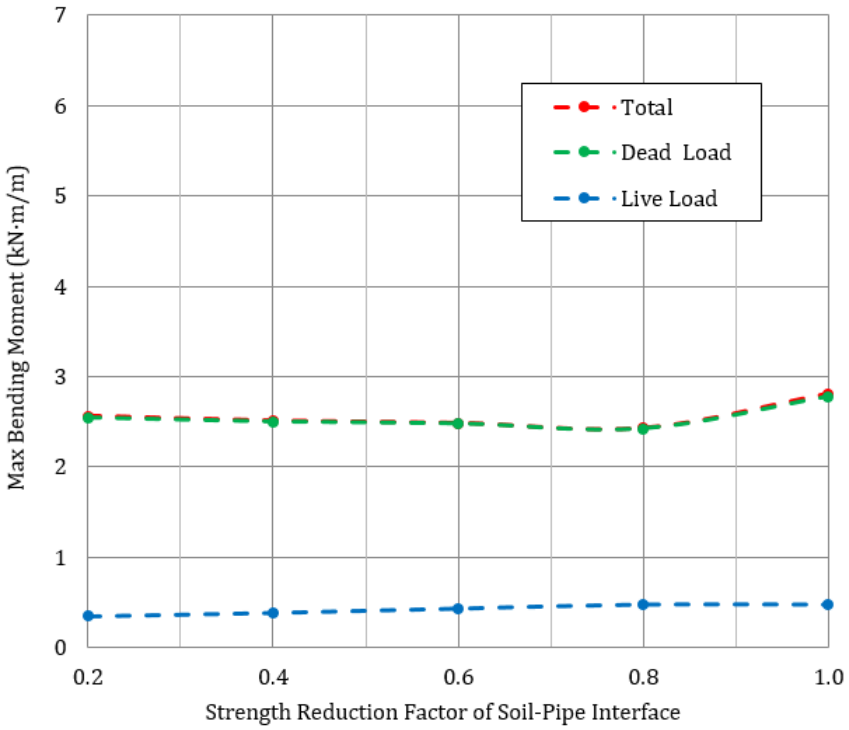

Figure 4.16 Effect of strength reduction factor of the soil-pipe interface on the maximum bending moment.

4.3.7 Sensitivity Analysis

Figure 4.17 through Figure 4.21 present a graphical summary of the results in the form of "Tornado" sensitivity plots. In these plots, the study parameters are listed along the y-axis, and the output variable is plotted on the x-axis. The thick black vertical line represents the value of the output variable for the baseline case. In addition to the baseline values, the plot illustrates the degree to which the output variable is affected as each input parameter is varied from its minimum to maximum anticipated value. The input parameters are sorted from top to bottom in order of largest to smallest total range of the output variable. Thus, the most critical input parameter is shown at the top, while the least critical is shown at the bottom.

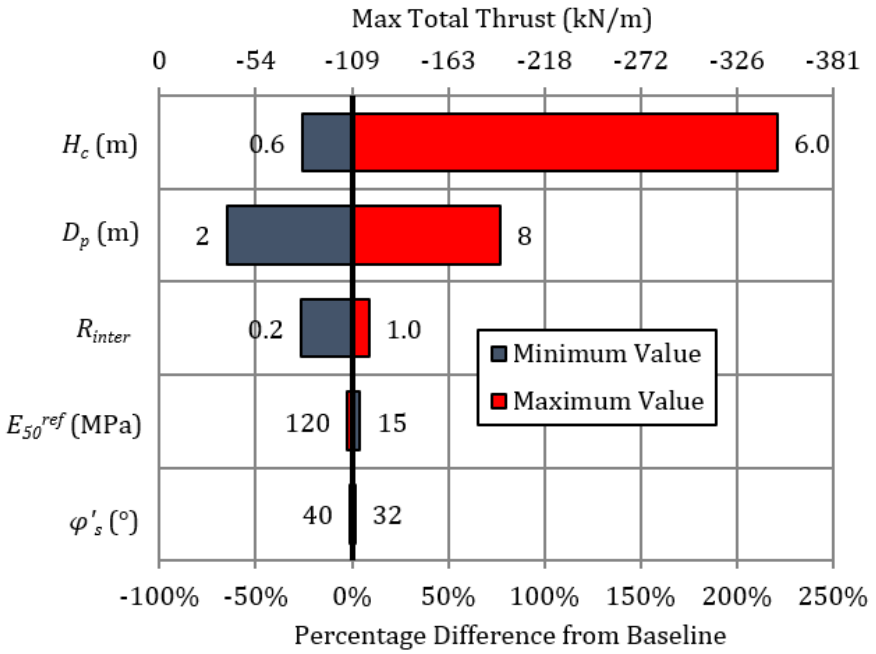

Figure 4.17 Sensitivity plot for the maximum total thrust around the pipe.

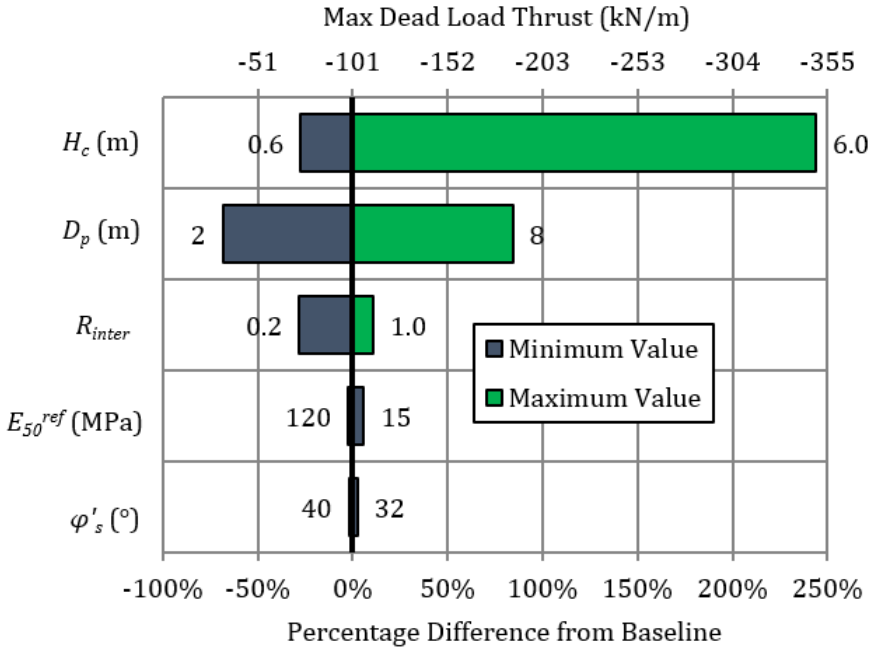

Figure 4.18 Sensitivity plot for the maximum dead load thrust around the pipe.

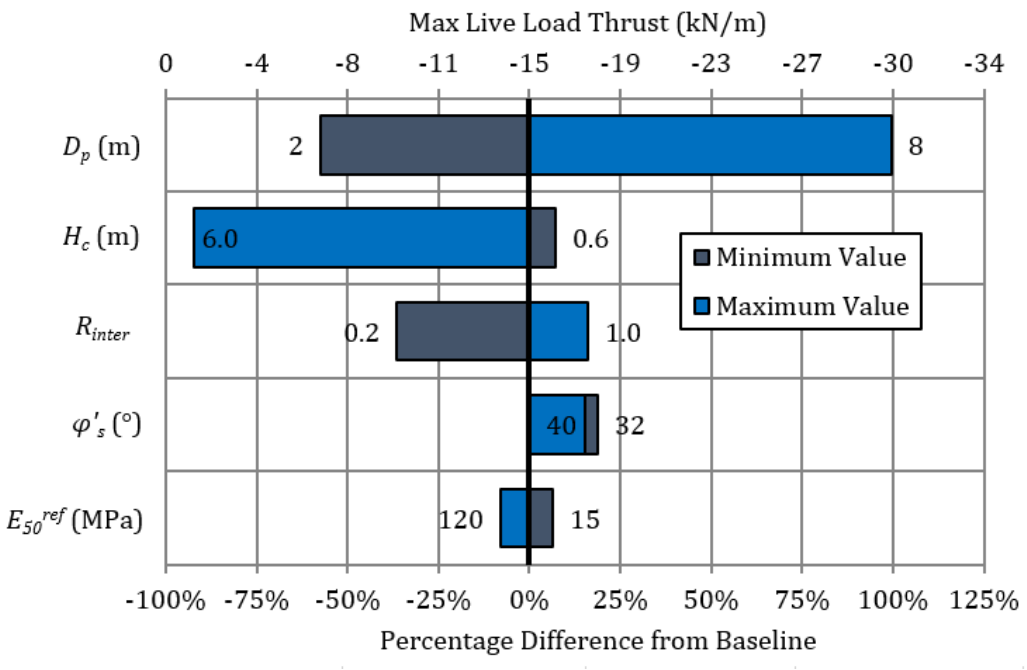

Figure 4.19 Sensitivity plot for the maximum live load thrust around the pipe.

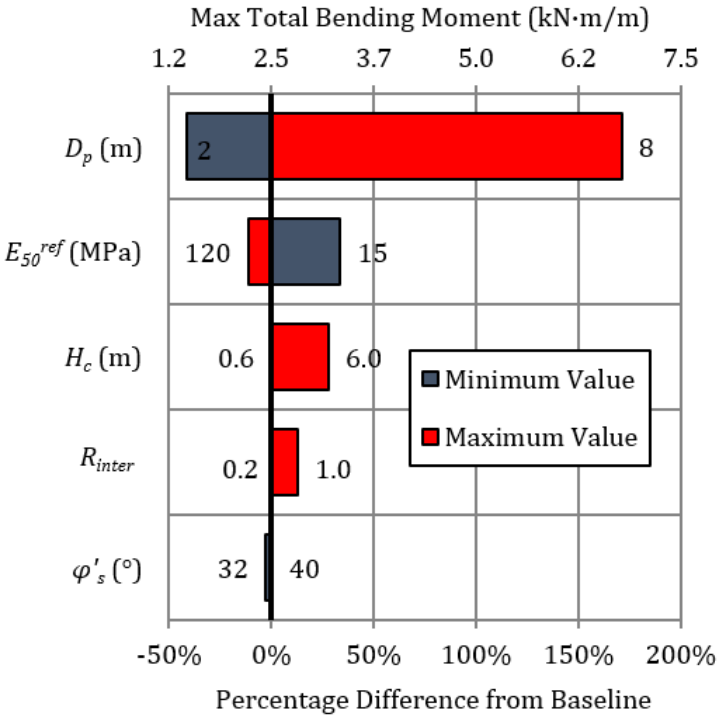

Figure 4.20 Sensitivity plot for the maximum total bending moment around the pipe.

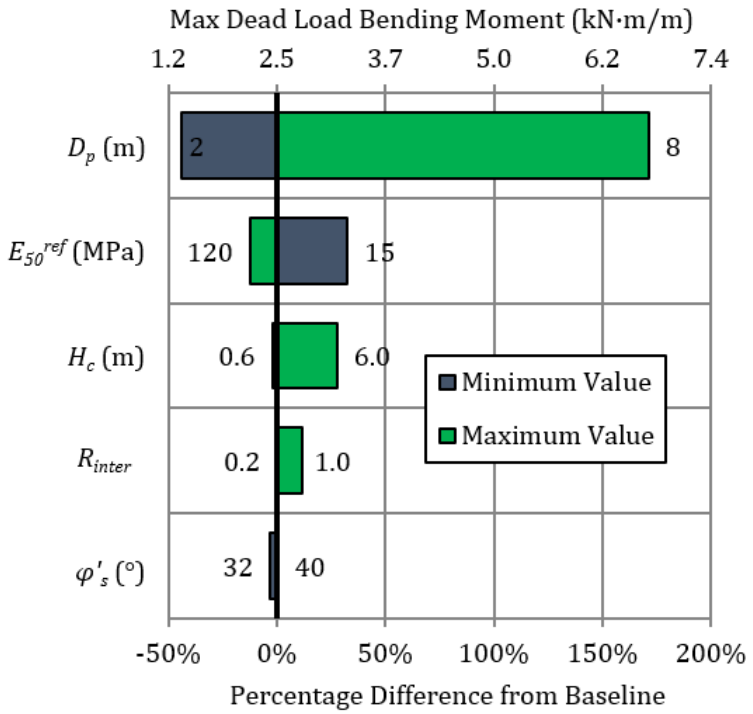

Figure 4.21 Sensitivity plot for the maximum dead load bending moment around the pipe.

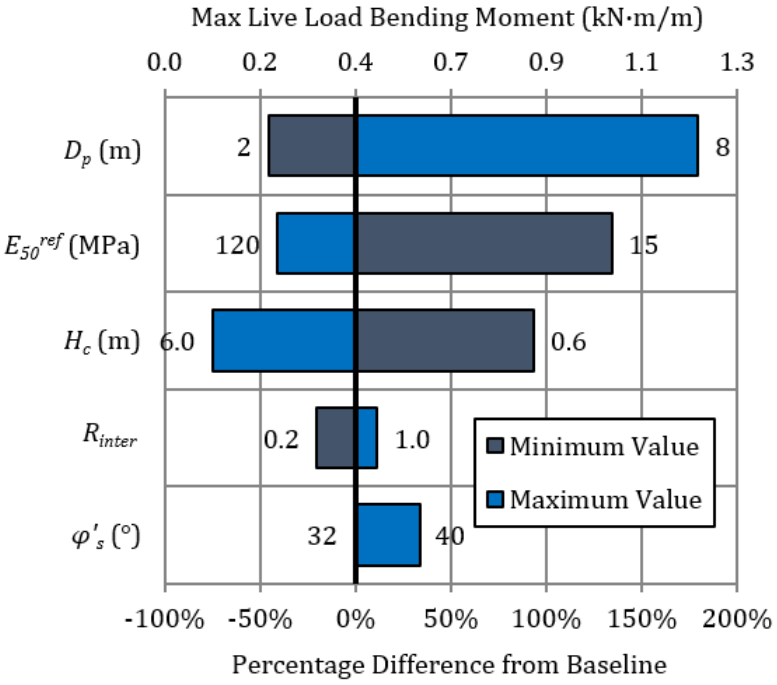

Figure 4.22 Parametric sensitivity plot for the maximum live load bending moment around the pipe.

4.4 Conclusions

A 3D finite element model was used to carry out a parametric study for intact (non-corroded), round CMP culverts. Five (5) input parameters were considered in terms of their effects on the thrusts and bending moments in the culvert pipe. Upon observation of the results, the following conclusions are made:

1. The maximum dead load thrust always occurred just below the springlines.
2. The maximum live load thrust always occurred at the crown.
3. The maximum dead load bending moments occurred in two (2) places: just below the springlines and just below the haunches.
4. The maximum live load bending moment occurred just above the shoulders.
5. Although maximum total bending moments are small (maximum moment for the baseline case = 2.8 kN), the bending stresses are generally of the same order of magnitude as the axial stresses, and are greater than the axial stresses at the locations of maximum bending moment(s).
6. Overall, the total pipe forces are most sensitive to the pipe diameter and the height of soil cover. The former suggests that pipe flexibility is a critical input parameter (i.e. changes to the profile of the corrugated plate would also have a major influence on the pipe forces).
7. The secant modulus of the soil and the strength reduction factor of the soil-pipe interface had a moderate influence on the total pipe forces.
8. The soil friction angle had the smallest influence on the total pipe forces.
9. The height of soil cover had a significantly larger influence on the maximum total thrust (range = 245% of baseline value) than on the maximum total bending moment (range = 110% of baseline value).
10. The secant modulus of the soil had a significantly larger influence on the maximum total bending moment (range = 45% of baseline value) than on the maximum total thrust (range = 5% of baseline value).

CHAPTER 5:
PARAMETRIC STUDY FOR CORRODED CORRUGATED METAL PIPE CULVERTS

5.1 Introduction

Most corrugated metal pipe (CMP) culverts are subject to degradation of the pipe material from the combined effects of abrasion and corrosion. Although it is usually a simple matter to identify the presence of corrosion, it is not obvious how corroded zones—which can vary in their position, severity, and extent across the surface of the CMP—affect the overall structural integrity of the culvert. Examples of corroded culverts are shown in Figure 5.1.

Figure 5.1 Examples of corroded CMP culverts in Canada (Campbell, 2017)

This chapter presents results from a parametric study investigating the effects of pipe corrosion on the stability of round CMP culverts. Previous work by El-Taher (2009) concluded that the critical failure mode is wall crushing due to yielding of the pipe plate, provided there are no erosion voids in the backfill soil adjacent to the pipe. In this study, buckling stability is assessed using the design equations from the Canadian Highway Bridge Design Code (CSA, 2014). The current study does not consider the effects of erosion voids in the backfill soil.

The purpose of the parametric study was to determine how the culvert stability is influenced by pipe corrosion of various magnitudes and three-dimensional geometries. El-Taher and Moore (2008) concluded that pipe corrosion (i.e. reduction in plate thickness) across the invert has negligible effect on thrusts and bending moments in the CMP, and therefore the reduction in factor of safety against yield is directly proportional to the reduction in plate thickness. Their findings were based on two-dimensional (2D) finite element models, which employed elastic backfill soil and did not consider the effects of live loading. The current study is based on three-dimensional (3D) finite element analyses, which employ a non-linear, strain-hardening soil model and include live-loading.

5.2 Numerical Details

5.2.1 Study Parameters

Four (4) corrosion variables were evaluated in terms of their influence on the structural forces (thrust and bending moment) and stresses in the pipe under combined dead and live loading conditions:

1. Circumferential Corrosion Pattern;
2. Percentage of Intact Plate Thickness Remaining P_t;
3. Circumferential Extent of Corrosion, θ_c; and
4. Longitudinal Extent of Corrosion, L_c.

Figure 5.2 illustrates the four (4) different circumferential corrosion patterns considered in this study: 'Full Circumference', 'Invert', 'Crown', and 'Haunches'. Each pattern describes the position(s) of the corroded zone(s) around the CMP. The position of a corroded zone is defined by its point of symmetry (angle around pipe measured clockwise from the crown). The point of symmetry is located at 180° for the 'Invert' corrosion pattern and 0° for the 'Crown' pattern. The 'Haunches' pattern has two (2) separate corroded zones (one at each haunch), each having its own point of symmetry (120° and 240°). The 'Full Circumference' pattern is a special case in which the corroded zone is symmetrical about all points around the circumference.

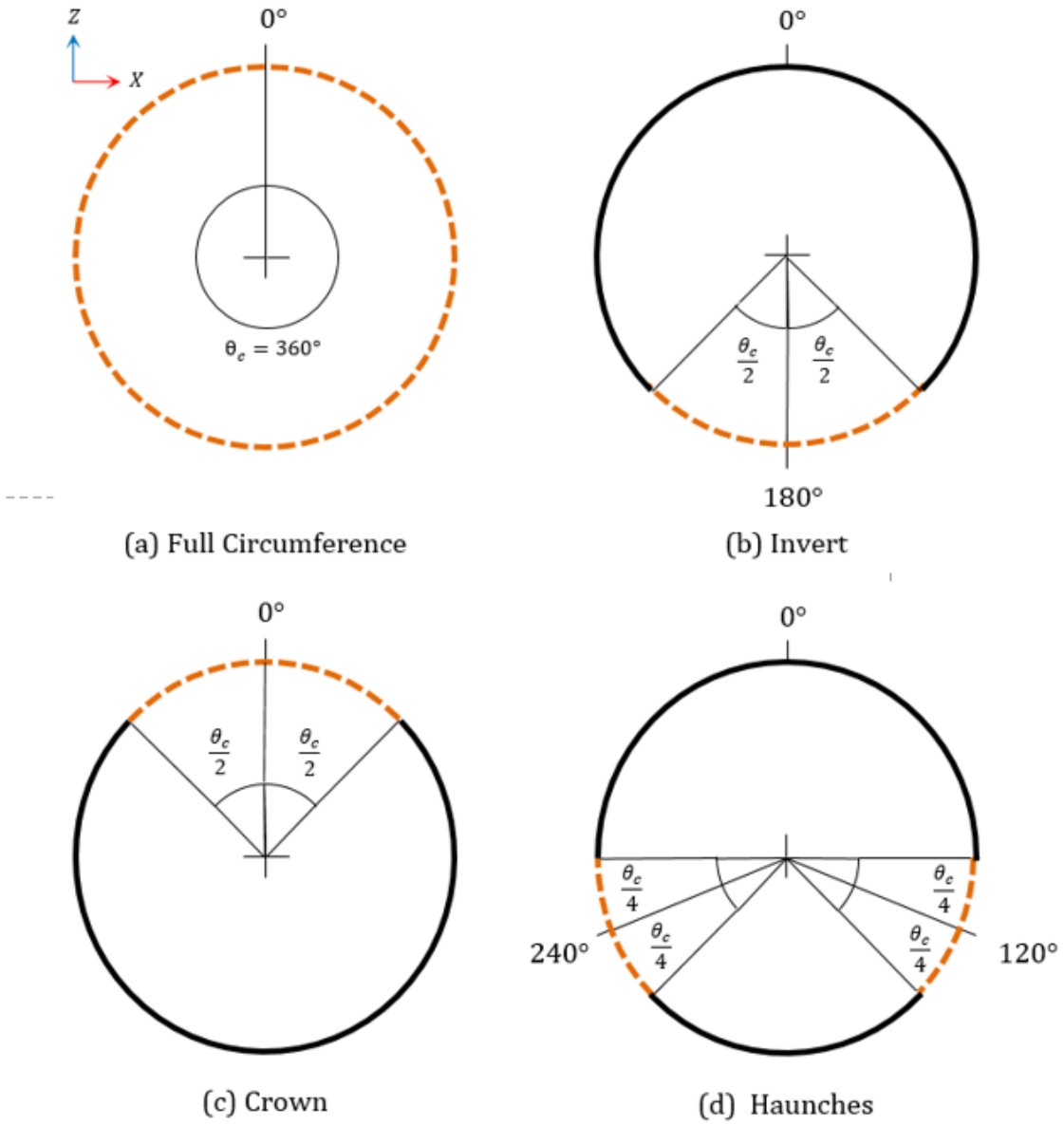

Figure 5.2 Four (4) circumferential corrosion patterns considered in the parametric study.

The geometry of the corroded zone is further defined by the circumferential extent of corrosion, θ_c, i.e. the angular proportion of the pipe circumference occupied by the corroded zone (ranging from 0° to 360°). The case θ_c = 0° represents the intact condition, while θ_c = 360° is a special case that can be considered as a unique pattern ('Full Circumference') or an upper limit of the 'Invert' or 'Crown' patterns. The maximum value of θ_c for the 'Haunches' pattern is technically less than 360°; the two corroded zones would overlap for θ_c > 270° (based on the fixed points of symmetry

that have been somewhat arbitrarily assigned to that corrosion pattern). The upper limit for a corrosion pattern with points of symmetry at 90° and 270° would be θ_c = 360°

The longitudinal extent of corrosion, L_c, describes the length of the corroded zone, which can range from 0 m (representing the intact condition) to the full length of the pipe, L = 40 m. (a check performed in Chapter 4 confirmed that, at this length, the model boundaries have no influence on the pipe at its longitudinal centre, where the pipe response is being evaluated). All corroded zone(s) in this study are symmetrical about the pipe's longitudinal midpoint, as illustrated in Figure 5.3.

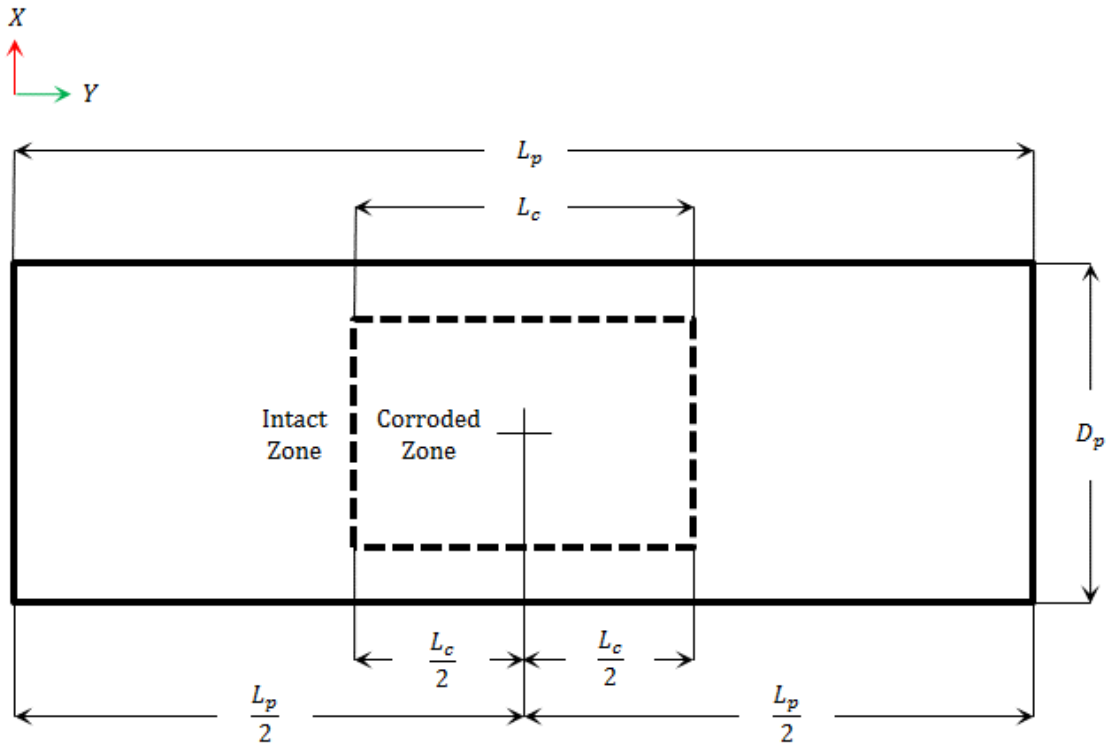

Figure 5.3 Definition of the longitudinal extent of corrosion, L_c.

The percentage of intact plate thickness remaining, P_t, is defined by Equation 5.1:

$$P_t = \left(\frac{t}{t_0}\right) \times 100 \qquad 5.1$$

where t_0 and t are the intact (i.e. pre-corrosion) and remaining (i.e. post-corrosion) plate thicknesses, respectively. In theory, P_t can range from 0 to 100%, but the smallest value of P_t considered in this study is 20%. Since corrosion tends not to develop perfectly-uniformly, once the average percentage of remaining plate thickness in the corroded zone reaches 20%, there will likely be many local areas that are fully perforated. In such cases, deterioration of the backfill soil is likely to have occurred, and additional analysis would be required to properly assess culvert stability.

The parametric study consisted of running forty-eight (48) simulations in total. The influence of each of the 4 (four) corrosion parameters was assessed by varying the value of a parameter while holding all other variables constant. All results were compared to those for the "intact" case, i.e. P_t = 100%. The full range of values considered for each of the four (4) study parameters is given in Table 5.2.

Table 5.1 Variable values used in the parametric study of corroded culverts.

Parameter	Symbol	Values	Units
Circumferential Corrosion Pattern	-	Full Circumference [1], Invert, Crown, Haunches	-
Percentage of Intact Plate Thickness Remaining	P_t	100, 80, 60, 40, 20	%
Circumferential Extent of Corrosion	θ_c	20, 60, 90, 150, 180, 360 [1]	°
Longitudinal Extent of Corrosion	L_c	0.8, 1.6, 4, 8, 20, 40	m

[1] The 'Full Circumference' pattern is a special case where θ_c = 360°.

5.2.2 Geometry, Mesh, and Boundary Conditions

The three-dimensional geometry of the models used in this study is the same as those used in the baseline case from Chapter 4, as described in Section 4.2.1 The lateral boundaries were placed about 4 times the diameter of the pipe in the two lateral directions. In the longitudinal direction, the model length was set to be 40 m (i.e. 8*D*). The bottom model boundary was placed about 3.5D below the invert of the pipe.

Results of sensitivity analyses indicated that further extension of the model boundaries had negligible effects on the output from the area of interest (i.e. near the centre of the model).

The natural ground and the backfilling envelope were modelled using higher order 10-node tetrahedral elements. The model comprised around 300,898 elements with an average element size around the culvert of 334 mm. The large number of small-sized elements assured high accuracy, especially at locations where nonlinear behaviour was anticipated, especially near the pipe. Figure 5.4 shows the FE mesh from the simulation of haunch corrosion.

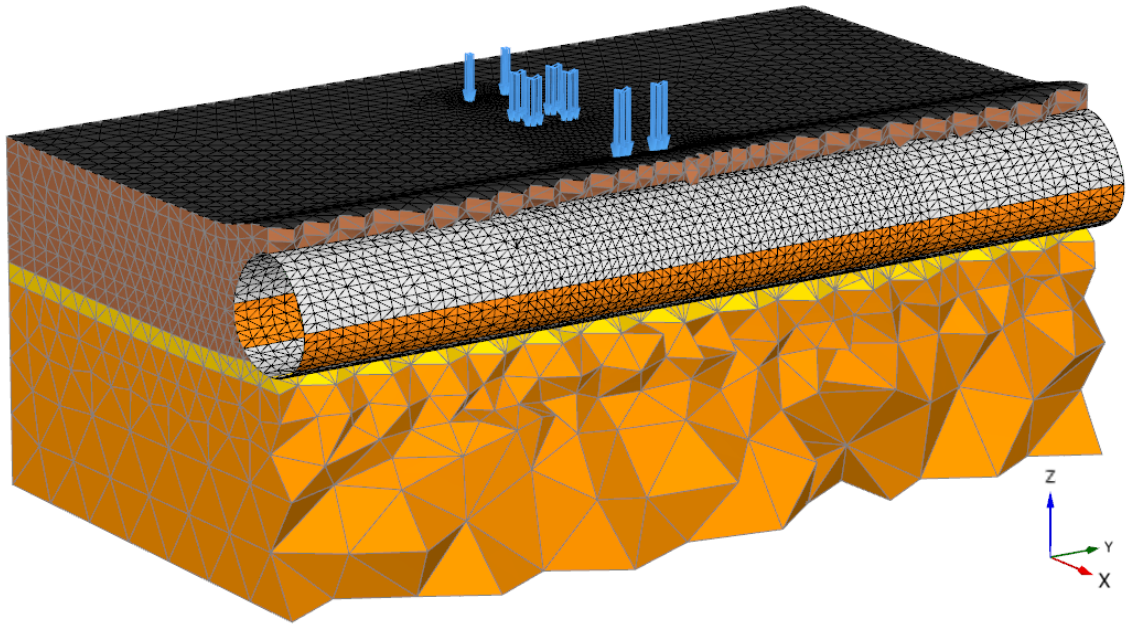

Figure 5.4 Cutaway section of the 3D finite element mesh used in the parametric study for corroded CMP culverts ('Haunch' corrosion pattern, θ_c = 90°, L_c = L).

The geometry, mesh, and boundary conditions of the models used in this study were the same as those used in the baseline case from Chapter 4, as described in Section 4.2.1.

5.2.3 Material Properties

The material properties used in the finite element models for this study were generally the same as those used in the baseline case from Chapter 4, as described in

Section 4.2.2. The material properties used to model the corroded pipe are presented in Table 5.2.

Table 5.2 Input parameters of the orthotropic plate used to model the CMP for various degrees of corrosion.

Parameter		Symbol	Percentage of intact plate thickness remaining, P_t					Units
			100%	80%	60%	40%	20%	
Plate thickness		$\bar{t} = d$	60.36	60.36	60.36	60.36	60.36	mm
Unit weight		$\bar{\gamma} = \gamma$	7.84	6.27	4.71	3.14	1.57	kN/m^3
Elastic moduli	Circumferential	$\bar{E}_\theta = E_2$	20,373,235	16,298,588	12,223,941	8,149,294	4,074,647	kPa
Elastic moduli	Longitudinal	$\bar{E}_L = E_1$	113,662	58,195	24,551	7,274	909	kPa
Poisson's ratio		$\bar{\nu}_p = \nu_{12}$	0	0	0	0	0	-
Shear moduli	Circumferential Out-of-plane	$\bar{G}_{\theta R} = G_{23}$	7,835,860	6,268,688	4,701,516	3,134,344	1,567,172	kPa
Shear moduli	Longitudinal Out-of-plane	$\bar{G}_{LR} = G_{13}$	43,716	22,383	9,443	2,798	350	kPa
Shear moduli	In-plane	$\bar{G}_{L\theta} = G_{12}$	585,282	374,580	210,701	93,645	23,411	kPa

5.2.4 Modelling Sequence and Loading Conditions

The modelling sequence and loading conditions used in this study are the same as those used in the baseline case from Chapter 4.

5.3 Results and Discussion

Unless otherwise noted, results discussed in this section pertain to the cross-section of the CMP in the centre of the model, i.e. in the same vertical plane as the centreline of the live load truck wheelprints.

5.3.1 Limiting Case

This section presents the results for a limiting case representing severe corrosion over the entire 2D pipe surface, i.e. P_t = 20%, θ_c = 360°, and L_c = L = 40 m. Results for the limiting case are compared to those for the intact case, i.e. P_t = 100%. The effects of each individual corrosion parameter are discussed in sections 5.3.2 to 5.3.5.

5.3.1.1 Thrusts

Figure 5.5 shows that the maximum live load thrust in the corroded pipe (-11.8 kN/m for P_t = 20%) was *less* than in the intact pipe (-15.2 kN/m). The reduction in thrust can be attributed to positive soil arching over the pipe caused by increased downward deflection of the crown (and thus the soil directly above the crown).

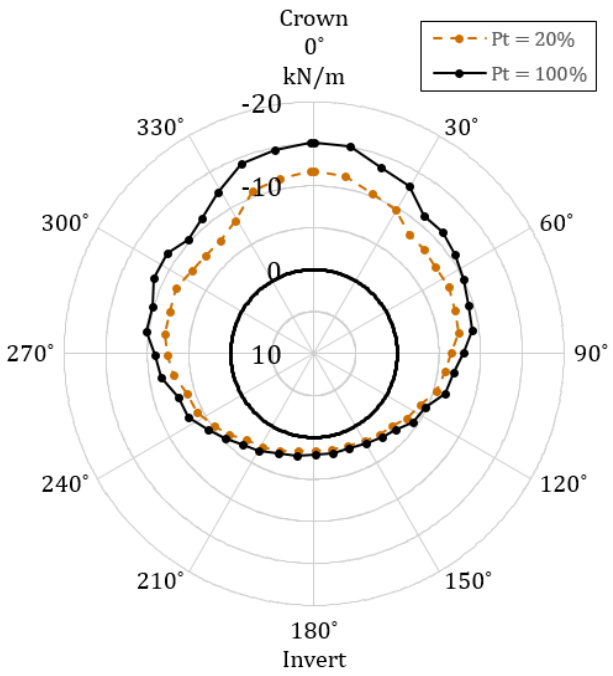

Figure 5.5 Effect of corrosion on the live load thrust distribution (θ_c = 360°, $L_c = L_p$).

Although the reduction of live load thrust was substantial (-22.5%), the maximum total thrust—which occurs just below the springlines—was barely affected. The maximum total thrust (107.2 kN/m) was only 1.5% less than in the intact case (108.8 kN/m).

5.3.1.2 Bending Moments

Figure 5.6 shows that live load bending moments were reduced everywhere above the springlines. This observation is also attributed to positive soil arching. The maximum live load bending moment in the corroded pipe (-0.131 kN·m/m) was 70% less than in the intact pipe (-0.442 kN·m/m). However, the maximum total bending moment (located at the haunches) was unaffected (-0.1% of intact).

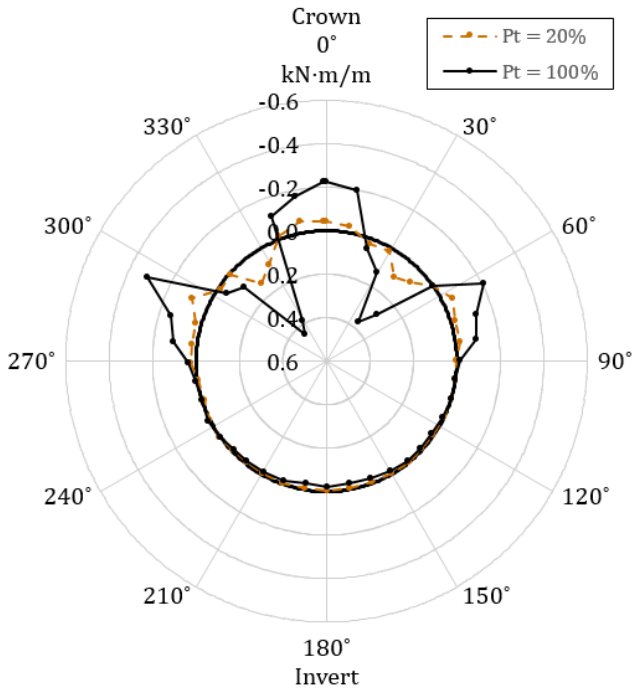

Figure 5.6 Effect of corrosion on the live load bending moment distribution (θ_c = 360°, L_c = L).

5.3.1.3 Normal Stresses

The normal stresses at the inner (σ_{in}) and outer (σ_{out}) extreme fibers of the CMP plate section resulting from combined axial (σ_a) and bending (σ_a) stresses were computed using Equations 5.2 and 5.3, where T and M are the circumferential thrust force and bending moment in the CMP. The normal stress, σ, reported in this section and subsequent sections refers to the greater of the two extreme fiber stresses (Equation 5.4). This is done to avoid confusion with σ_{max}, which is reserved for the maximum normal stress around the entire circumference of the pipe. A sample stress calculation is provided in Appendix B.

$$\sigma_{in} = \sigma_a - \sigma_b = \frac{T}{A} - \frac{My}{I} \quad 5.2$$

$$\sigma_{out} = \sigma_a + \sigma_b = \frac{T}{A} + \frac{My}{I} \quad 5.3$$

$$\sigma = \max(|\sigma_{in}|, |\sigma_{out}|) \quad 5.4$$

Figure 5.7 compares the distribution of (maximum) normal stresses around the corroded and intact pipes. Although even severe corrosion appears to have minimal effect on the total forces (thrusts and bending moments), the normal stresses increase due to the reduction in cross-sectional area of the corrugated plate. The maximum normal stress in the corroded pipe was 398% greater (-256.3 MPa) than in the intact pipe (-51.5 MPa).

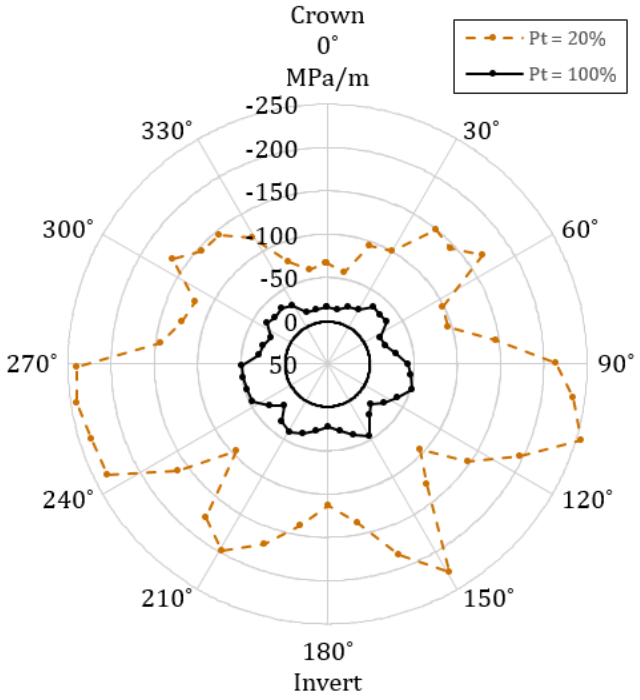

Figure 5.7 Effect of corrosion on the maximum normal stress distribution (θ_c = 360°, L_c = L).

5.3.1.4 Factor of Safety against Yielding

The factor of safety against yielding, FS_y, was computed according to Equation 5.5

$$FS_y = \frac{\sigma_y}{\sigma} \qquad 5.5$$

Since corrosion causes the normal stresses to increase while the yield strength of the steel remains the same, FS_y is reduced, as shown in Figure 5.8. The minimum factor of safety against yielding, $FS_{y(\min)}$—which occurs just below the springlines—is 79.9% lower in the corroded pipe (0.90) than in the intact pipe (4.47).

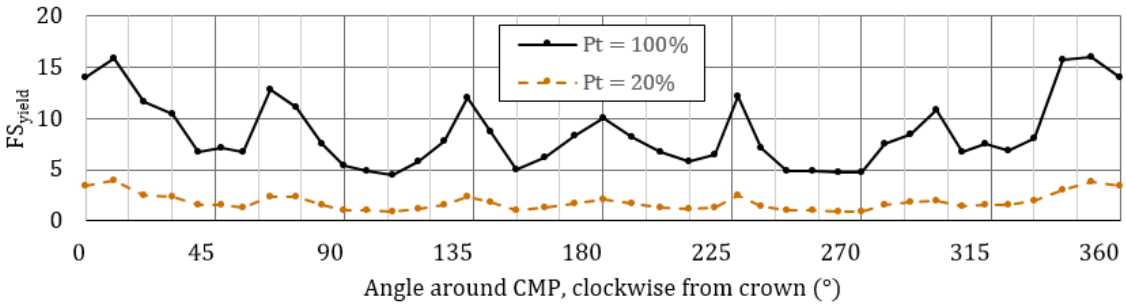

Figure 5.8 Effect of corrosion on the distribution of factor of safety against yielding around the CMP (θ_c = 360°, $L_c = L$).

5.3.1.5 Factor of Safety against Buckling

The factor of safety against buckling, FS_b, was calculated using Equation 5.6:

$$FS_b = \frac{f_b}{\sigma_a} \tag{5.6}$$

The buckling strength f_b was calculated using the method developed by Abdel-Sayed (1978), which is the basis for section 7.6.3.2 of the CHBDC (CSA, 2014). The pipe circumference is divided into the following two zones: the lower zone, in which radial displacements of the wall are toward the soil; and the upper zone, in which radial displacements of the wall are toward the inside of the pipe. The upper zone extends $\pm\theta_0$ from the crown. The angle θ_0 (in radians) is calculated using Equation 5.7:

$$\theta_0 = 1.6 + 0.2 \log\left[\frac{EI}{E_m R^3}\right]; \tag{5.7}$$

where R is the centroidal radius of the pipe and E_m is the modified modulus of soil stiffness. For the lower zone, E_m is equal to the secant modulus of soil stiffness, E_s, but for the upper zone it is calculated using Equation 5.8:

$$E_m = E_s\left[1 - \left[\frac{R_c}{R_c + 1000[H + H']}\right]^2\right] \tag{5.8}$$

where R_c is the pipe radius at the crown (for round CMPs $R_c = R$), H is the height of cover, and H' is half the vertical distance between the crown and springline.

A factor representing the relative stiffness of the conduit wall, K, is then computed from Equation 5.9:

$$K = \lambda \left[\frac{EI}{E_m R^3}\right]^{0.25} \quad 5.9$$

For the lower zone, λ is equal to 1.22, but for the upper zone it is calculating using Equation 5.10:

$$\lambda = 1.22\left[1.0 + 1.6\left[\frac{EI}{E_m R_c^3}\right]^{0.25}\right] \quad 5.10$$

An equivalent radius, R_e, is then calculated for both the upper and lower zones as per Equation 5.11:

$$R_e = \frac{r}{K}\left[\frac{6E\rho}{F_y}\right]^{0.5} \quad 5.11$$

Where r is the radius of gyration of the pipe plate, F_y is the yield stress of the pipe material, and ρ is a reduction factor for buckling stress computed using Equation 5.12:

$$\rho = \left[1000\frac{(H + H')}{R_c}\right]^{0.5} \geq 1.0 \quad 5.12$$

Finally, the buckling strength f_b can be calculated using Equation 5.13 if $R \leq R_e$ (which refers to inelastic buckling), or Equation 5.14 if $R > R_e$ (which refers to elastic buckling).

$$f_b = \phi_t F_m\left[F_y - \frac{\left(F_y KR\right)^2}{12Er^2\rho}\right] \quad 5.13$$

$$f_b = \frac{3\phi_t \rho F_m E}{\left[\frac{KR}{r}\right]^2} \quad 5.14$$

where ϕ_t = 0.8 for shallow-corrugated plates and F_m = 1.0 for single conduit structures.

The factor of safety against buckling, FS_b, around the intact and corroded CMPs are presented in Figure 5.9. The minimum factor of safety against buckling, $FS_{b(min)}$, again occurs just below the springlines (the point of maximum total thrust) and is reduced by 79.0% from P_t = 100% (9.79) to P_t = 20% (2.05). The reduction in buckling stability approximately equals the reduction in pipe plate thickness (-80%). For the limiting case considered here, FS_b > 1.0 at all points around the pipe, and is greater than or equal to FS_y everywhere around the pipe except within ±15° from the crown. Because the maximum total thrust was located just below the springlines, stability against yielding remains the critical design condition.

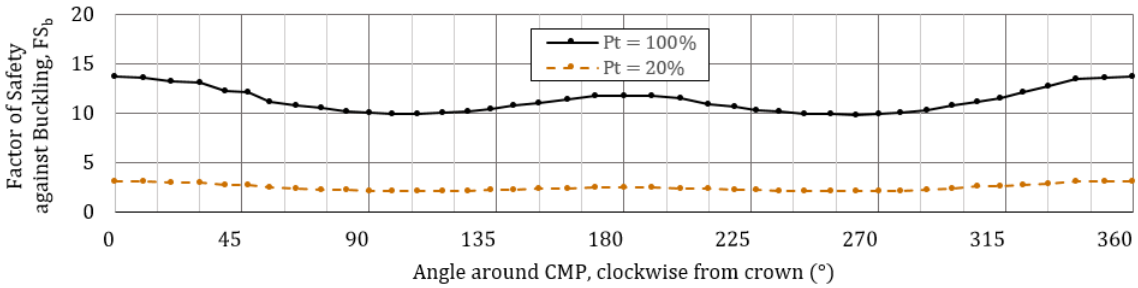

Figure 5.9 Effect of corrosion on the distribution of factor of safety against yielding around the CMP (θ_c = 360°, L_c = L).

5.3.2 Effect of Circumferential Corrosion Pattern

The influence of the circumferential corrosion pattern was evaluated by running a series of simulations and varying the corrosion pattern while holding the other parameters constant (i.e. P_t = 20% and L_c = L). One exception to this is the circumferential extent of corrosion, the value of which is unique for the 'Full Circumference' pattern (θ_c = 360°). For the 'Invert', 'Crown', and 'Haunches' patterns, θ_c = 90°.

5.3.2.1 Thrusts

Figure 5.10 shows the influence of the different circumferential corrosion patterns on the maximum live load thrust in the CMP. In all cases, the maximum live load thrust

is reduced (not increased) compared to the intact case. The largest reduction in maximum live load thrust was for the 'Full Circumference' pattern (-22.5%), followed closely by the 'Crown' pattern (-16.2%). The 'Haunches' pattern had a minor effect (-2.2%). The maximum live load thrust was essentially unaffected by 'Invert' corrosion (-0.2%).

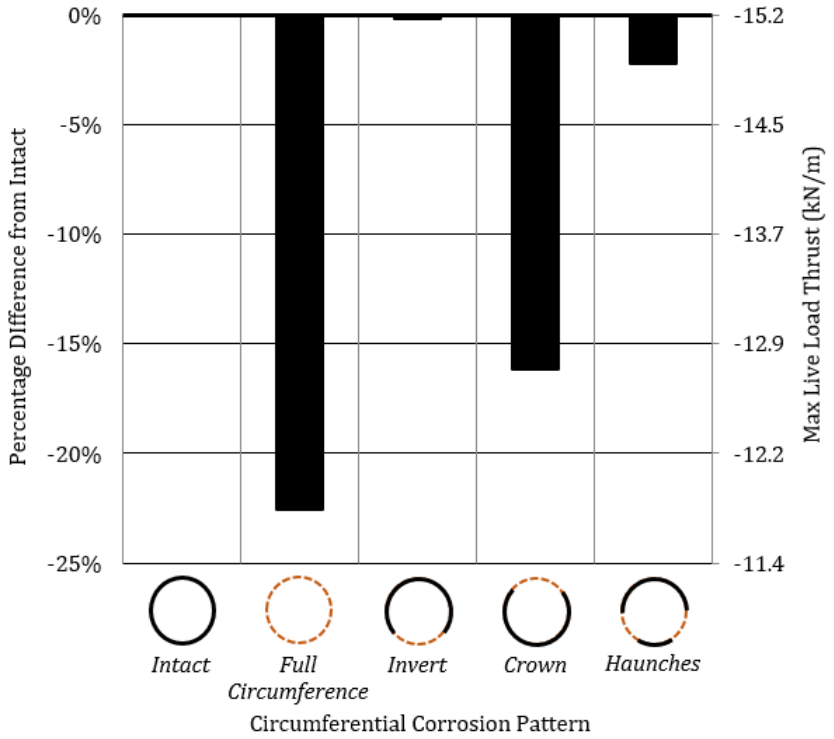

Figure 5.10 Influence of the circumferential corrosion pattern on the maximum live load thrust (P_t = 20%, L_c = L = 40 m).

5.3.2.2 Bending Moments

Figure 5.11 shows the influence of the different circumferential corrosion patterns on the maximum live load bending moment in the CMP. As for thrusts, the maximum live load bending moment was either reduced or unaffected in each case. The largest reduction in maximum live load bending moment was for the 'Full Circumference' pattern (-70.4%), followed closely by the 'Crown' pattern (-16.2%). The 'Haunches' pattern had a minor effect (-28.3%). The maximum live load bending moment was unaffected by either the 'Invert' (0.0%) or 'Haunches' (-0.2%) patterns.

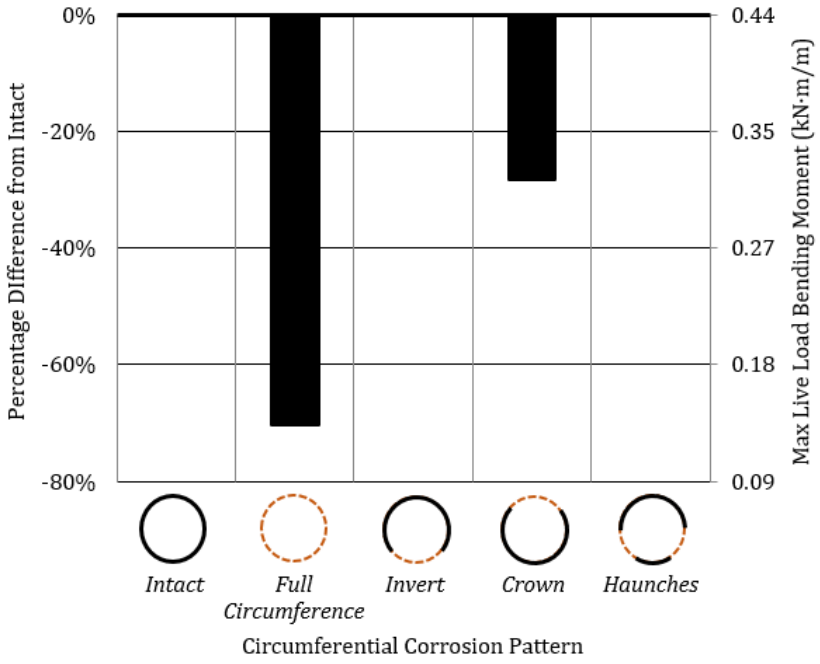

Figure 5.11 Influence of the circumferential corrosion pattern on the maximum live load bending moment (P_t = 20%, L_c = L = 40 m).

5.3.2.3 Normal Stresses

The distributions of maximum normal stress around the intact and corroded CMP for the various circumferential corrosion patterns are shown in Figure 5.12. The shape of the stress distribution remains the same in all cases, but the magnitude of stresses increases significantly in the corroded zones.

The maximum normal stress in the CMP was affected by all corrosion patterns, as shown in Figure 5.13. The 'Haunches' (+399.1%) and 'Full Circumference' (+398.0%) patterns cause the greatest increase, followed by 'Invert' (+345.2%) and 'Crown' (+192.6%).

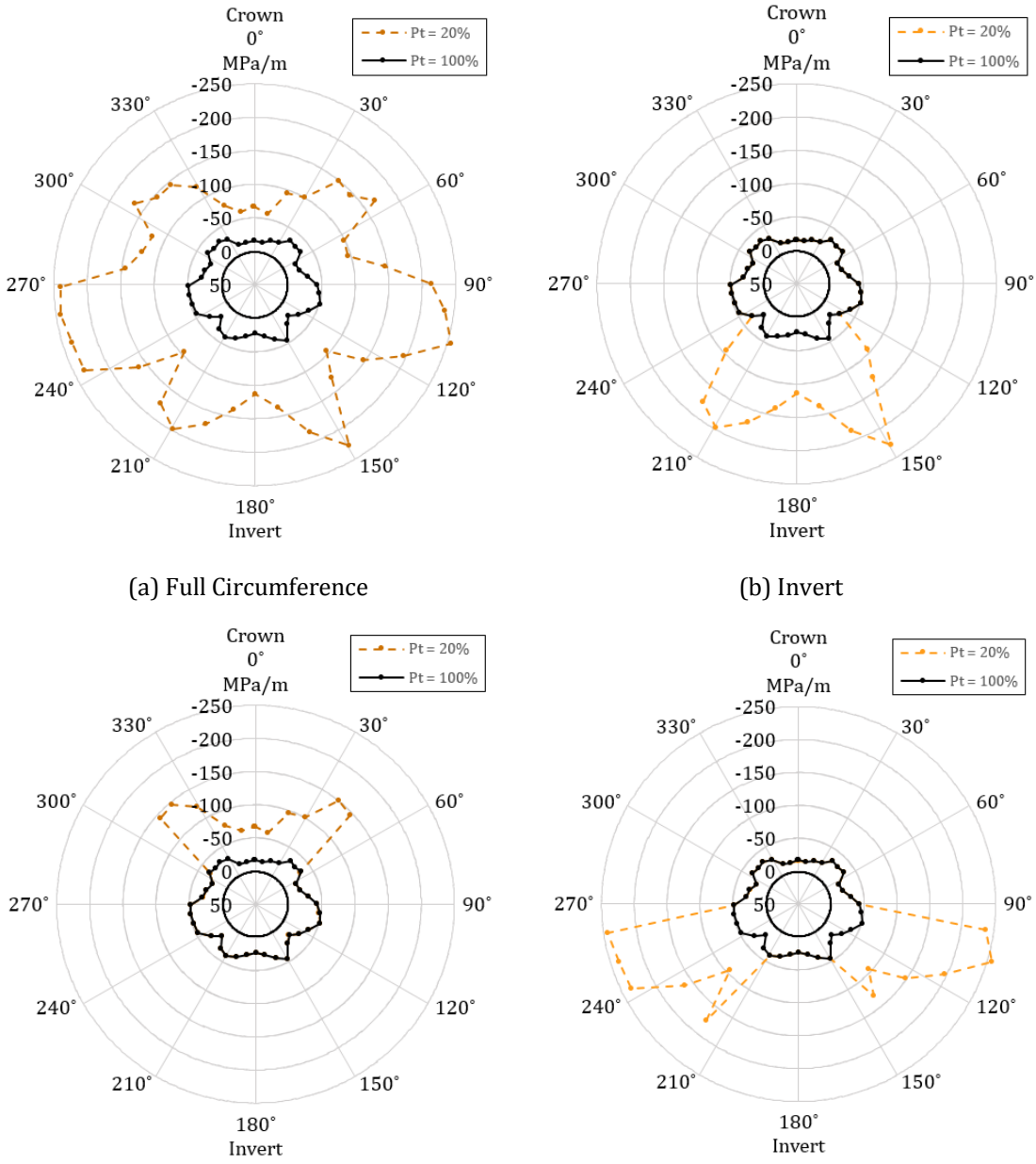

(a) Full Circumference

(b) Invert

(c) Crown

(d) Haunches

Figure 5.12 Maximum normal stress distribution around the CMP for different circumferential corrosion patterns: (a) 'Full Circumference' (θ_c = 360°); (b) 'Invert' (θ_c = 90°); (c) 'Crown' (θ_c = 90°); and (d) 'Haunches'. (θ_c = 90°).

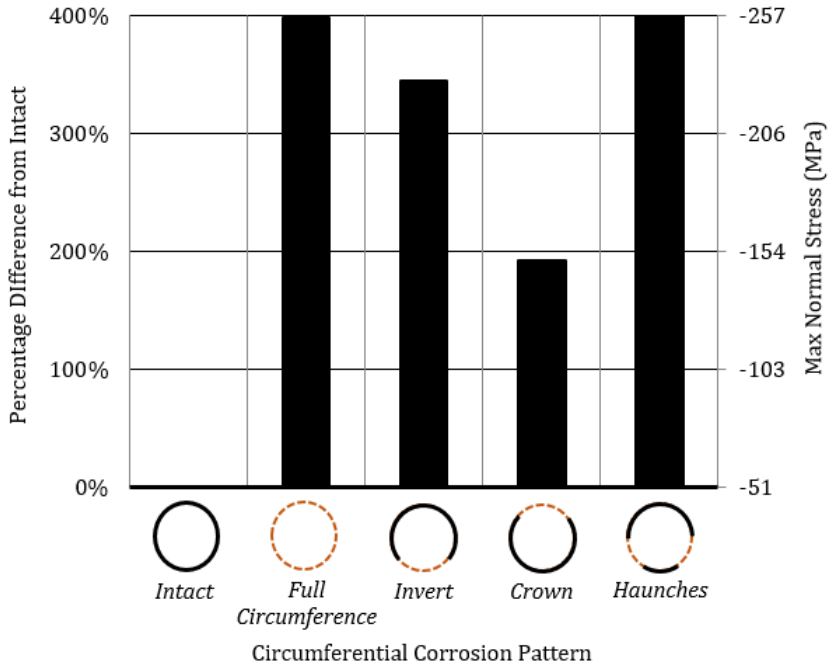

Figure 5.13 Influence of the circumferential corrosion pattern on the maximum normal stress (P_t = 20%, L_c = L = 40 m).

5.3.2.4 Factor of Safety against Yielding

Like normal stresses, the factor of safety against yielding was affected by all corrosion patterns, as shown in Figure 5.14. The minimum factor of safety against yielding, $FS_{y(min)}$, was reduced the most for the 'Full Circumference' and 'Haunches' patterns (-79.9% in both cases), followed by 'Invert' (-77.6%) and 'Crown' (-65.8%).

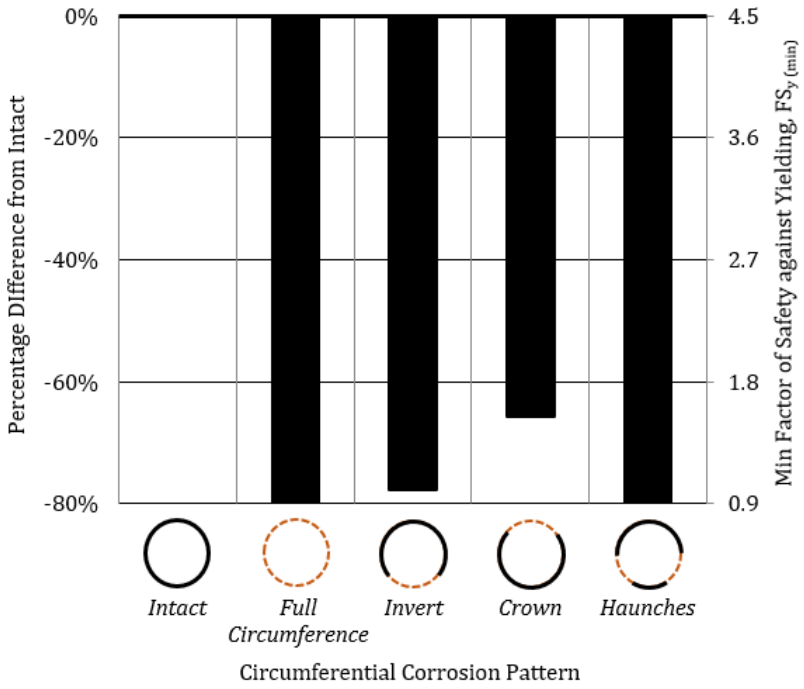

Figure 5.14 Influence of the circumferential corrosion pattern on the minimum factor of safety against yielding (P_t = 20%, L_c = L = 40 m).

5.3.3 Effect of Percentage of Intact Plate Thickness Remaining

The influence of the percentage of intact plate thickness remaining, P_t, was assessed by running a series of simulations and varying the value of P_t in each simulation, while holding the other parameters constant (circumferential corrosion pattern = 'Full Circumference', θ_c = 360°, and L_c = L = 40 m).

5.3.3.1 Thrusts

The maximum live load thrust was reduced non-linearly with reducing plate thickness, as shown in Figure 5.15. This trend can be explained by the fact that the amount of incremental flexural deflection of the pipe crown is inversely proportional to its flexural rigidity, EI (the pipe crown effectively behaves as a horizontal beam), and that positive soil arching is proportional to the magnitude of flexural deflection. The amount of positive soil arching (i.e. reduction in thrust) would therefore be inversely proportional to the flexural rigidity of the pipe plate (and thus, P_t).

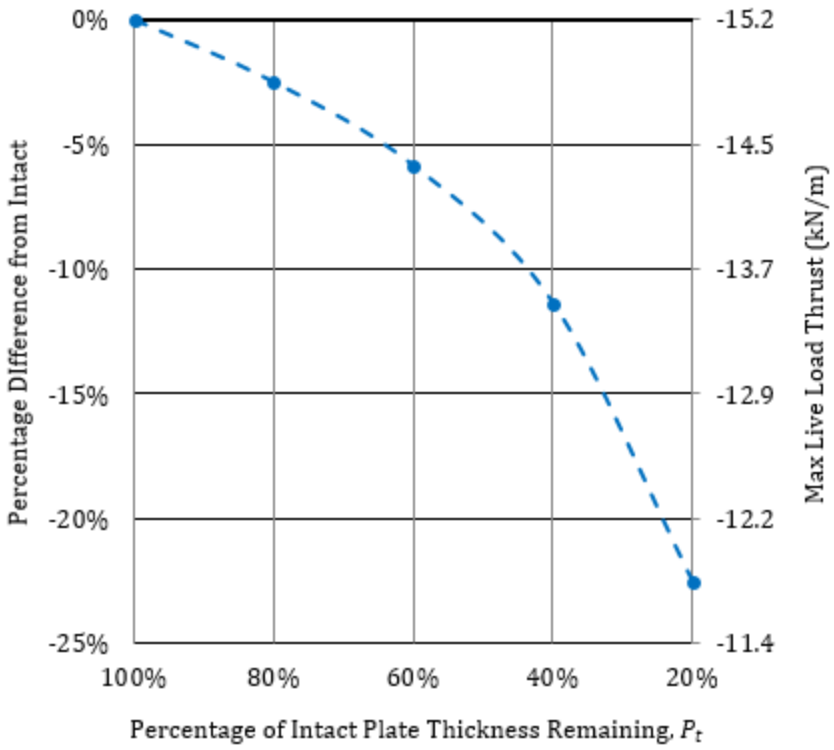

Figure 5.15 Influence of the percentage of intact plate thickness remaining on the maximum live load thrust (θ_c = 360°, L_c = L).

5.3.3.2 Bending Moments

The relationship between maximum live load bending moment and remaining plate thickness was approximately linear, as shown in Figure 5.16. This result may be because the maximum live load bending moment occurs at the shoulders, while the maximum deflection occurs at the crown. The reduction in bending moment would therefore not be directly proportional to the reduction in flexural rigidity of the pipe. In other words, two inversely proportional relationships (deflection vs *EI*, and max bending moment vs deflection) result in a directly proportional relationship (max bending moment vs *EI*).

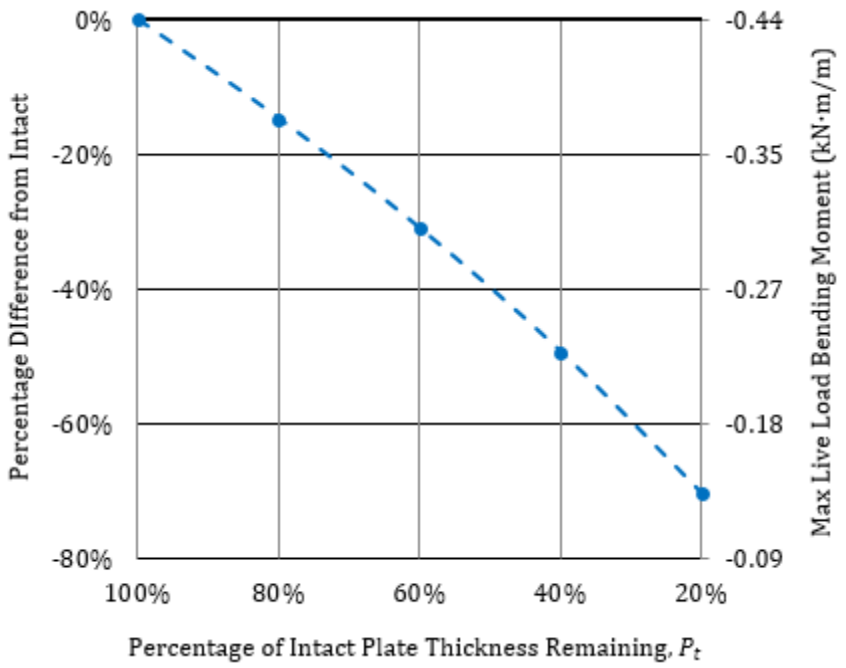

Figure 5.16 Influence of the percentage of intact plate thickness remaining on the maximum live load bending moment in the CMP (θ_c = 360°, L_c = L).

5.3.3.3 Normal Stresses

The influence of remaining plate thickness on the maximum normal stress (combined axial and bending stress) in the pipe is shown in Figure 5.17. The relationship between the percentage of intact plate thickness remaining and the maximum normal stress is non-linear; the maximum normal stress increases exponentially with increasing amount of corrosion. This result is reasonable; the normal stress is inversely proportional to the cross-sectional area (and thus thickness) of the pipe plate.

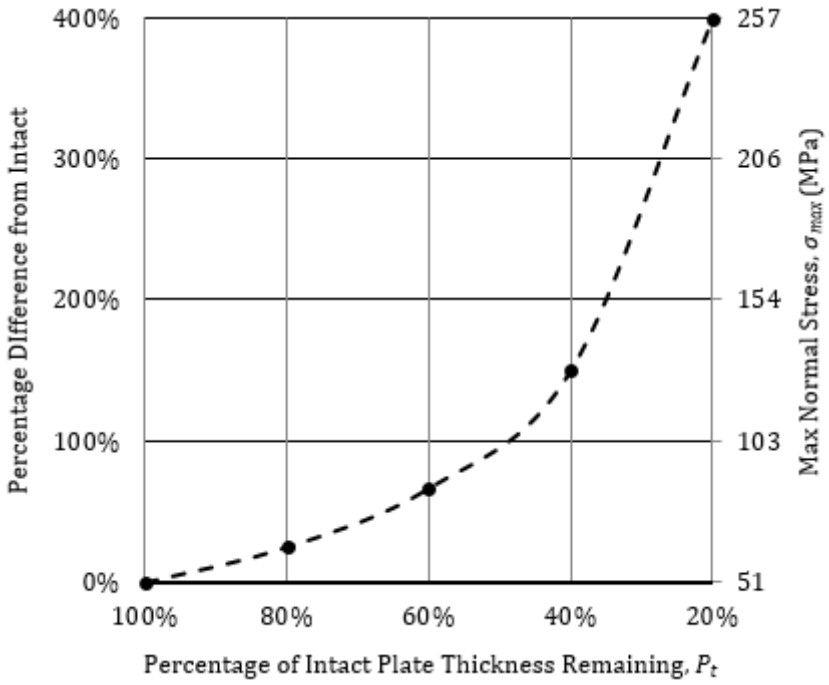

Figure 5.17 Influence of the percentage of intact plate thickness remaining on the maximum normal stress (θ_c = 360°, L_c = L).

5.3.3.4 Factor of Safety against Yielding

As shown in Figure 5.18, the minimum factor of safety against yielding, $FS_{y(min)}$, was linearly proportional to the percentage of intact plate thickness remaining, P_t. The explanation for this trend is simple: FS_y is inversely proportional to the normal stress, and the normal stress is inversely proportional to P_t. Considering those two relationships, FS_y must be directly proportional to P_t.

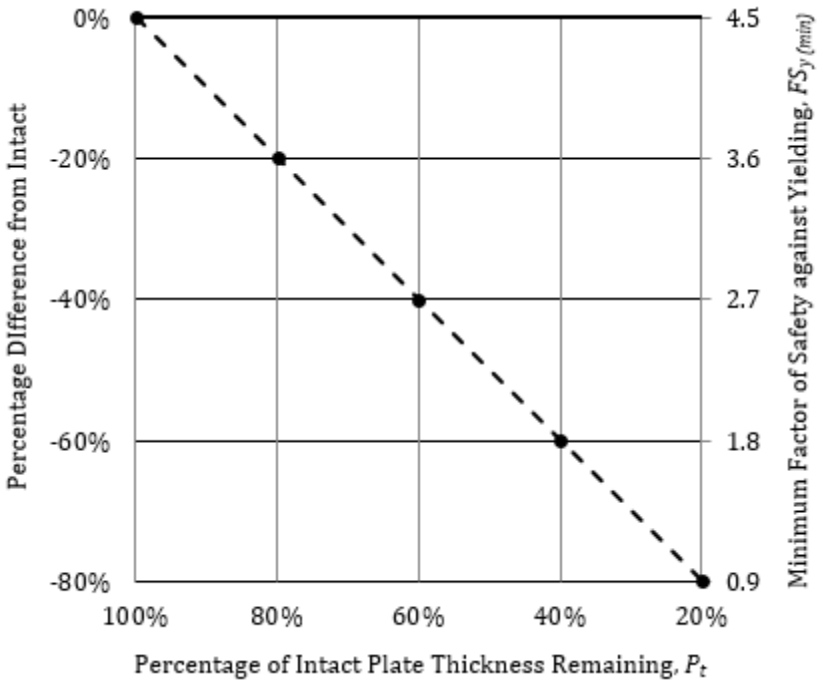

Figure 5.18 Influence of the percentage of intact plate thickness remaining on the minimum factor of safety against yielding (θ_c = 360°, $L_c = L$).

5.3.3.5 Factor of Safety against Buckling

Figure 5.19 shows that the minimum factor of safety against buckling, $FS_{b(min)}$, is also reduced in direct proportion to the reduction in plate thickness, and for the same reason as $FS_{y(min)}$. Following the methodology presented in section 7.6.3.2 of the CHBDC, the computed buckling strength f_b is not significantly affected by the reduced flexural rigidity of the pipe plate. In fact, f_b was 7.1% greater in the corroded pipe than in the intact pipe. Normal stresses are inversely proportional to P_t, while FS_b and P_t are directly proportion.

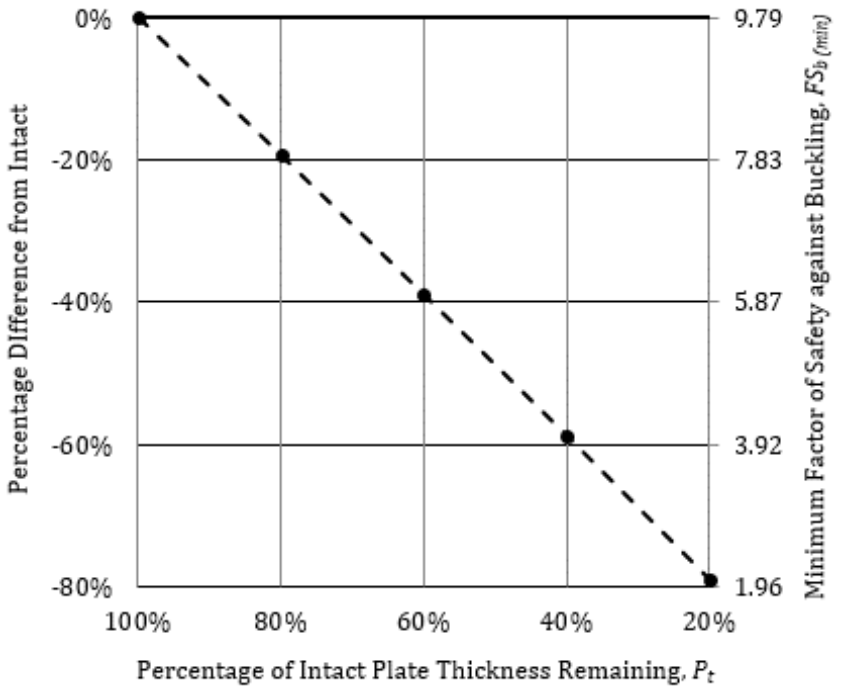

Figure 5.19 Influence of the percentage of intact plate thickness remaining on the minimum factor of safety against buckling (θ_c = 360°, L_c = L).

5.3.4 Effect of Circumferential Extent of Corrosion

The influence of the circumferential extent of corrosion, θ_c, was assessed for three corrosion patterns ('Invert', 'Crown', and 'Haunches') by running a series of simulations and varying the value of θ_c in each simulation, while holding the other parameters constant (P_t = 20% and L_c = L = 40 m).

5.3.4.1 Thrusts

Figure 5.20 shows the influence of the circumferential extent of corrosion on the maximum live load thrust in the CMP. The relationship is nonlinear for each corrosion pattern. However, the curve for the 'Crown' pattern is concave, while the curves for the 'Invert' and 'Haunches' patterns are convex. This can be explained by considering the distribution of live load thrust around the CMP (refer to Figure 5.5); the live load thrust is maximal at the crown, then decreases steadily through the shoulders, springlines, and haunches before reaching a minimum at the invert. Therefore, even at low values of θ_c, the corroded zone of the 'Crown' pattern spans the point of

maximum live load thrust. For the 'Invert' and 'Haunches' patterns, however, the corroded zones begin to span points of larger thrust as the value of θ_c increases.

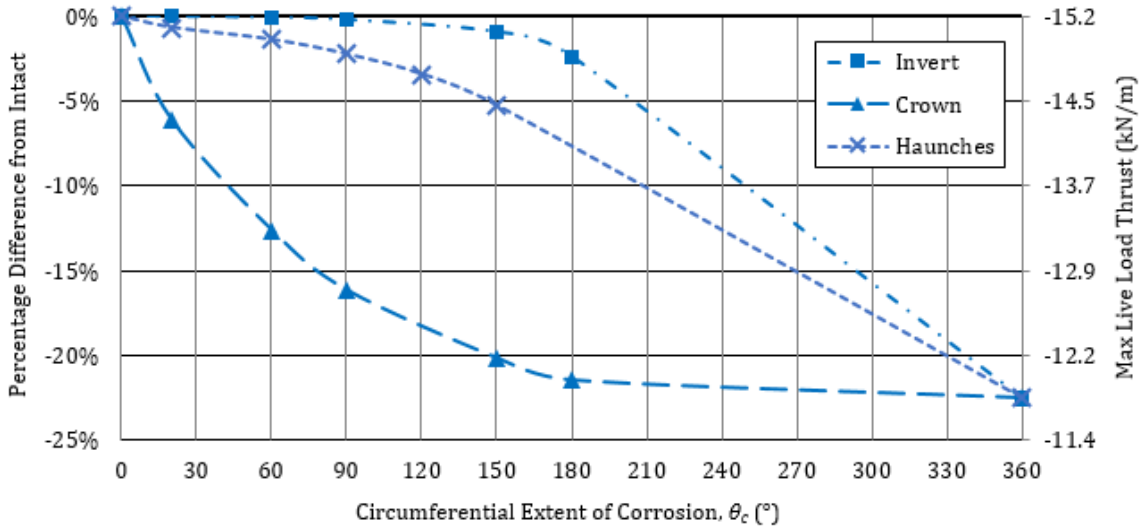

Figure 5.20 Influence of the circumferential extent of corrosion on the maximum live load thrust (P_t = 20%, L_c = L).

5.3.4.2 Bending Moments

The influence of θ_c on the maximum live load bending moment (Figure 5.21) is different than that on the maximum live load thrust, but probably for a similar reason. The curve for the 'Crown' pattern is relatively flat from $0° \le \theta_c \le 60°$, declines almost linearly between $60° \le \theta_c \le 150°$, and becomes flat again from $150° \le \theta_c \le 360°$. The inflection points on this curve match approximately the points of largest live load bending moment (refer to Figure 5.6). Again, the reduction in maximum live load bending moment for the 'Invert' and 'Haunches pattern does not begin until about $\theta_c \ge 180°$, because live load bending moments are negligible on the bottom half of the pipe.

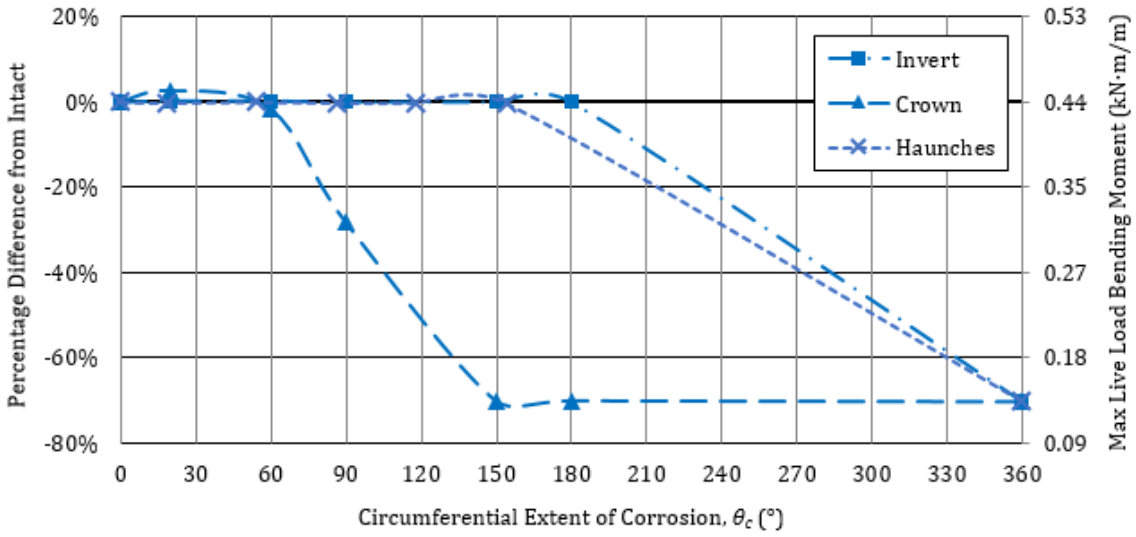

Figure 5.21 Influence of the circumferential extent of corrosion on the maximum live load bending moment (P_t = 20%, $L_c = L$).

5.3.4.3 Normal Stresses

The influence of θ_c on the maximum normal stress is shown in Figure 5.22. These curves make sense when compared to the normal stress distribution around the CMP (refer to Figure 5.7), and considering the points of symmetry of each corrosion pattern. For example, the points of symmetry for the 'Haunches' pattern are 120° and 240°, which are very close to the locations of maximum normal stress. Therefore, haunch corrosion has a huge effect on the maximum normal stress, even when the circumferential extent of corrosion is small, i.e. $\theta_c \geq 20°$. Again, for the 'Invert' and 'Crown' patterns, the inflections points on the curves (60°, 180°) correspond with locations of maximum normal stress.

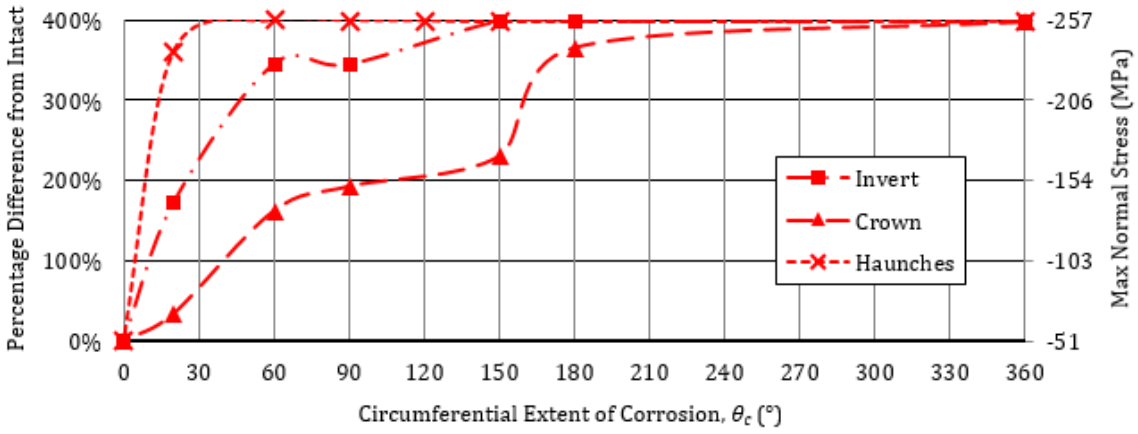

Figure 5.22 Influence of the circumferential extent of corrosion on the maximum normal stress (P_t = 20%, L_c = L).

5.3.4.4 Factor of Safety against Yielding

The influence of θ_c on the factor of safety against yielding (Figure 5.23) is essentially the inverse of the influence on maximum normal stress. Again, the shape of the curves can be explained by comparing them to the distribution of FS_y around the CMP (refer to Figure 5.7). The result suggests that haunch and invert corrosion have larger effects on $FS_{y(min)}$ than crown corrosion for low values of θ_c (e.g. 20°).

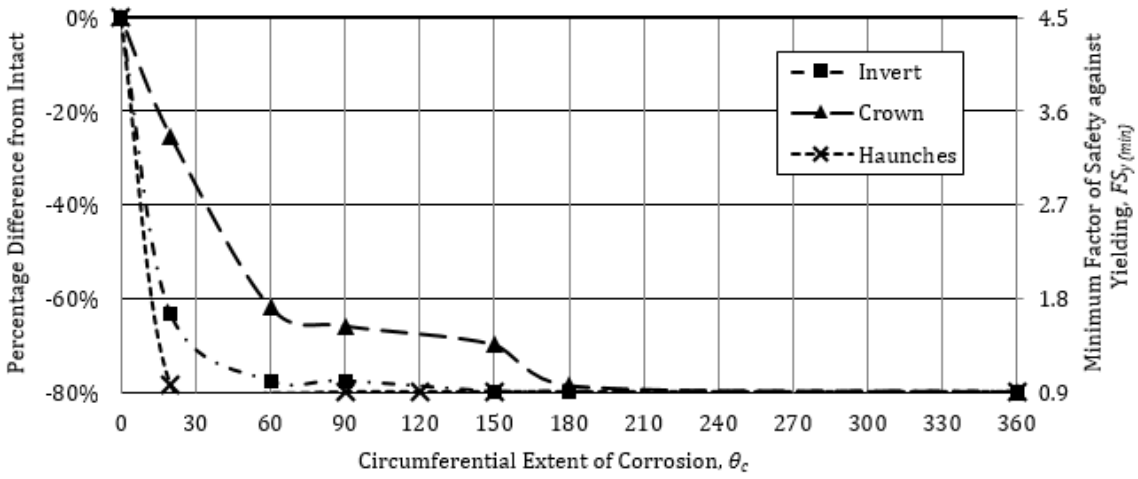

Figure 5.23 Influence of the circumferential extent of corrosion on the minimum factor of safety against yielding (P_t = 20%, L_c = L).

5.3.5 Effect of Longitudinal Extent of Corrosion

5.3.5.1 Thrusts

Figure 5.24 shows the influence of L_c on the maximum live load thrust. The trend shows that the maximum reduction in thrust occurs when the length of the corroded zone is very small (i.e. $L_c \leq 0.6$ m). The reduction in thrust decreases non-linearly with increasing length of the corroded zone until reaching a plateau at around $L_c = 8.0$ m. Beyond $L_c = 8.0$ m, the length of the corrosion zone does not have an influence on the maximum live load thrust.

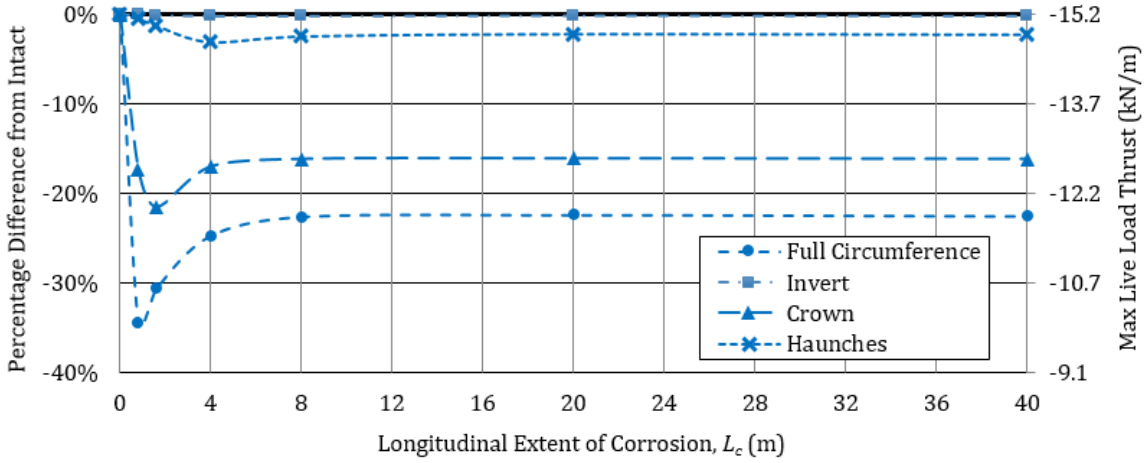

Figure 5.24 Influence of the longitudinal extent of corrosion on the maximum live load thrust ($P_t = 20\%$, $\theta_c = 90°$ (360° for 'Full Circumference')).

5.3.5.2 Bending Moments

Figure 5.25 shows the influence of L_c on the maximum live load bending moment. The curves are like those for the maximum live load thrust, but less pronounced. The length of the corroded zone does not appear to affect the maximum live load bending moment when $L_c \geq 4$ m.

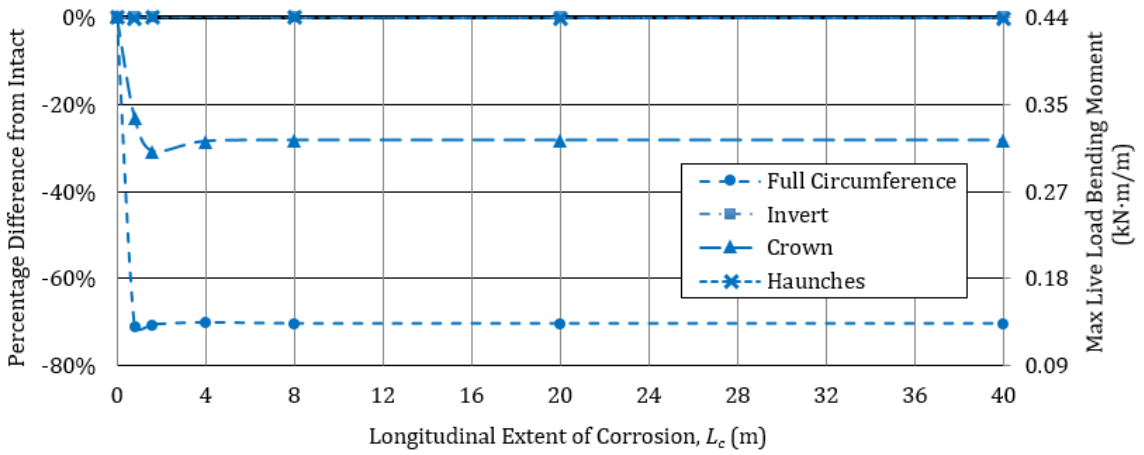

Figure 5.25 Influence of the longitudinal extent of corrosion on the maximum live load bending moment (P_t = 20%, θ_c = 90° (360° for 'Full Circumference')).

5.3.5.3 Normal Stresses

Figure 5.26 shows the influence of L_c on the maximum normal stress in the CMP. The length of the corroded zone has a negligible effect on the maximum normal stress moment for L_c > 0 m.

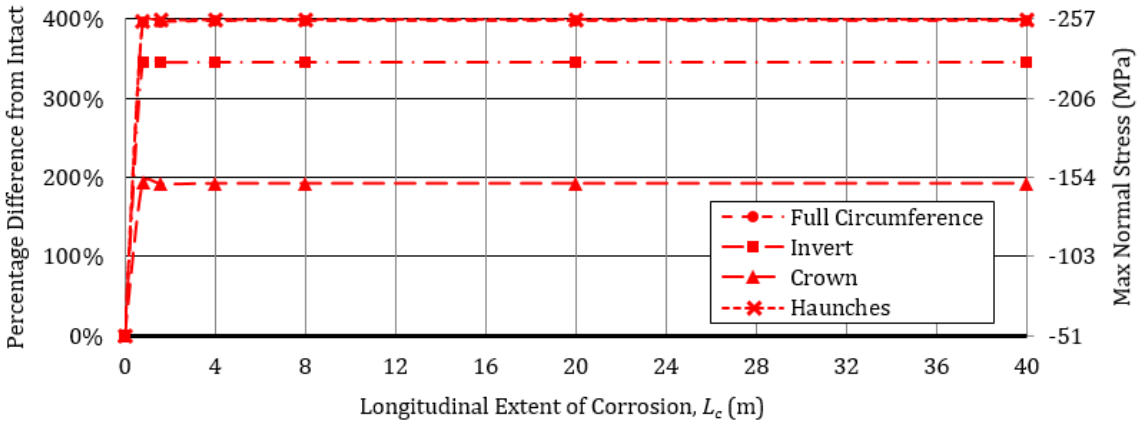

Figure 5.26 Influence of the longitudinal extent of corrosion on the maximum normal stress (P_t = 20%, θ_c = 90° (360° for 'Full Circumference')).

5.3.5.4 Factor of Safety against Yielding

The longitudinal extent of corrosion also has a negligible effect on the minimum factor of safety against yielding (for L_c > 0 m), as shown in Figure 5.27.

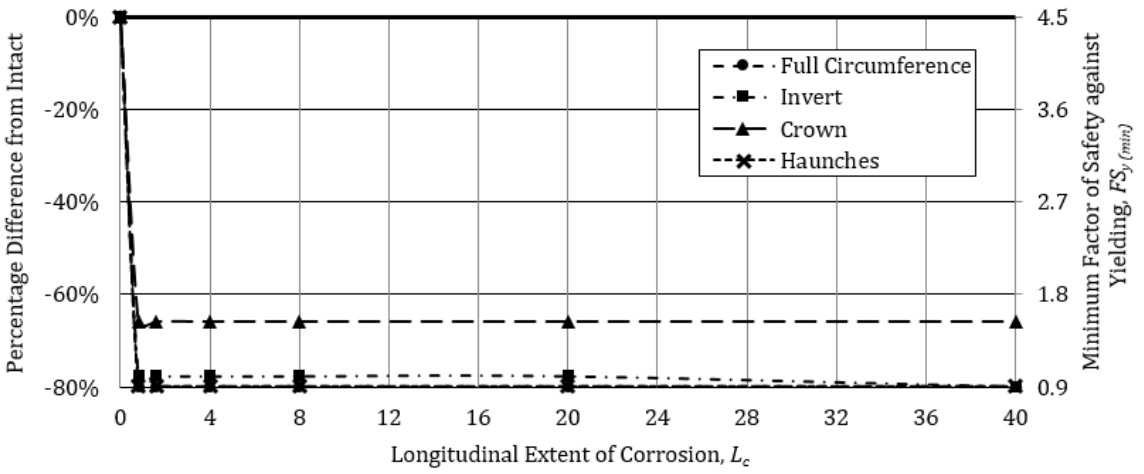

Figure 5.27 Influence of the longitudinal extent of corrosion on the minimum factor of safety against yielding (P_t = 20%, θ_c = 90° (360° for 'Full Circumference')).

5.4 Conclusions

The following conclusions are made:

1. Corrosion of the CMP generally causes a slight *reduction* in live load thrusts and bending moments in the pipe. However, because the maximum dead load forces are located at different locations than the maximum live load forces, corrosion of the CMP has either minor or negligible effects on the total forces in the pipe.

2. Although the total forces in the pipe are largely unaffected by corrosion, normal stresses are increased due to the reduction in cross-sectional area of the pipe plate.

3. The maximum normal stress in the CMP increases exponentially with decreasing plate thickness.

4. The minimum factors of safety against yielding and buckling decrease linearly with decreasing plate thickness. Yielding remains the critical design conditions for 'Full Circumference' corrosion. Stability against buckling was not assessed for other corrosion patterns. However, since $FS_b < FS_y$ at the crown, buckling might be the critical failure mode when corrosion is concentrated at the crown.

5. The circumferential extent of corrosion has a unique effect on the live load forces, maximum normal stress, and a minimum factor of safety against yielding for each different corrosion pattern. For small values of θ_c (e.g. 20°), haunch corrosion has a larger influence on $FS_{y(min)}$ than invert or crown corrosion, because the minimum factor safety against yielding is located at the haunches.
6. The longitudinal extent of corrosion has only a small effect on the live load forces, and a negligible effect on the maximum normal stress and minimum factor of safety against yielding for all corrosion patterns.

CHAPTER 6:
CONCLUSION

The effects of corrosion on the stability of round, corrugated metal pipe (CMP) culverts were examined using 3D finite element (FE) modelling. Firstly, a 3D FE model accounting for non-linear soil behaviour, construction sequence, the soil-CMP interface, anisotropic behaviour of the CMP, and live loading was developed. The model was calibrated by comparing results to experimental data by Mai et al. (2014a). Secondly, a parametric study was carried out for intact (i.e. non-corroded) culverts to determine the sensitivity of pipe forces to various material and geometric parameters. Thirdly, a parametric study was performed for corroded culverts to investigate the effects of different corrosion scenarios on culvert stability.

6.1 Development of a Three-Dimensional Finite Element Model for Corrugated Metal Pipe Culverts

In Chapter 3, a 3D FE model was developed for round, CMP culverts. The model accounted for many of the important aspects of real culverts and could simulate the effects of pipe corrosion. Three (3) simulations were carried out using different soil models (Linear Elastic (LE), Mohr-Coulomb (MC), and Hardening Soil (HS)) to evaluate each of their abilities to predict the pipe response measured experimentally. The output from the model compared reasonably well with the experimental data of Mai et al. (2014a). The HS soil model accurately captured the experimental peaking response of the culvert during backfilling. The MC model was less accurate, and the LE model was inaccurate. These results suggest that the HE model was effective at transferring the simulated compaction-induced loads from the soil to the pipe. The LE model did not predict the dead load thrusts as well as the MC and HS models. Live-load thrust distributions from the MC and HS models were within 1% of each other, and both matched the experimental data closely everywhere except at the crown. The non-linear load-bending moment curve observed in the experiment was well captured by the MC and HS models; the results produced by the LE model were linear

and inaccurate. The observed performance of the developed 3D finite element model is deemed sufficient for proceeding with a parametric study in the following chapters.

6.2 Parametric Study for Intact Corrugated Metal Pipe Culverts

In Chapter 4, several new models were created (using the same methodology described in Chapter 3) to carry out a parametric study on intact CMP culverts. Study parameters included the pipe diameter, height of soil cover, secant modulus of soil, internal friction angle of soil, and the strength reduction factor of the soil-pipe interface. Overall, the total pipe forces are most sensitive to the pipe diameter and the height of soil cover. The former suggests that pipe flexibility is a critical input parameter (i.e. changes to the profile of the corrugated plate would also have a major influence on the pipe forces). The secant modulus of the soil and the strength reduction factor of the soil-pipe interface had a moderate influence on the total pipe forces. The soil friction angle had the smallest influence on the total pipe forces, The maximum dead load thrust always occurred just below the springlines. The maximum live load thrust always occurred at the crown. The maximum dead load bending moments occurred in two (2) places: just below the springlines and just below the haunches. The maximum live load bending moment occurred just above the shoulders. Although maximum total bending moments are small (maximum moment for the baseline case = 2.8 kN), the bending stresses are generally of the same order of magnitude as the axial stresses, and are greater than the axial stresses at the locations of the maximum bending moment(s). The height of soil cover had a significantly larger influence on maximum total thrust (range = 245% of baseline value) than on maximum total bending moment (range = 110% of baseline value). The secant modulus of the soil had a significantly larger influence on the maximum total bending moment (range = 45% of baseline value) than on maximum total thrust (range = 5% of baseline value).

6.3 Parametric Study for Corroded Corrugated Metal Pipe Culverts

In Chapter 5, the same model from Chapter 4 was used to simulate a corroded culvert and conduct a parametric study on corroded culverts. Study parameters included the circumferential corrosion pattern [Full Circumference, Invert, Crown, Haunches], the percentage of intact plate thickness remaining, and both the circumferential and longitudinal extents of corrosion. In general, corrosion of the CMP caused a reduction (not increase) in live load thrusts and bending moments in the pipe. However, because the maximum dead load forces are located at different locations than the live load forces, corrosion of the CMP has either minor or negligible effects on the total forces in the pipe. Although the total forces in the pipe were largely unaffected by corrosion, normal stresses increased due to the reduction in cross-sectional area of the pipe plate. The maximum normal stress in the CMP increased exponentially with decreasing plate thickness. The minimum factors of safety against yielding and buckling decreased linearly with decreasing plate thickness. Stability against buckling was only assessed for the Full Circumference corrosion patterns. Since $FS_b<FS_y$ at the crown, buckling could be the critical failure mode when corrosion is concentrated at the crown. The circumferential extent of corrosion had a unique effect on the live load forces, maximum normal stress, and minimum factor of safety against yielding for each different corrosion pattern. For small values of θ_c (e.g. 20°), haunch corrosion had a larger influence on the minimum factor safety against yielding than invert or crown corrosion, because the $FS_{y\ (min)}$ occurred at the haunches. The longitudinal extent of corrosion had only a small effect on the live load forces, and a negligible effect on the maximum normal stress and minimum factor of safety against yielding for all corrosion patterns.

6.4 Applicability and Future Work

The results and observations from this research reinforce the findings of El-Taher and Moore (2008) that, in general, corrosion of CMP culverts reduces the factor of safety against yielding in direct proportion to the reduction in pipe thickness. The results of

the parametric study on corroded culverts suggest that haunch corrosion may have a larger effect on the factor of safety against yielding than invert or crown corrosion for narrow circumferential extents of corrosion, since the haunches are closer to the location of maximum stress (just below the springlines).

Additional research is required to fully understand the influence of pipe deterioration on the stability of the culvert. The model predictions for corroded culverts presented herein should be verified against experimental observations. Other examples of future work could include modelling the effects of corrosion for other shapes of corrugated culverts (e.g. pipe-arch, horizontal ellipse, etc.), and modelling the corrugated geometry of the pipe explicitly. If developed, a superior method for simulating compaction effects would have wide-ranging applications to soil-structure interaction problems.

REFERENCES

1. Aagah, O., & Aryannejad, S. (2014). *Dynamic analysis of soil-steel composite railway bridges* (Master of Science). KTH Royal Institute of Technology, Sweden

2. AASHTO. (2014). *LRFD bridge design specifications.* (7th ed.). American Association of State Highway and Transportation Officials.

3. Abdel-Sayed, G. (1978). Stability of flexible conduits embedded in soil. *Canadian Journal of Civil Engineering, 5*, 324-333.

4. Allen, R. L., Duncan, J. M., & Snacio, R. T. (1988). *An engineering manual for sheet pile walls.* Blacksburg, VA: Department of Civil Engineering, Virginia Tech.

5. Armtec. (2015). Culvert design 201. structural design, durability & applications. technical webinar. Retrieved from https://www.slideshare.net/Armtecltd/keep-it-flowing-culvert-design-20-design-durability-applications

6. Bakht, B. (1980, August). *Live load testing of soil-steel structures.* SRR-80-4. Ontario Ministry of Transportation and Communication, Policy Planning and Research Division.

7. Bell, A. L. (1915). The lateral pressure and resistance of clay and the supporting power of clay foundations. *Minutes of the Proceedings of the Institution of Civil Engineers, , 199*(1915), 233-272.

8. Brinkgreve, R. B. G. (2015). Plaxis 3D*AE.01*

9. Burns, Q., & Richard, M. (1964). Attenuation of stresses for buried cylinders. *Proc., Symposium of Soil-Structure Interaction, Univ. of Arizona Eng. Research Lab., Tucson, Arizona,*

10. Coduto, D. P. (1999). *Geotechnical engineering: Principles and practices.* (illustrated ed.). Prentice Hall.

11. Contech. (2017). Culverts, canals, and enclosures. Retrieved from http://www.conteches.com/products/applications/culverts-canals-and-enclosures

12. Corrugated Steel Pipe Institute. (2009). *Handbook of steel drainage & highway construction products.* (2nd Canadian ed.). Canada: American Iron and Steel Institute.

13. Coulomb, C. A. (1776). Sur une application des regles maximis et minimis a quelques problemes de statique, relatifs a l'architecture. *Acad. Sci. Paris Mem. Math. Phys., 7*, 343-382.

14. CSA. (2014). *Canadian highway bridge design code. CSA standard CAN/CSA-S6-14.* Rexdale, Ontario: Canadian Standards Association.

15. Desai, C. S., & Nagaraj, B. K. (1988). Modeling for cyclic normal and shear behaviour of interfaces. *Journal of Engineering Mechanics, 114*(7), 1198-1217.

16. Duncan, J. M. (1978). Soil-culvert interaction method for design of metal culverts. *Transportation Research Record,* (678), 53-59.

17. Duncan, J. M. (1979). Behaviour and design of long-span metal culverts. *Journal of Geotechnical Engineering, 105*(GT3), March 1979.

18. El-Sawy, K. M. (2003). Three-dimensional modeling of soil-steel culverts under the effect of truckloads. *Thin-Walled Structures, 41*(8), 747-768. doi: 10.1016/S0263-8231(03)00022-3

19. Elshimi, T. M. (2011). *Three-dimensional nonlinear analysis of deep-corrugated steel culverts* (Doctoral dissertation). Available from QSpace theses database.Queen's University, Kingston, ON

20. Elshimi, T. M., & Moore, I. D. (2013). Modeling the effects of backfilling and soil compaction beside shallow buried pipes. *Journal of Pipeline Systems Engineering and Practice, 4*(4), 04013004-1-04013004-7. doi: 10.1061/(ASCE)PS.1949-1204.0000136

21. El-Taher, M. (2009). *The effect of wall and backfill soil deterioration on corrugated metal culvert stability* (Doctoral dissertation). Available from QSpace theses database.Queen's University, Kingston, Ontario, Canada

22. El-Taher, M., & Moore, I. D. (2008). Finite element study of stability of corroded metal culverts. *Transportation Research Record: Journal of the Transportation Research Board, 2050*, 157-166. doi: 10.3141/2050-16

23. EPA. (1991). *Sewer system infrastructure analysis and rehabilitation. EPA/625/6-91/030.* Cincinnati, OH: United States Environmental Protection Agency.

24. FHA. (1995, May). *Culvert repair practices manual.* Publication No. FHWA-RD-94-096. U.S. Department of Transportation Federal Highway Administration.

25. Girges, Y., & Abdel-Sayed, G. (1995). Three-dimensional analysis of soil-steel bridges. *Canadian Journal of Civil Engineering, 22*(6), 1155-1163. doi: 10.1139/l95-133

26. Hansen, P. L. (2007). Rehabilitation opportunities for NBDOT steel culvert type bridges. *Prepared for Presentation at the 2007 Annual Conference of the Transportation Association of Canada,* Saskatoon, Saskatchewan, 10.

27. Ingold, T. S. (1979). The effects of compaction on retaining walls. *Géotechnique, 29*, 265-283.

28. Jaky, J. (1948). Pressure in silos. *Proceedings of the 2nd International Conference on Soil Mechanics and Foundation Engineering, , 1*, 103-107.

29. Katona, M. G. (1976). *CANDE: A modern approach for the structural design and analysis of buried culverts.* Report FHWA-RD-77-5. Federal Highway Administration, Department of Transportation, Washington, D.C.

30. MacDonald, L. (2010). *Numerical modelling of vehicle loads on buried orthotropic steel shell structures* (Master's thesis). Available from DalSpace Theses database.Dalhousie University, Halifax, NS

31. Mai, V. T. (2013). *Assessment of deteriorated corrugated steel culverts* (Master's thesis). Available from QSpace theses database.Queen's University, Kingston, ON, Canada

32. Mai, V. T., Hoult, N. A., & Moore, I. D. (2012). Assessment of corroded corrugated steel culverts using field data. *North American Society for Trencless Technology: No-Dig show 2012,* Nashville, TN, 10.

33. Mai, V. T., Hoult, N. A., & Moore, I. D. (2014a). Effect of deterioration on the performance of corrugated steel culverts. *Journal of Geotechnical and Geoenvironmental Engineering, 140*(2) doi: 10.1061/(ASCE)GT.1943-5606.0001021

34. Mai, V. T., Moore, I. D., & Hoult, N. A. (2014b). Performance of two-dimensional analysis: Deteriorated metal culverts under surface live load. *Tunelling and Underground Space Technology, 42*, 152-160. doi: 10.1016/j.tust.2014.02.015

35. Mattsson, H., & Sundquist, H. (2007). The real service life and repair methods of steel pipe culverts in sweden. *Proceedings of the 1st European Conference on Buried Flexible Steel Structures,* Rydzyna, Poland, 185-192.

36. Mayne, P. W., & Kulhawy, F. H. (1982). K_0-OCR relationships in soil. *Journal of the Geotechnical Engineering Division, 108*(GT6), 851-872.

37. Mayniel, K. (1808). Traite experimental, analytique et preatique de la poussee des terres et des murs de revetement, paris.

38. McGrath, T. J. (1999). Calculating loads on buried culverts based on pipe hoop stiffness. *Transportation Research Record: Journal of the Transportation Research Board, 1656*, 73-79. doi: 10.3141/1656-10

39. McGrath, T. J., Moore, I. D., Selig, E. T., Webb, M. C., & Taleb, B. (2002). *NCHRP report 473: Recommended specifications for large span culverts.* Transportation Research Board, Washington, D.C.

40. Moore, I. D., & Brachman, R. W. (1994). Three-dimensional analysis of flexible circular culverts. *Journal of Geotechnical Engineering, 120*(10), 1829-1844. doi: 10.1061/(ASCE)0733-9410(1994)120:10(1829)

41. Müller-Breslau, H. (1906). Erddruck auf stutzmauern, alfred kroner, stuttgart.

42. Perrin, J. J., & Jhaveri, C. S. (2004, January). *The economic costs of culvert failures.* Transportation Research Board. Retrieved from www.concrete-pipe.org/pdf/economiccosts.pdf

43. Petersen, D. L., Nelson, C. R., Li, G., McGrath, T. J., & Kitane, Y. (2010). *NCHTP report 647: Recommended design specifications for live load distribution to buried structures.* Transportation Research Board, Washington, D.C.

44. Plaxis bv. (2013). *Plaxis 3D reference manual - anniversary edition.* Retrieved from http://www.plaxis.nl/files/files/3D-2-Reference.pdf

45. Plaxis bv. (2015). *Plaxis material models manual.* Retrieved from http://www.plaxis.nl/files/files/3D-3-Material-Models.pdf

46. Rankine, W. (1857). On the stability of loose earth. *Philosophical Transactions of the Royal Society of London. , 147*

47. Roberge, P. R. (2008). *Corrosion engineering: Principles and practice.* (1st ed.). McGraw-Hill Education.

48. Scott, J. D., Bauer, G. E., & Shields, D. H. (1977). *Triaxial testing on granular A aggregate.* Ont. Project O-1. Ontario Joint Transportation and Communications Research Program.

49. Seed, R. B., & Raines, J. R. (1988). Failure of flexible long-span culverts under exceptional live load. *Transportation Research Record,* (1191), 20-22.

50. Selig, E. (1990). Soil properties for plastic pipe installations. In In M. J. Cassidy, & G. S. Buczala (Eds.), (Ed.), *Buried plastic pipe technology, ASTM special technical publication 1093* (pp. 141-158). W. Conshohocken, PA: American Society for Testing and Materials.

51. Spangler, M. G. (1941). The structural design of flexible pipe culverts. *Iowa Engineering Experiment Station. Bulletin 153,*

52. Taleb, B., & Moore, I. D. (1999). Metal culvert response to earth loading: Performance of two-dimensional analysis. *Transportation Research Record: Journal of the Transportation Research Board, 1656*, 25-36. doi: 10.3141/1656-04

53. Tenbusch, A., Dorwart, B., & Tenbusch, A. F. (2009, August). *Failing culverts - the geotechnical perspective.* Retrieved from http://www.tenbusch.com/underground_equipment/files/FailingCulvertsGeotechnicalPerspective.pdf

54. Terzaghi, K. V. (1936). Stress distribution in dry and in saturated sand above a yielding trap-door. *Proceedings of the 1st International Conference on Soil Mechanics and Foundation Engineering,* Cambridge, MA*, 1*, 307-311.

55. Terzaghi, K. V. (1943). *Theoretical soil mechanics.* New York, NY: John Wiley and Sons.

56. United States Army Corps of Engineers. (1998, March 31). *Engineering and design: Conduits, culverts, and pipes.* EM 1110-2-2902. Retrieved from www.publications.usace.army.mil/Portals/76/Publications/EngineerManuals/EM_1110-2-2902.pdf

57. Watkins, R. K., & Anderson, L. R. (1999). *Structural mechanics of buried pipes.* USA: CRC Press LLC. doi: 10.1201/9781420049572.fmatt

58. Watkins, R. K., & Spangler, M. G. (1958). Some characteristics of the modulus of passive resistance of soil: A study in similitude. *Highway Research Board Proc. , 37*(576)

59. Webb, M. C. (1995). *Field studies of buried pipe behavior during backfilling.* (Unpublished master's thesis). University of Massachusetts at Amherst, USA.

60. Zienkiewicz, O. C., & Taylor, R. L. (2005). *The finite element method for solid and structural mechanics.* (6th ed.). Butterworth-Heinemann.

APPENDIX A

SAMPLE STRESS CALCULATIONS

Pipe stresses were not generated directly from the Plaxis 3D Model. The total circumferential forces in the pipe (thrust N and bending moment M) output from the model were processed via spreadsheet. Below are sample calculations for a point located at the crown (0°) for the baseline case from Chapter 4, with the live load applied.

Input Parameters

Parameter	**Value**	**Units**
A	6.149	mm^2/mm
I	1867.12	mm^4/mm
r	17.425	mm
σ_b	-4,317.3	kPa
$R = R_c$	2,500	mm
E	200,000	MPa
$E_s = E_m$ (lower)	60	MPa
F_y	230	MPa
H	1.2	m
H'	1.25	m
ϕ_t	0.80	-
F_m	1.0	-
λ (lower)	1.22	-

Calculated Parameters

Parameter	Value	Units	Equation
N	-73.784	kN/m	-
M	-0.316	kN·m/m	-
$\boldsymbol{\sigma_a}$	**-12,035**	**kPa**	**5.2/5.3**
σ_b	-4,317.3	kPa	5.2/5.3
σ_{in}	-7,717.9	kPa	5.2
σ_{out}	-16,352.6	kPa	5.3
$\boldsymbol{\sigma}$	**-16,352.6**	**kPa**	**5.4**
$\boldsymbol{FS_y}$	**14.1**	**-**	**5.5**
θ_0	5.7	°	5.7
ρ	0.9899		5.12
E_m (upper)	44.7	MPa	5.8
λ (upper)	1.52	-	5.10
K (upper)	0.2307	-	5.9
K (lower)	0.1724	-	5.9
R_e (upper)	5,429	mm	5.11
R_e (lower)	7,266	mm	5.11
f_b (upper)	164.5	MPa	5.13
f_b (lower)	173.1	MPa	5.13
$\boldsymbol{f_b}$	**164.5**	**MPa**	**-**
$\boldsymbol{FS_b}$	**13.7**	**-**	**5.6**